IMPROVING RESILIENCE OF COASTAL STRUCTURES SUBJECT TO TSUNAMI-LIKE WAVES

A thesis submitted to The University of Manchester for the degree of

Doctor of Philosophy

in the Faculty of Engineering and Physical Sciences

2016

Gede Pringgana

School of Mechanical, Aerospace and Civil Engineering

Contents

List of Published Works and Award

Parts of this research project have been presented or submitted for publication, as follows:

Journal papers:

- Cunningham, L.S., Rogers, B.D. and Pringgana, G., 2014. Tsunami wave and structure interaction: an investigation with smoothed-particle hydrodynamics. *ICE Journal of Engineering and Computational Mechanics*, 167(EM3), pp.126–138.

- Pringgana, G., Cunningham, L.S., and Rogers, B.D. Modelling of tsunami-induced bore and structure interaction. *ICE Journal of Engineering and Computational Mechanics*. (Accepted for publication).

Conference papers:

- Pringgana, G., Cunningham, L.S., and Rogers, B.D. 2015. Modelling tsunami bore impact on structure using SPH. *11th Young Coastal Scientists and Engineers Conference*, Manchester, 23rd – 24th March 2015.

- Pringgana, G., Cunningham, L.S., and Rogers, B.D. 2015. SPH modelling of tsunami-induced bore and structure interaction using DualSPHysics, *Proceedings of the 23rd UK Conference of the Association for Computational Mechanics in Engineering (ACME)*, Swansea, 8th – 10th April 2015.

- Pringgana, G., Cunningham, L.S., and Rogers, B.D. 2015. Modelling of tsunami bore impact on structures using DualSPHysics. *1st DualSPHysics Users Workshop*, Manchester, 8th – 9th September 2015.

Award:

- Thomas Telford Premium 2014, awarded by the Institution of Civil Engineers.

List of Tables

List of Figures

List of Symbols and Operators

Symbol	**Definition**
α_D	normalisation parameter
f_j	scalar quantity
g	gravitational acceleration
γ	polytrophic index
h	characteristic smoothing length
P	pressure
h_0	water depth
Π	artificial viscosity
r	distance between particles
ρ	density of particle
ρ_0	reference density for water (1000 kg/m^3)
v	flow velocity
W	weighting or kernel function
A_i	tributary area where pressure probe *i* is situated
B	the breadth of structure
D	represent a certain length of 1 m in the SPH model
d_p	water particle size or the initial spacing of particle
E	Young's modulus of elasticity
F_i	force at a certain point in a 3-D model
H	solitary wave height
h	characteristic smoothing length
h_0	offshore water depth/ still water level
h_b	the height of the bore
L	shortest dimension of box in convergence study (0.161 m)
L_p	layers of pressure probes
P_i	pressure at a certain area in a 3-D model
ρ	density
v	Poisson's ratio
v_j	the velocity of bore

List of Abbreviations

ASCE	American Society of Civil Engineers
CCBFC	Canadian Commission on Building and Fire Codes
CCH	Coastal Construction Honolulu
CCM	City and County of Manual
FEM	Finite Element Method
FEMA	Federal Emergency Management Agency
IBC	International Building Codes
ICBO	International Conference of Building Officials
OCADI	Overseas Coastal Area Development Institute
SPH	Smoothed Particle Hydrodynamics
UBC	Uniform Building Code
USACE	United State Army Corps of Engineers

Abstract

University of Manchester
Gede Pringgana
Doctor of Philosophy
Improving Resilience of Coastal Structures Subject to Tsunami-like Waves
2016

This thesis investigates tsunami impact on shore-based, low-rise structures in coastal areas. The aims are to investigate tsunami wave inundation in built-up coastal areas with reference to structural response to wave inundation, to assess the performance of current design codes in comparison with validated state-of-the-art numerical models and to improve structural design of residential buildings in tsunami risk areas. Tsunami events over the past few decades have shown that a significant proportion of fatalities can be attributed to the collapse of building infrastructure due to various actions of the incident waves. Although major tsunami events have demonstrated the potential catastrophic effects on built infrastructure, current building codes have no detailed or consistent guidance on designing structures in tsunami-prone regions. Furthermore, considerable differences in existing empirical formulae highlight that new research is necessary to appropriately address the particularities of the tsunami-induced forces and structure response into the design standards.

In this thesis, numerical modelling methods are used to simulate hydrodynamic impact on shore-based coastal structures. The hydrodynamic simulations were conducted using a novel meshless numerical method, smoothed particle hydrodynamics (SPH), which is coupled with the finite element (FE) method to model structural behaviour. The SPH method was validated with experimental data for bore impact on an obstacle using a convergence study to identify the optimum particle size to capture the hydrodynamics. The FE model was validated against experimental data for plates under transient blast loads which have similar load characteristics with impulsive tsunami-induced bore impacts.

One of the contributions of the thesis is the use of a new coupling method of the SPH-based software DualSPHysics and FE-based software ABAQUS. Using SPH particle spacing of the same size as the FE mesh size, enables the SPH output pressure to be directly applied as an input to the structural response model. Using this approach the effects of arrangement and orientation of single and multiple low rise structures are explored. Test cases were performed in 2-D and 3-D involving a discrete structure and multiple structures. The 3-D SPH simulations with single and multiple structures used an idealised coastal structure in the form of a cube with different on-plan orientations (0°, 30°, 45° and 60°) relative to the oncoming bore direction. The single structure cases were intended to study the improvement of the resilience of coastal structures by reducing the acting pressures on the vertical surfaces by changing the structure's

orientation. It was found the pressure exerted on the vertical surface of structure can be reduced by up to 50% with the 60° orientation case. The multiple structure models were conducted to examine shielding and flow focusing phenomena in tsunami events. The results reveal that the distance between two adjacent front structures can greatly influence the pressure exerted on the rear structure. This thesis also demonstrates the capability of SPH numerical method in simulating standard coastal engineering problems such as storm waves impact on a recurve wall in 2-D.

The idealised structures were represented as standard timber construction and the finite element modelling was used to determine the corresponding stress distributions under tsunami impact. Following the comparison of the method used in this thesis with commonly used design equations based on the quasi-static approach, large differences in stress prediction were observed. In some cases the loads according to the design equations predicted maximum stresses almost one order of magnitude lower. This large discrepancy clearly shows the potential for non-conservative design by quasi-static approaches.

The new model for the simulation of tsunami impact on discrete and multiple structures shows that the resilience of a coastal structure can be improved by changing the orientation and arrangement. The characteristics of tsunami waves during propagation and bore impact pressures on structures can be assessed in great detail with the combined SPH and FE modelling strategy. The techniques outlined in this thesis will enable engineers to gain a better insight into tsunami wave-structure interaction with a view towards resilience optimisation of structures vulnerable to tsunami impact events.

Declaration

No portion of the work referred to in this report has been submitted in support of an application for another degree or qualification of this or any other university or other institute of learning.

Acknowledgements

This thesis would not exist if not for the emotional and scientific support of the following people:

- I would like to express my appreciation to my supervisors, Dr. Benedict D. Rogers and Dr. Lee S. Cunningham, for their invaluable supervision, continuous support, patience, guidance, ideas and critical feedbacks.
- I would like to thank the Directorate General of Higher Education of The Republic of Indonesia for the financial support of this research.
- I would like to thank my institutions; *Kopertis Wilayah VIII* and Warmadewa University in Bali for their support.
- I am thankful to all the members of the University of Manchester SPH and Structure research groups for their continuous support throughout regular meetings and especially to Dr. Athanasios Mokos, Dr. Stephen Longshaw and Dr. Georgios Fourtakas for their assistance in computational issues.
- I would like to thank the University of Manchester academic and IT staff for providing excellent and informative workshops and for their technical support.
- I would like to thank my colleagues at the university and also my house mates for their daily support.
- Last but not least, I would like to express my gratitude to my family for their love, patience, support and encouragements over the years.

Chapter 1

Introduction

1.1 Background

Tsunamis and wind-waves are water waves that move inland and can inundate low-elevation coastal regions. The tsunami and wind-wave-induced forces may cause damage to coastal structures including residential buildings. Both tsunamis and storm surges (wind-waves) are reported to cause similar damaging effects to coastal structures as stated in Robertson *et al.* (2007). A small-scale tsunami wave impact can cause minor damage to infrastructure and lifeline utilities (Reese *et al.*, 2007). However, large-scale events can cause catastrophic damage to coastal structures as shown by the 2004 Indian Ocean tsunami event. Saatcioglu *et al.* (2005) reported that the 2004 Indian Ocean tsunami caused widespread damage in Indonesia, Malaysia, Myanmar, Thailand, Bangladesh, Sri Lanka, India and 12 other countries around the Indian Ocean. The effects of the tsunami were felt as far away as Somalia, Tanzania and Kenya along the east coast of Africa.

Forces due to the impact of tsunamis are frequently ignored in structural design practice. The low probability of large-scale tsunamis in the inhabited and built environment is possibly the main reason. Indeed, major tsunamis have a recurrence interval of more than 500 years, whereas it is standard practice for structural engineers to take into account earthquake-induced forces with a return period of 2,500 years in design practice (Saatcioglu, 2009). Large magnitude tsunamis can cause disastrous effects as demonstrated by the 2004 Indian Ocean and the 2011 East Japan tsunami events which generated massive structural damage on infrastructure. Casualties were in excess of 300,000 while the destruction of residential buildings left approximately 1.5 million people homeless in the Indian Ocean event alone (Ghobarah *et al.*, 2006). Although major tsunami events have demonstrated the potential catastrophic effects on built infrastructure, current building codes have no consistent guidance on designing coastal structures in high tsunami-risk regions (Palermo and Nistor, 2008). Furthermore, considerable differences in existing empirical formulae highlight that new research is necessary to appropriately address the addition of the tsunami-induced forces and also the debris impact forces into the design standards (Nistor *et al.*, 2010). This thesis aims to address these gaps in our knowledge and understanding.

Research post events has shown that the vast majority of structures that were partially damaged or completely destroyed in the 2004 and 2011 tsunami events were residential buildings. Suppasri *et al*. (2013) stated that 115,163 houses were heavily damaged, 162,015 houses were moderately damaged and 559,321 houses were partially damaged caused by the 2011 East Japan tsunami alone. Many of those residential houses were low-storey and made of timber. A timber structure might survive the earthquake that generated the tsunami due to their relatively high strength-to-mass ratio and flexibility but could not resist the hydrodynamic forces resulting from the tsunami-induced bore impacts. An improved understanding of the residential building response to tsunami loads could help reduce casualties, increase survivability of such structures and speed up recovery time post-tsunami. Becker *et al*. (2011) show that a key factor of building response to the external actions is the interaction between the structural components of the building and the wave. The pressure of the tsunami bore can be likened to the pressures attributable to winds which are treated as uniform lateral pressures acting along the entire height of the building. However, in determining tsunami loads, the varying depth of the water, associated velocity and duration of impact are added variables that affect the resulting force and structure response.

Robertson *et al*. (2011) categorized the main research on wave impact loads on structures into the following three areas: (i) work related with storm wave impact on offshore platforms which is presently the most commonly studied; (ii) combining experimental and numerical research in order to develop design formulae for associated loads on structures; (iii) research on the forces and associated structural response resulting from tsunami bores impacting on land-based structures. This last area, is least studied. Consequently, there is a need for better understanding of tsunami bore impact on onshore coastal structures due to the relatively limited available research. Following the Indian Ocean tsunami in 2004 and the Tohoku tsunami in 2011, extensive study has started to be conducted in order to improve the understanding of tsunami impact loads and improve design guidelines. However, research has mainly focused on experimental investigation and has been mostly confined to small-scale models, while application of numerical models have been limited due to the high computational demand (Como & Mahmoud, 2013). As reviewed later in this thesis, there are many choices of computational methods to simulate the rapidly-varying violent flows of a tsunamis bore impacting a structure.

This thesis uses smoothed particle hydrodynamics (SPH) which is a meshless Lagrangian technique ideal for simulating highly non-linear free-surface phenomena such as tsunami waves. The rationale for choosing SPH is explained later in Chapter 2. By solving the 3-D Navier-Stokes equations, the SPH numerical modelling technique offers the potential for improved definition of wave characteristics and associated pressures on impacted structures. The capabilities of SPH to model wave-structure interaction for coastal engineering problems were presented by Dalrymple *et al*. (2009), Barreiro *et al*. (2013) and Altomare *et al*. (2015). Previous studies have demonstrated the applicability of SPH in quantifying tsunami wave characteristics within acceptable levels of accuracy when impacting vertical onshore structures (Cunningham *et al*., 2014). In addition to the laboratory experiments on tsunami wave impact on structures near shore, St-Germain *et al*. (2014) also conducted the numerical modelling using SPH on the basis of analogies between tsunami bores and dam break waves. Furthermore, the SPH technique has also been used to model other violent wave behaviour such as storm wave impact on vertical walls near shore, (Altomare *et al*., 2015). More details about the SPH software used herein, DualSPHysics, can be found in Crespo *et al*. (2015), Crespo *et al*. (2011), Crespo *et al*. (2013), Gomez-Gesteira *et al*. (2012a), Gomez-Gesteira *et al*. (2012b). Although Canelas *et al*. (2013) have coupled SPH to the discrete element method (DEM) for fluid-fixed structure interaction, none of the aforementioned studies have investigated the response of a deformable structure due to the hydrodynamics of a tsunami-like wave.

1.2 Objectives

The research presented in this thesis is intended to address the limited research on tsunamis impacting land-based structures by providing more detailed information on the tsunami-induced bore and structure interactions via numerical models. The numerical study is conducted using two software packages: (i) the fluid is simulated using the smoothed particle hydrodynamics (SPH) software DualSPHysics; (ii) the structural response is simulated using commercial finite element software ABAQUS. The ultimate goal of the research is to enhance present understanding of tsunami wave-structure interaction with a view to improving current design provisions. Therefore, the objectives of this thesis are to:

- Investigate tsunami wave inundation in built-up coastal areas with references to forces and structural response to wave inundation.

- Assess the performance of current design codes with reference to validated state-of-the-art numerical models.

- Improve resilience of residential buildings in tsunami risk areas.

1.3 Outline of the thesis

This thesis is structured as follows:

- Chapter 2 comprises of a critical review of published works on tsunami waves and structure interaction. It covers the characteristics of tsunami waves and the damage of coastal structures due to tsunami impacts. The existing design codes of tsunami resistant buildings and the current development on associated numerical modelling have also been addressed. The current building design codes do not specifically included the tsunami wave loads which is related to the limited research on this area. This chapter also highlights the emerging technology in the numerical modelling for violent waves including the smoothed particle hydrodynamics (SPH).

- Chapter 3 presents the basic theory of SPH and its application to the 2-D and 3-D modelling that are relevant to the topic of the current research. The SPH-based software DualSPHysics is introduced with its application to the dambreak case performed for the validation purpose for the current research.
- Chapter 4 presents the application of finite element software, ABAQUS, for simulating structures subjected to transient loads. The effectiveness of ABAQUS for modelling response of structure subject to impulsive loading is described as a means of model validation.
- Chapter 5 provides the results of hydrodynamic modelling of tsunami-like wave impacts on idealised coastal structures using DualSPHysics. The results include the improvement of the resilience of coastal structures by managing the orientation of coastal structures with respect to the direction of incoming tsunami-induced bores. The simulation of the effect of shielding and flow focussing has been conducted to study the influences on a group of idealised coastal structures.
- Chapter 6 provides the results of structural response modelling using ABAQUS on vertical structures made of timber. This chapter shows that the results of hydrodynamic modelling using DualSPHysics in terms of wave pressure-time history can be applied to finite element analysis of structures. The response of timber structures including deflections and stress distributions are reported.
- As a means of illustrating wider applicability of this method to regular storm wave and structures, Chapter 7 shows the applicability of DualSPHysics for simulating wind wave impacts on a recurve wall of a coastal defence with reference to the case occurring near Blackpool, UK.
- Chapter 8 presents the general and detailed conclusions of the current research and the recommendation for future research.

Chapter 2

Tsunami Risks to Coastal Structures

2.1 Introduction

Low lying coastal zones at elevations less than 10 m above mean sea level cover only 2 per cent of the world's land area but contain 10 per cent of the world's population (McGranahan *et al*., 2007). However, if this low lying area is situated near to seismically active areas, then it may become vulnerable to tsunami waves. Data show that tsunamis have been triggered by sea floor displacement associated with earthquake more often than other potential causes such as landslides, underwater mountain eruptions, or meteor impacts (Tinti *et al*., 2005; Papadopoulos and Fokaefs, 2005). The tsunami runup can reach more than 10 m high and inundates the land up to hundreds of meters from shoreline (EERI, 2010; EERI, 2011). The energy transported by a tsunami is sufficient to destroy many types of land-based structure including residential houses. The field observations after the 2004 Indian Ocean and 2011 Japan tsunami events show that most of residential buildings were destroyed and swept away by the tsunami-induced bore but some of buildings that survived had only minor damage (Chock *et al*., 2012; Saatcioglu, 2009; Ghobarah *et al*., 2006; Iemura *et al*., 2005; Nistor *et al*., 2000).

The performance of coastal structures during major tsunami and storm surge events were studied based on evidence obtained following field surveys (Saatcioglu *et al*., 2005; Mikami *et al*., 2012). Some engineered buildings that were designed and constructed with modern techniques survived tsunami waves with minor damage, while other buildings were either heavily damaged or totally collapsed. Failure of structures occurred where the design capacity was exceeded by unpredicted larger loads. Forces that significantly influence structures for the period of tsunami and storm surge events include hydrostatic uplift, hydrodynamic uplift and drag, debris impact, scour. Intensive research regarding the significance of aforementioned forces to a structure's behaviour is conducted extensively by experimental investigation and numerical modelling as will be described here. The structure's performance, the loads and research on tsunami and storm wave actions are outlined in the following sections.

2.2 Tsunami Waves

A tsunami has the same basic properties with other water wavges that occur on the free surface of a body of water. A tsunami has a wavelength, a period, a water height, and also can undergo shoaling, refraction, and diffraction (Segur, 2007). Dissimilar from sound waves that travel with the same speed and independent of the frequency and wavelength, the water waves with different wavelengths travel with different speed. Longer water waves have lower frequencies and travel faster than short waves, where the characteristic speed of propagation is approximately $\sqrt{gh}$, where g is the acceleration due to gravity and h represents the local water depth, measured from the bed elevation (at the floor of the ocean, or the bottom of the water tank) up to the quiescent free surface.

The term "long wave" is usually used for a water wave with a wavelength that is much longer than local water depth; alternatively, a body of water with depth much less than the wavelength of waves is called "shallow water" (Segur, 2007). A tsunami is one example of a very long wave. The Indian Ocean tsunami, for instance, had a wavelength (λ) about 100 km in the east-west direction that travelled through a 3 km deep (h) ocean. It is categorized as a long wave because the ratio of ocean depth to wavelength (h/λ) is much less than 1. This also means that the Indian Ocean was "shallow water" for the 2004 tsunami. The wave propagation speed of a tsunami is still $\sqrt{gh}$ in the deep ocean and starts to slow down in progressively shallower depth as the wave approaches shore where the sea bed begins to slope. The front of the wave must slow down earlier than the back of the wave. The consequence is that the back of the wave starts to converge with the front and the wave compresses horizontally as it moves near shore.

Since water is nearly incompressible, the wave must grow vertically to accommodate the accumulation of extra water if the wave compresses horizontally. This steepening of the wave can be unstable such that the waves eventually break. Once broken this displacement of the surface water that is barely noticeable in the deep open ocean can lead to a bore containing a large onshore mass flux which ultimately can become very destructive as it propagates. The motion of a tsunami in laboratory experiments and numerical models is often approximated using simplified forms which will now be discussed.

2.2.1 Solitary waves

A popular representation used to model tsunami runup experimentally and numerically is a solitary wave which has gained popularity since the early 1970s. The solitary wave was chosen by many researchers to model a tsunami wave because of numerous advantages. For example, Goring (1978) stated three reasons for choosing the solitary wave method; (1) theoretically the waves which have net positive volume eventually break up into a series of solitary waves if the propagation distance is sufficient, (2) although non-linear, a solitary wave can be described with just two parameters for analysis, (3) solitary waves propagate with constant form in constant depth. Yeh *et al*. (1994) added that it has become customary to use a solitary wave to model tsunami wave formation offshore because of its stable form and the leading wave of tsunamis often emerges as a solitary wave after a long period of propagation. Moreover, Li and Raichlen (2001) also reported that the solitary wave or the combinations of positive and negative solitary wave are often used to simulate the runup and shoreward inundation of the catastrophic waves.

The justifications used by researchers for the solitary wave, however, seems to be rather weak according to Madsen *et al*. (2008) for the reason that a potential problem with the solitary wave paradigm link to geophysical tsunamis has never really been established. By nature, a tsunami comprises a number of transient and non-periodic waves and these waves are gradually modified with respect to amplitudes, wave lengths and wave periods during the propagation from the ocean source to near shore areas. A significant amplification of amplitude and flow velocity takes place during the last stages of shoaling and runup. Madsen *et al*. (2008) argued that the strong input non-linearities combined with solitary waves were unrealistic. The finite amplitude of a solitary wave with the wave height to depth ratio H/h between 0.05 – 0.50 (where H is the wave height) for studying the runup, impact and scour of tsunamis may be interesting from an academic point of view, but when scaled up, these events are very short and closer to wind waves than to tsunami waves. As a consequence, conclusions related with tsunami based on solitary waves should be made with great care.

The solitary wave paradigm for tsunamis arises first after the theory of solitons invented by Zabusky and Kruskal (1965), where the theory is based on the KdV (Korteweg and de Vries) equation which can define the proper input waves for physical or mathematical models of tsunamis first derived by Korteweg and de Vries in 1895. Solitons are a special class of waves that propagate with permanent form, interact with other strongly non-linear waves without losing their identity, and related to solitary waves and localized so that they decay in infinity. Drazin and Johnson (1989) added that the word soliton covers the case when several of these waves are present simultaneously, and a soliton becomes a solitary wave when it completely separates from the other solitons. Once the KdV dynamics start to become active, it takes significant time and distance before the first soliton actually develops and separates from the rest of the wave train to become solitary wave.

Madsen *et al*. (2008) and Madsen and Schaffer (2010), explained that the threshold for soliton separation will not be reached neither in the deep ocean nor on the continental shelf. By using the non-linear KdV equations to calculate the propagation of tsunami in 4 km deep and 400 km wide ocean, for instance, a typical tsunami with 2 m amplitude needs to propagate 16000 water depths before the non-linear KdV becomes relevant and also needs 2 million water depths before a soliton will appear. Based on these results, Madsen (2010) claimed that the solitary wave is not suitable for being used to simulate the tsunami wave in respect to geophysical scale. However, solitary waves are highly repeatable in the laboratory and are very useful for physical and numerical modellers for comparison and validation purposes.

2.2.2 Long wave runup and inundation

The combination of huge runup elevations and extreme runup velocities of a tsunami produces more devastating effects compared with other wave events such as tide and wind waves. On steep and mild beaches the tsunami behaves differently. It has been rarely addressed that the flow velocity during runup and also rundown is more crucial for the impact rather than the height itself. The influence of beach slope on flow velocity was reported by Madsen and Fuhrman (2007) for the Indian Ocean tsunami where the flat beaches such as Patong, Kalim, Kamala, Bang Tao and Khao Lak experienced major destruction while steeper beaches such as Surin, Karon, Kata, Kata Thani and at the Similan Islands were left almost untouched.

2.2.3 Tsunami bore impact forces

The tsunami propagates toward the shoreline and runs up the shore as a hydraulic bore after breaking when the water depth is approximately equal to the incident wave height. This phenomenon was video-recorded during the 2004 Indian Ocean Tsunami event (Nouri *et al*., 2010). Even though the wave has been transformed into bore, it possess an enormous force as evidenced by structural failures and also displacement of large debris such as boats that were carried up to four kilometres inland (Nistor *et al*., 2005). The analytical and experimental study to quantify the hydraulic bore force was initiated by solving non-linear shallow water equations and also investigating the reflection of a bore from a rigid vertical wall (Stoker, 1957). A solution for the impact of a two-dimensional fluid wedge on a vertical wall was presented by Cumberbatch (1960) and this approach was adapted by Cross (1967) to study the properties of surges and their impact on a vertical wall. A further development of the force due to a surge includes gravity to produce the maximum force for a bore that can be simplified as follows:

$$F = \frac{1}{2}\rho g b(H+h)^2 + \rho b H c^2 \tag{2.1}$$

where ρ is the sea water density, b is the width of the wall, H is the incident bore height at the wall, h is the still water depth, and c is the celerity and can be determined from

$$\frac{c^2}{gh} = \frac{1}{8}\left[\left(2\frac{H}{h} + 3\right)^2 - 1\right] \tag{2.2}$$

The investigation of solitary waves and the corresponding bores and surges on dry-bed with vertical wall was performed comprehensively by Ramsden and Raichlen (1990), Ramsden (1993) and Ramsden (1996). The experiment was conducted using a water tank with dimensions of 0.40 m wide, 0.61 m deep and 36.60 m long. It was found that the pressure distribution during bore impact was non-hydrostatic, so it was argued that the shallow water equations could not be used to determine the pressures and forces following the bore impact. Ramsden (1993) noticed that the maximum measured forces due to solitary waves, bores, and surges is less than the computed forces from the maximum measured runup based on hydrostatic condition. The reason for this is due to the existence of vertical flow acceleration. The dry-bed testing showed that the model of Cross (1967) in Equation (2.1) under-predicts the measured forces due to bores by 20% to 50%. The forces were gradually increased to an approximately constant value, and no impulsive force during runup exceeded this constant force.

2.3 Performance of Structures during Tsunami Events

2.3.1 Performance of timber-frame houses

The condition of timber frame buildings after the 2011 earthquake and tsunami events in Japan have been reported by Fraser *et al*. (2013). Damage levels of timber buildings were assessed using damage scales ranging from D0 (no damage) to D4 (collapse) with descriptions of damage, occupancy suitability and level of required repair for a timber frame. The damage scales are shown in Table 2.1. Based on tsunami damage scale in Table 2.1, most of timber frame buildings in observed areas, including Kamaishi City and Kesennuma City, experienced damage level D4, which is complete collapse. For comparison, steel frame buildings suffered damage level D1-D3 and reinforced concrete buildings reached damage level D1-D2. Importantly, some of them survived with less damage due to significant sheltering or shielding by other more robust structures such as steel or concrete frame buildings.

Table 2.1 Tsunami damage scale for timber frame building (Fraser *et al*., 2013)

Damage Level:	Description:
No damage (D0)	No visible damage to the structure observed during the survey. Suitable for immediate occupancy.
Light damage (D1)	Flood damage to contents. Some non-structural (fittings, windows) damage. Damage is minor and repairable. Suitable for immediate occupancy.
Moderate damage (D2)	Out-of-plane failure or collapse of parts of or whole sections of masonry infill walls and windows at ground storey. Repairable damage from debris impact to structural members (columns, beams, walls). No structural member failure. Scouring at corners of the structures leaving foundations partly exposed but repairable by backfilling. Unsuitable for immediate occupancy but suitable after light repair.
Heavy damage (D3)	The structure stands but is severely damaged. Infill panels above the 1st storey have been damaged or have failed. Structural and non-structural members have been damaged. Failure of a few structural members which are not critical to structure stability (e.g. failure of infill concrete walls). Roofs are damaged and have to be totally replaced or repaired. Significant scouring at corners of the structures leaving foundations exposed, with minor repairable tilting. Structure requires extensive repair and is unsuitable for immediate occupancy.
Collapse (D4)	Partial or total collapse of the building. Collapse of large sections of foundations or structure due to heavy scouring or debris impact. Excessive foundation settlement and tilting beyond repair. Damage to the structure cannot be repaired and must be demolished.

Fraser *et al*. (2013) investigated 2-storey timber houses that suffered soft-story damage as shown by Figure 2.1; soft-story damage is typical of building damage due to earthquake shaking. Soft story damage usually occurs when the first story columns of a building have much less stiffness than other columns above them. The first story column with less stiffness will fail if they support excessive vertical and lateral loads in combination. However, based on observation in un-inundated areas where timber building performed well due to ground shaking, the studies by Fraser *et al*. (2013)

indicate that the soft-story failures were caused by the tsunami rather than earthquake lateral loading. The second story of house in Figure 2.1 appears to have remained intact because of the existence of a supporting central steel beam but also shows the devastating effect of tsunamis. In contrast, to design a reinforced concrete building in the tsunami-prone coastal areas, a balanced design approach (for both earthquake and tsunami) is necessary since the reinforced concrete frames with an open ground storey are effective to reduce tsunami forces, however, such soft storey failure mechanism tend to occur under severe seismic condition.

Figure 2.1 Soft-storey collapse of a 2-storey timber house Fraser *et al*. (2013)

The failure mechanism of timber-frame buildings under tsunami loads has been explained by Becker *et al*. (2011). The damages of timber-frame houses under rapid onset flooding were categorized into three groups, namely (1) submergence of building to a depth that is unsafe for occupants, (2) structural failure that causes collapse of buildings and harms inhabitant, (3) the uplift pressures and lateral forces caused by flood that exceed the capacity of the building's design load. Those three mechanisms are referred to as fill, collapse, and float. Lateral load resistance of simple timber house is shown in Figure 2.2 (Becker et al., 2011). It is assumed that lateral loads due to tsunami flow are perpendicular to a single wall of building. Lateral load resistance by the house frame platform consists of four main components: foundation, floor, walls and roof. The structural frame system transfers externally applied loads to the house foundation through the load path. Load carrying components of a timber house include the sheathing, studs, floor, roof, nailed connections, shear-walls and foundation anchors.

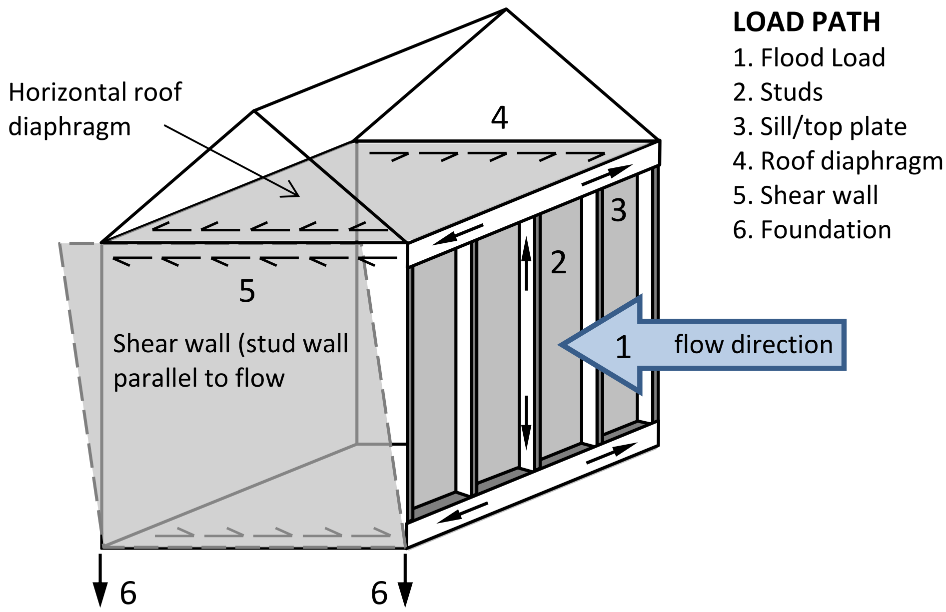

Figure 2.2 Flood response load path of simple timber-frame house (Becker *et al*., 2011)

Robertson *et al*. (2007) also reported on the poor performance of residential structures made of light-frame wood and unreinforced masonry under violent wave impact during the 2005 Katrina storm surge. Similar to tsunamis impact results, following the storm surge the only remaining indication of a residential building in many coastal areas was a ground-floor slab on site and pieces of debris deposited at the high water mark. The vulnerability of residential timber houses against tsunamis was convincingly demonstrated in the numbers stated by Suppasri *et al*. (2012) where 115,163 houses were reported heavily damaged, 162,015 houses were moderately damaged and 559,321 houses were partially damaged due to the 2011 East Japan tsunami.

2.3.2 Performance of un-reinforced masonry walls

During the 2004 Indian Ocean tsunami, un-reinforced masonry walls suffered punching shear failures due to the tsunami waves pressure applied perpendicularly to the wall plane. This pressure resulted in large holes on the walls and sometimes removing the masonry wall almost entirely, as illustrated in Figure 2.3. The remaining walls around the frames did not show any sign of diagonal tension cracks, the typical failure caused by seismic excitations. In a simple house, un-reinforced masonry walls usually support roof dead loads and in the case of the wall suffering severe damage, this may trigger the collapsed of the entire structure.

(a) Ghobarah *et al*. (2006) (b) Saatcioglu *et al*. (2005)

Figure 2.3 Damage of un-reinforced masonry walls due to tsunami

2.3.3 Performance of non-engineered buildings

A non-engineered residential building was reported as the most severely damaged type of structure by number during the Indian Ocean and East Japan tsunamis (Saatcioglu *et al*., 2005; Mikami *et al*., 2012). A non-engineered residential building is typically the low-cost residential house built in coastal areas in developing countries including Indonesia. The roofs of this low-cost house either have light corrugated metal coverage or clay tiles. A typical house is predominantly made of homogeneous material such as wood or brick and it is not generally designed to resist large lateral loads.

Saatcioglu *et al*. (2005) stated that in Indonesia and Thailand, the non-engineered two-storey low-rise buildings were mostly built using in-situ concrete, with small-sized columns cross-section, of area approximately 200 mm^2. The reinforcement ratio of small columns containing 4 smooth or deformed corner bars with 8 mm diameter is approximately 0.5%. The capacity of this column is far below the moment imposed by tsunami forces. Figure 2.4 shows column failures in non-engineered reinforced concrete frame buildings due to large tsunami wave pressures. Most columns failed because of debris impact at mid-height. Floating large debris like cars, boats and building produce impact forces larger than wave pressures.

Figure 2.4 Damage of non-engineered low-rise building (Nistor *et al*., 2010)

In addition to impact loading, Robertson *et al*. (2007) confirmed that columns can be damaged by debris impact and water-damming effect that occurs when large debris becomes lodged against structures and disrupted the water flows causing significant drag and inertia forces. A shipping container is a common type of debris that can cause substantial fluid forces on structures for this case. Figure 2.5 illustrates the debris impact loading where in this case the columns that support building roof were severely damaged by shipping container impact.

Figure 2.5 Damage of columns caused by debris impact (Robertson *et al*., 2007)

2.3.4 Performance of engineered buildings

Numerous low to mid-rise reinforced concrete frame buildings which appeared to have been engineered successfully survived tsunami waves during the 2004 Indian Ocean tsunami (Ghobarah *et al*., 2006). Most of them suffered minor damage to non-structural elements, such as masonry wall damage in the lowest storey. Engineered structural elements have proven reliable in tsunami disaster even though those buildings are originally built to withstand earthquake loads that are likely more often to occur.

Ghobarah *et al*. (2006) reported that in Banda Aceh and Thailand, a well-constructed reinforced concrete structure survived high tsunami run up with minimum damage limited to non-engineered part of building including the broken windows and doors, and the failed thin masonry walls at first floor. An example of a well-constructed building in Banda Aceh is shown by Figure 2.6(a). The tsunami waves were very turbulent as they come to shore and when receding. Therefore, sand and granular materials under shallow foundation suffered from scouring. This occurred to a three-storey building among other buildings in Khao Lak, Thailand, as shown in Figure 2.6(b). This kind of damage was observed in the area where the run up height exceeded 8 m.

(a) (b)

Figure 2.6 Minor damage of well-engineered buildings (Ghobarah *et al*., 2006)

2.3.5 Performance of bridges

Bridge structures along the coast are repeatedly subjected to hydrodynamics loads, for instances, those due to storm surges (Robertson *et al*., 2007) and tsunamis (Ghobarah *et al*., 2006) as clearly exposed in Figure 2.7. The hydrodynamic loads due to tsunami and storm surge on a coastal bridge include hydrostatic pressure, buoyancy force, fluid flow drag and surge impingement (Yim, 2005). These loads are able to initiate fracture or even collapse, affect structural stability or dislodge of coastal structures from their bases.

(a) Damage caused by hurricane Katrina (Robertson *et al*., 2007)

(b) Damage caused by Indian Ocean tsunami (Ghobarah *et al*., 2006)

Figure 2.7 Damage of bridges caused by storm wave and tsunami

During the East Japan tsunami, EERI (2011) reported a number of railway bridges that failed due to large sustained lateral forces caused by wave pressure on the bridge spans. The acting lateral forces were sufficient to break seismic anchorages or even pull down the overpass piers, as shown in Figure 2.8(a). In many highway bridges, seismic lateral blocking and ductile anchorage of girder were ineffective to resist uplift pressures. Scouring was reported to cause the collapse of a highway overpass in Rikuzentakata, Japan, during the 2011 tsunami event. A brand-new highway overpass consisting of three skew spans had collapsed as shown in Figure 2.8(b). All three reinforced concrete piers and two abutments were still intact and showed no signs of damage, however, there was significant scour behind the abutments. The three deck sections had been dislocated from atop the piers to a location approximately 40 m inland.

(a) (b)

Figure 2.8 Damaged of highway bridges in Japan due to tsunami (EERI, 2011)

Dislodgement of the bridge deck was assumed to be caused by buoyant forces due to the large volume of air that entrapped between girders and the bulkheads as the inundation increased. The field measurements of the remaining deck section indicated that when fully submerged the residual weight of the deck is only 11% of its original weight (EERI, 2011). This means small additional amount of uplift forces will dislocate the deck sections. Although concrete shear keys and large diameter steel dowels embedded vertically into the end of bulkhead at each deck section were sufficient to resist lateral forces when the earthquake happened, they were unlikely to resist uplift forces.

2.3.6 Shielding and focusing effects

A field investigation following the 2011 Japan tsunami event in Sendai reported in Robertson *et al*. (2013) concerned the role of multiple leading columns of a building providing a shielding against the tsunami wave flow for the back columns. That situation was then modelled in a laboratory by simulating water flow that strikes columns with configuration as can be seen in Figure 2.9. The forces measured on the columns’ surface without shielding effects were compared with forces on columns with shielding effects. Two kind of shielding effects called symmetric and offset shielding were investigated, along with some variations regarding the size of tested columns (see Figure 2.10).

Figure 2.9 Wave impact testing on multiple columns (Robertson *et al*., 2013)

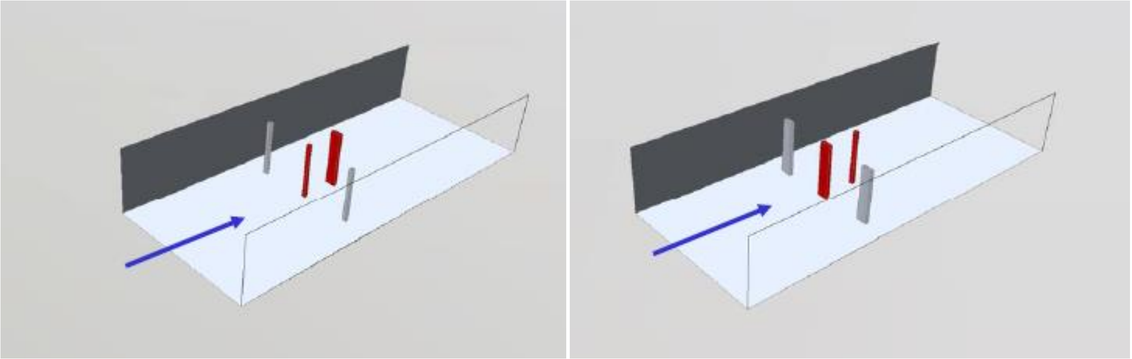

(a) Symmetric shielding (Robertson *et al*., 2013)

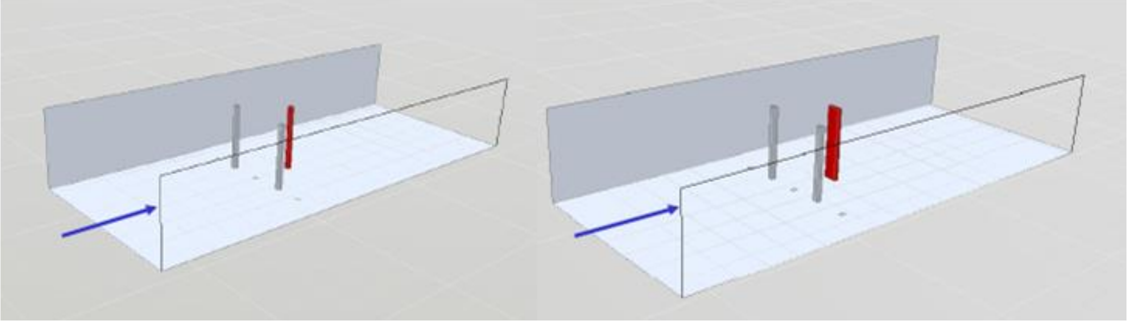

(b) Offset shielding (Robertson *et al*., 2013)

Figure 2.10 Illustration of symmetric and offset shielding columns

The test results show that there was a significant drop in load with ratio originally from 1 up to 0.64 for a 2x2 cm column shielded by 3-6x2 cm columns in the symmetric shielding case. On the other hand, an increase of load about 24% was measured on the surface of a 6x4 cm column shielded by 3-2x2 cm columns for the offset shielding case. A close prediction to the second results was obtained by Robertson *et al*. (2013) who performed a study on flow focusing effects for an idealized building as illustrated in Figure 2.11. The maximum increase of 25% was measured for the use of effective wake angle θ = 35° during the test. The amplification of forces for different values of θ is shown in Table 2.2. The flow focusing of wave will be examined in this work since it clearly gives significant effects to the neighbouring buildings.

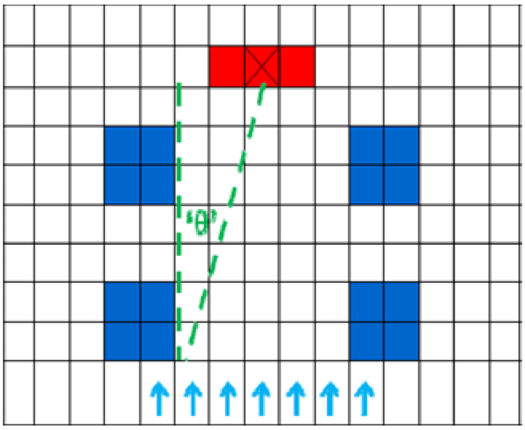

Figure 2.11 Illustration of flow focusing on buildings (Robertson *et al*., 2013)

Table 2.2 Amplification of wave forces by flow focusing effects (Robertson *et al*., 2013)

Effective Wake Angle, θ	**0**	**10**	**20**	**35**	**≥ 55**
Amplification for symmetrical layout	1.0	1.0	1.25	1.25	1.0
Amplification for non-symmetrical layout	1.0	1.0	1.15	1.15	1.0

A real example of flow focusing occurred in Onagawa during the 2011 Japan tsunami event. Based on field evidence (Robertson *et al*., 2013) as illustrated in Figure 2.12(a), the researchers found that the large buildings which survived (marked with A) caused a “flow focusing” to occur between and around those buildings. The focusing effect (or channelization) was causing the overturning of concrete and steel buildings (marked with C), and at the end of that channel causing devastation to a major steel-framed shopping structure (marked with D). “Shielding effects” were experienced by buildings marked with B, protecting building B from serious damage.

Similar damaging effects were also observed during the drawdown which caused the downstream failures. As shown in Figure 2.12(b), the focusing during the drawdown flows caused a pedestrian bridge to be moved from position B to B’ and also lifted up an enormous slab-on-grade section and twisted it around (from position A to A’) and causing significant scours between these two buildings. Based on this evidence, the focusing effect is clearly important, and will be considered in this study.

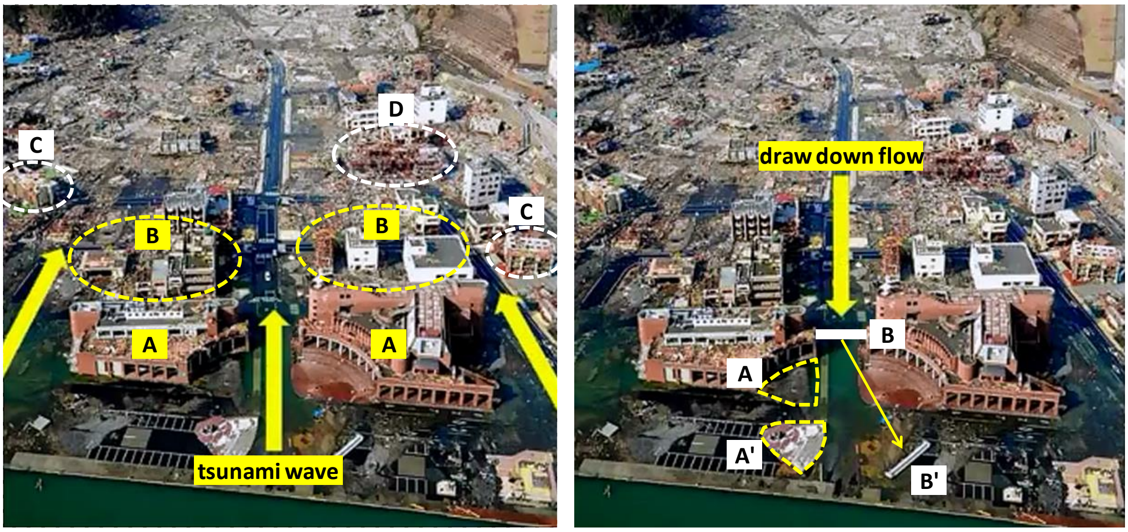

(a) Run-up (b) Run-down

Figure 2.12 Flow focusing in Onagawa during the 2011 Japan tsunami (Robertson *et al.*, 2013)

2.4 Existing Design Codes for Tsunami-Resistant Buildings

Buildings should be designed to be able to withstand the combination of loads that act vertically and horizontally. Determining site-specific loads is one of the steps that are important in the design process of buildings, as stated in FEMA P-55 (2011) which provides guidance for designing, constructing and maintaining residential buildings in coastal areas. In addition to standard wind and seismic loading (CCBFC, 1995) for designing coastal buildings, other than vertical dead and live loads, there are several types of loads that should be considered related with natural hazards such as coastal flood, wind and seismic loads that act laterally. It should be noted that those lateral loads are influenced by site and building characteristics. For example, the site characteristics that affect flood loads are the orientation of water flow and the soil type related with scour potential, while the building characteristics that affect wind or seismic loads are the building geometry and weight, respectively. According to FEMA P-55 (2011) the summary of typical loads and characteristics that are important for building design can be seen in Figure 2.13.

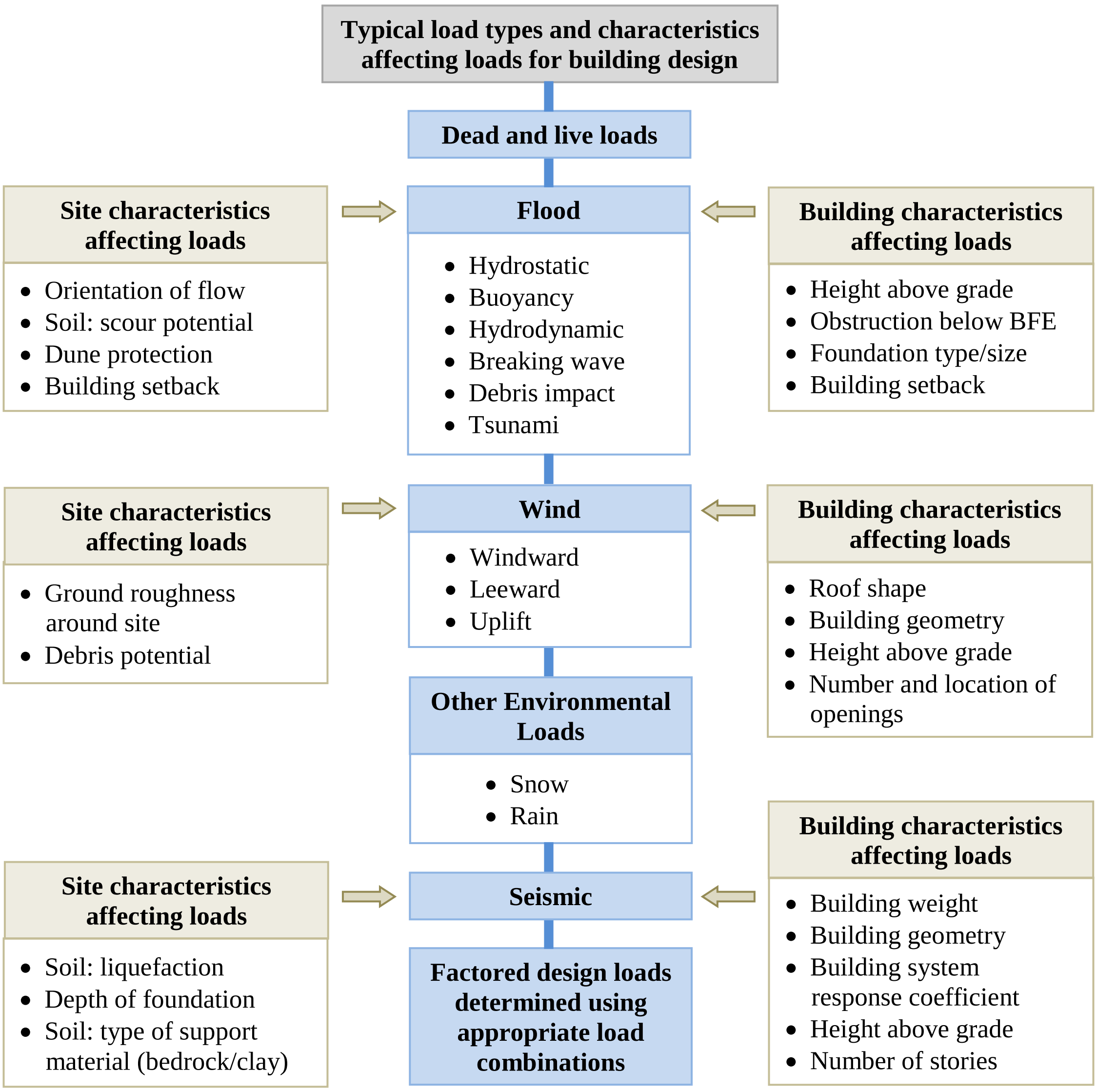

Figure 2.13 Summary of typical loads and characteristics for building design (FEMA P-55, 2011).

The following current design codes can be used as guidelines that provide equations to estimate the loads acting on structures during flood events (Yeh *et al.*, 2005; Yim, 2005; FEMA P-646, 2008; FEMA P-55, 2011):

- The City and County of Honolulu Building Code (CCH) Chapter 16 Article 11, published by the Department of Planning and Permitting of Honolulu, Hawaii, covers regulations that apply within flood hazard districts and for developments adjacent to drainage facilities.
- The 1997 Uniform Building Code (UBC 97) Appendix Chapter 31, published by the International Conference of Building Officials (ICBO) covers special construction topics in flood-resistant construction.
- The 2000 International Building Code (IBC 2000) published by the International Code Council provides information on flood design and flood resistant construction.
- The ASCE 7-98 (ASCE 7) published by American Society of Civil Engineers Committee 7 describes the different forces involved with flood and wave loads.
- The Federal Emergency Management Agency Coastal Construction Manual (FEMA CCM) contains expressions for flood loads which include wave loads.

The scope of the codes implies that within flood risk areas, the structures be designed and constructed to resist the effect of flood hazards and loads. This is to include all new and existing building or portion of building construction. FEMA P-646 (2008) classifies flooding-prone areas as A-zones and V-zones. A-zones are areas that are prone to flooding but not subject to wave height of more than 3 feet (~1 meter) and V-zones are the coastal high-hazard areas that have wave heights greater than 3 feet (~1 meter) or subject to high velocity wave run-up or wave-induced erosion. Shallow foundation types are not permitted in V-zones unless the natural supporting soils are protected by scour protection. Design and construction of coastal building structures in V-zones should consider the following loads: hydrostatic, hydrodynamic, impact, surge, wave and breaking wave loads. To reduce the risk due to excessive loads on the structural frame, elements of buildings such as walls and partitions parallel to the expected direction of water flow are required to break away, especially when situated below the flood elevation. The main building structure must be adequately anchored and connected to a substructure system to resist lateral and uplift forces. Moreover, habitable space in building structures must be elevated above the minimum base flood elevation by such means as posts, piles or piers.

Nistor *et al*., (2000) stated that there are three important parameters for estimating the magnitude and application of tsunami forces, namely inundation depth, flow velocity, and flow direction. Those three parameters mainly depend on tsunami wave height and wave period; coastal topography; and roughness of the coastal inland. Several forces that should be considered as part of tsunami load effects for the design of vertical evacuation structures and coastal bridges are: (1) hydrostatic forces; (2) buoyant forces; (3) hydrodynamic forces; (4) impulsive forces; (5) debris impact forces; (6) debris damming forces; (7) uplift forces; and (8) additional gravity loads from retained water on elevated floors (Nistor *et al.*, 2000; Yim, 2005; FEMA P-646, 2008; Robertson *et al.*, 2007). This thesis will examine the hydrostatic, hydrodynamic and impulsive forces on structures.

2.4.1 Hydrostatic forces

A structure experiences hydrostatic forces when motionless water acts perpendicular to the surface of the component of interest. Imbalance in pressure due to differential water depth on opposite site of a component can create a net force. This force may not be pertinent for a structure with fixed breadth, around which the water can flow quickly and fill in on all sides. Hydrostatic forces are usually significant for long structures such as sea walls. Hydrostatic buoyant forces should be considered when the ground floor of a building is watertight. In this condition, the hydrostatic forces should be calculated for individual wall panels. The horizontal hydrostatic forces (Figure 2.14) on a wall panel can be calculated using Equation (2.3):

$$F_h = p_c A_w = \frac{1}{2}\, \rho_s g b h_{max}^2 \tag{2.3}$$

where p_c is the hydrostatic pressure, A_w is the wetted area of the panel, ρ_s is the fluid density including sediment (1200 kg/m^3), g is the gravitational acceleration, b is the breadth (width) of the wall, and h_{max} is the maximum water height above the base of the wall at the structure location.

The Japanese design method for tsunami wave loading, proposed by Okada *et al*. (2005), considers both static and dynamic load together. For a tsunami wave with no break up, the force per unit length of the wall is taken as an equivalent hydrostatic load and this leads to a resultant force equal to nine times the hydrostatic force of inundation depth h (Thusyanthan and Madabhushi, 2008). In the case of break-up, the tsunami force increase with added a triangular pressure distribution with base pressure 2.4 ρgh (see Figure 2.15). This leads to an equivalent force of tsunami around 11 times the hydrostatic force of inundation depth h.

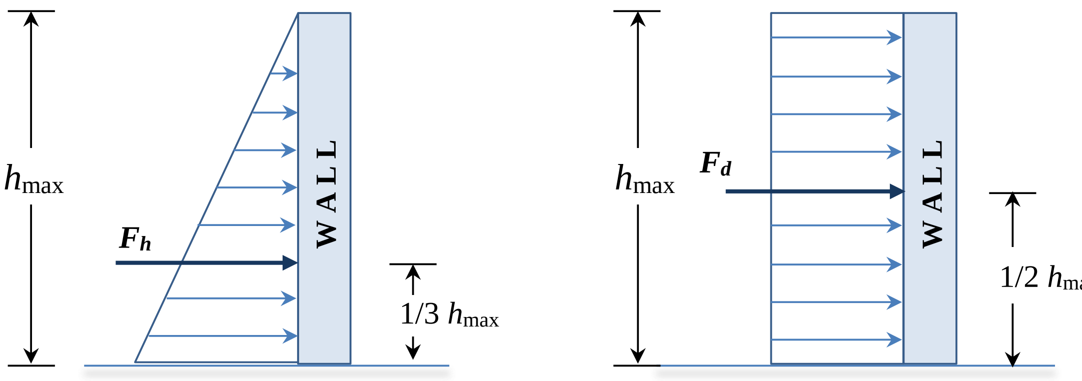

Figure 2.14 Hydrostatic force (F_h) and associated hydrodynamic force (F_d) distribution (FEMA P-646, 2008)

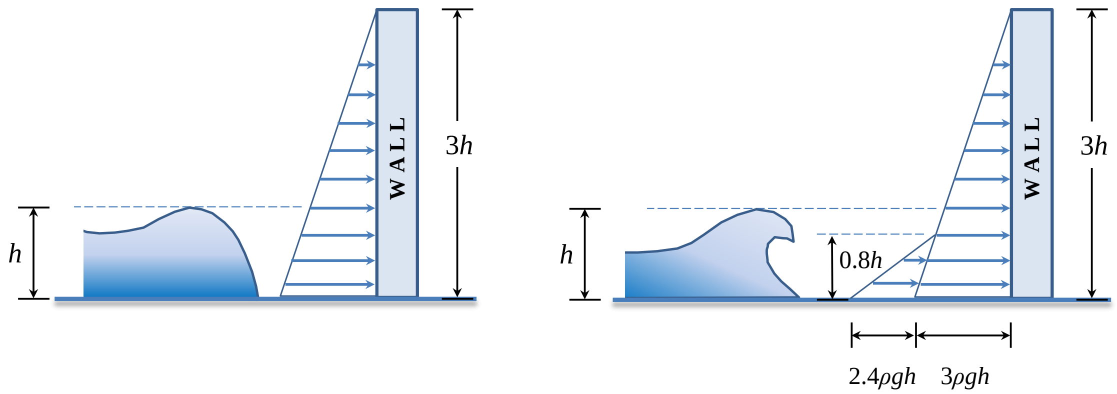

Figure 2.15 Japanese design method assumes tsunami wave pressure is equivalent to three times the hydrostatic pressure (Thusyanthan and Madabhushi, 2008).

The US Army coastal engineering research centre also provides guidance (USACE, 1990) on wave force exerted on shoreward vertical wall. The guidance by US Army is based on work by Cross and Camfield, where the tsunami force is 4.5 $\rho g h^2$. This is in line with the Japanese design method that approximates the tsunami impact pressure to be nine times the hydrostatic load. The US FEMA CCM provides the total wave load (hydrodynamic and hydrostatic) on a vertical wall (height $\geq$ 2.2 h) of a coastal residential building to be about 11 times the hydrostatic force with inundation depth, h.

2.4.2 Hydrodynamic forces

Hydrodynamic forces are applied to the structure when water flows around a structure at moderate to high velocity. Hydrodynamic forces are also known as drag forces and are a function of fluid density, flow velocity and structure geometry. Hydrodynamic forces are a combination of lateral forces generated by the pressure forces from the moving mass of water and the friction forces produced by the water flows around the structure or component. Hydrodynamic forces can be computed using Equation (2.4) (FEMA P-55, 2011):

$$F_d = \frac{1}{2} C_d \, \rho \, V^2 A \tag{2.4}$$

where F_d is horizontal drag force, C_d is the drag coefficient which is recommended to be taken as 2.0 for square rectangular piles and 1.2 for round piles, ρ_s is the fluid density, V is velocity of water, A is surface area of obstruction normal to flow. In addition to drag coefficient, its value also depends on ratios of width to depth (w/d) and width to height (w/h) of submerged surface area, as shown in Table 2.3.

Nistor *et al*. (2000) argued that since the hydrodynamic forces is proportional to the square of the bore velocity, uncertainties in estimating bore velocity cause large differences in the value of resulting hydrodynamic forces. Tsunami-bore velocity and direction can vary significantly during a tsunami event. Recent estimations of the velocity usually assumed that a conservatively high flow velocity strikes the building at normal angle. Moreover, the results of run-up, run-down and direction of velocity are not addressed in the existing design codes. FEMA P-55 (2011) defined the bore velocity as given in Equation (2.5):

$$u = \sqrt{gd_s} \tag{2.5}$$

where u is the bore velocity, d_s is the inundation depth.

Table 2.3 Drag coefficient for ratios of (w/d) and (w/h)

Width to Depth Ratio (w/d or w/h)	Drag Coefficient (C_d)
1 – 12	1.25
13 – 20	1.30
21 – 32	1.40
33 – 40	1.50
41 – 80	1.75
81 – 120	1.80
> 120	2.00

To improve the existing formula found in literature, Chock *et al*. (2011) and Robertson *et al*. (2013) developed a semi-empirical method to predict bore forces on a vertical wall

$$F = \frac{1}{2}\rho g h_b^2 + \rho h_j v_j^2 + \rho g^{1/3}\left(h_j v_j\right)^{4/3} \tag{2.6}$$

Equation (2.6) allows for the estimation of the peak impact force per unit width on a vertical wall following simplified model shown in Figure 2.16. This equation was based on a series of experiments performed in the large wave flume (LWF) at Oregon State University. The prediction of Equation (2.6) is compared (see Figure 2.17 for the results) with other equations such as equation by Cross (1967) that studied bores propagating over a dry-bed and impacting the wall,

$$F = \frac{1}{2}\rho g h_b^2 + \rho h_b v_j^2 \tag{2.7}$$

where ρ is the mass density, g is gravitational acceleration, h_b is the height of the bore and v_j is the propagation speed.

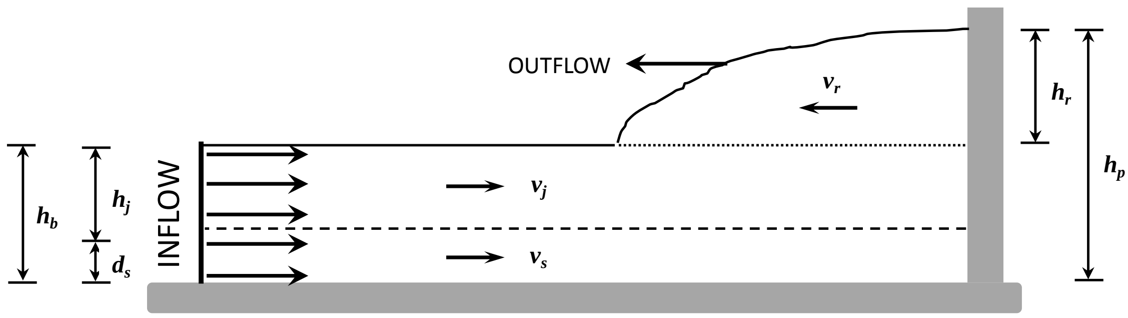

Figure 2.16 Hydrodynamic force on wall due to bore impact

Asakura *et al*. (2000) proposed Equation (2.8) that was based on experiments with a beach slope and a dry flat shoreline, and also a vertical seawall in front of test specimen.

$$F = \frac{1}{2}\rho g \left(3h_j\right)^2 \tag{2.8}$$

Using an experimental setup similar to Asakura *et al*. (2000), Fujima *et al*. (2009) proposed Equation (2.9) based on the maximum water inundation level and structure distance from the reef break

$$F = 1.3\rho h_j v_j^2 \tag{2.9}$$

Regarding the case of a bore travelling over a still water, the Overseas Coastal Area Development Institute (OCADI) of the Ports and Harbours Bureau of Japan (OCADI, 2009) proposed an equation to determine lateral force per unit width on the wall

$$F = 3.3\rho g h_j^2 + 2.2\rho g h_j d_s \tag{2.10}$$

The equation based on triangular pressure distribution above the still water with height $3h_j$ and base pressure given by $2.2\rho g h_j$. The base pressure is constant throughout the depth of still water.

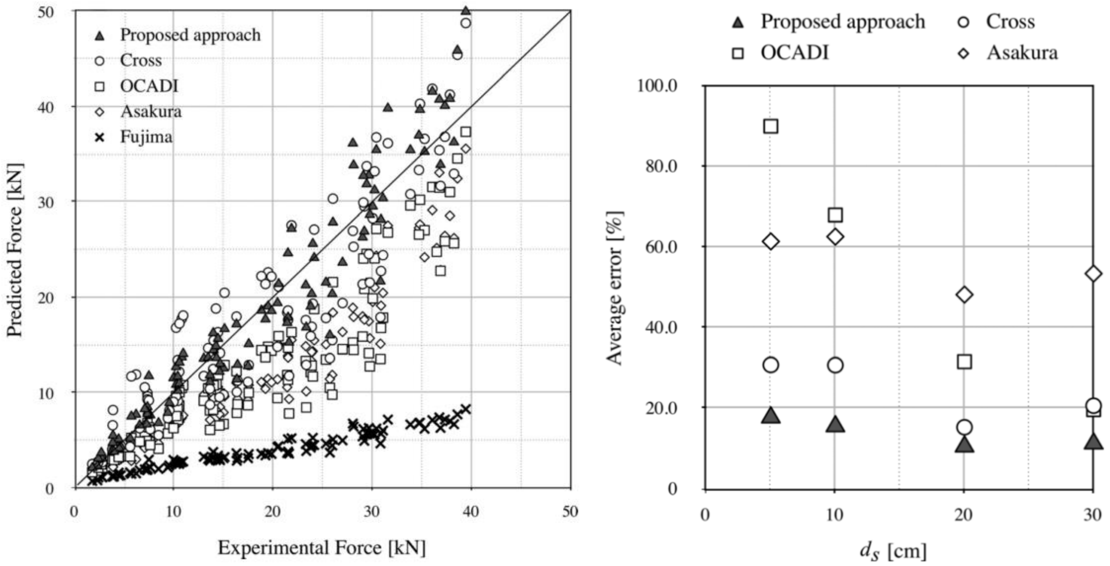

(a) (b)

Figure 2.17 Comparison of force prediction (Robertson *et al.*, 2013)

The efficacy of Equations (2.6), (2.7), (2.8), (2.9) and (2.10) in predicting the force of tsunami impact on the vertical surface of a structure is depicted in Figure 2.17. The solid diagonal line in Figure 2.17(a) is an ideal trend on which the points would lie if the predicted results equalled the experimental results. Equations (2.6) proposed by researchers in Oregon State University (OSU) provides good estimate of the peak experimental force and also gives smaller average error around 10% for all standing water levels.

2.4.3 Lateral load design for tsunami, seismic and wind loads

A comparison between earthquake, wind and tsunami wave dynamic pressure was made by Saatcioglu *et al*. (2005). Firstly, an expression that is applicable for estimating uniform dynamic pressure of tsunami wave impact given by (Hiroi, 1919) is introduced,

$$p = 1.3\gamma H_w \tag{2.11}$$

where p is uniform lateral pressure, γ is the specific gravity of sea water (10.3 kN/m^3), H_w is wave height in m. Then, the hydrodynamic tsunami wave pressure obtained from Equation (2.11) is compared with wind design pressure specified in the National Building Code of Canada (CCBFC, 1995) on building located at the coastal city of Vancouver, Canada. From the comparison, it was found that the tsunami pressure at the first floor could be approximately 26 times the design wind pressure in Vancouver, explaining the widespread damage to masonry wall observed within the first stories of the most buildings.

For a comparison between design lateral forces due to wind, seismic and tsunami, Saatcioglu *et al*. (2005) used a sample case of a 6-storey, 3-bay reinforced concrete frame structure in Vancouver, Canada, loaded with 5 m tsunami wave height. The comparison of lateral forces as depicted in Figure 2.18 shows that the base shear due to tsunami was about twice the base shear caused by the 50-year return period wind speed (100-110 km/h) pressure.

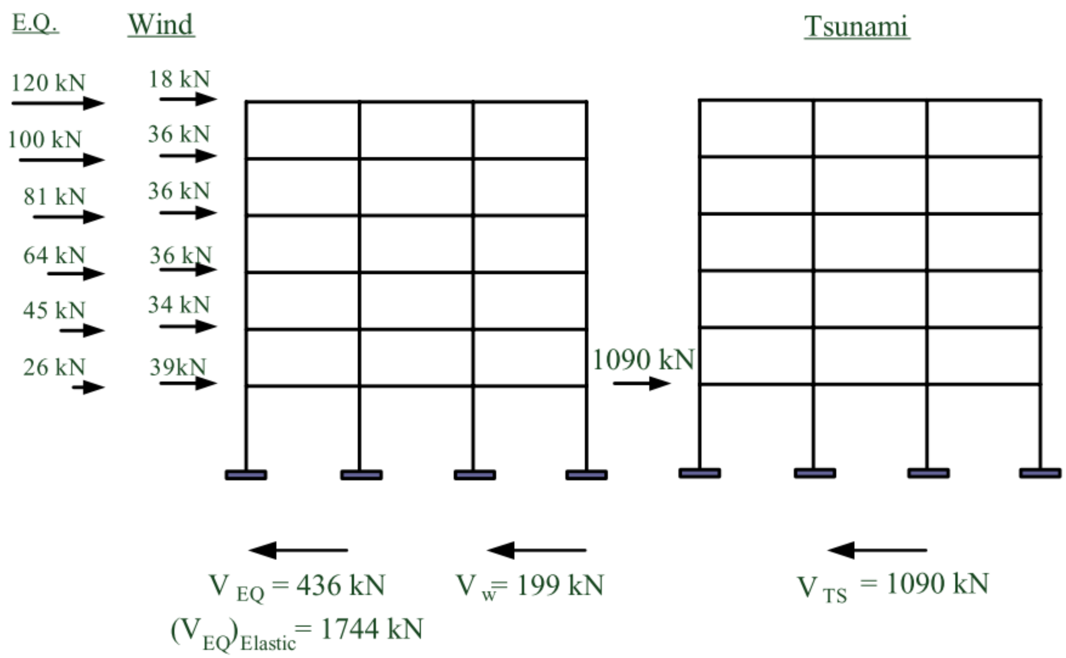

Figure 2.18 Comparison of lateral force due to earthquake, wind and tsunami for a case of 6-storey building (Saatcioglu *et al*., 2005)

From the total base shear due to tsunami, 60% of that caused by elastic seismic force and 2.5 times the inelastic seismic design base shear for a ductile moment resisting frame building. This comparison provides indications for the magnitude of tsunami and its effect on building compared with other lateral loads that are usually taken into account in designing a building.

The tsunami hydrodynamic forces exerted on the building are much larger than typical lateral design forces (e.g. wind and seismic). Non-structural components of building structure will likely break away under tsunami hydrodynamic loads, thereby reducing the tsunami load on the structural frame. However, structural walls of building must be able to resist the tsunami loads so that they continue to support the building gravity loads.

This thesis aims to examine the impact force on structures due to tsunamis and their structural response. Later in this thesis in Chapter 4, the choice and validation of methodology to simulate the structural response using the finite element (FE) method is presented. Now methods for simulating the fluid motion are discussed.

2.5 Existing Numerical Modelling of Tsunamis

To enable communities to respond before a tsunami disaster occurs so that the loss could be minimized, a forecasting system is required (Behrens and Dias, 2015). The forecast needs knowledge of tsunami runup and inundation zones, the investigation of the geological evidence and the impact of past tsunamis. Since tsunamis are rare events, it is often difficult to collect data from the past events and often relying on an analysis of sedimentary deposits. Therefore, computer models can help to describe past events and provide potential hazard scenarios in the future. However, due to the uncertainties about many tsunami features, it is challenging to simulate and analyse the water motion accurately and for operational purposes model validation is essential.

2.5.1 Modelling approaches

Modelling tsunami waves requires a description of the physical phenomena in terms of mathematical equations and appropriate methods to solve the equations. A number of approaches are available to formulate the tsunami wave behaviour as a set of hydrodynamic equations and conservation of laws.

(a) Shallow water equations

Linear and non-linear shallow water theory has traditionally been used in the modelling of tsunami and successfully describes the phenomenon up to a water depth corresponding to near-shore regions. In particular, it is assumed that the wave height h is small compared with the mean water depth, H, ($h \ll H$), and the characteristic wavelength L is large compared with the water depth ($H \ll L$). The non-linear set of shallow water equations can be derived given by:

$$\frac{\partial h}{\partial t} + \nabla \cdot \left(\mathbf{v}(H + h)\right) = 0 \qquad (2.12a)$$

$$\frac{\partial \boldsymbol{v}}{\partial t} + \mathbf{v} \cdot \nabla \mathbf{v} + \nabla(gh) = S(\mathbf{v}, h) \qquad (2.12b)$$

where h is the sea surface elevation, H is the mean depth of the ocean, $\mathbf{v}$ is the two-dimensional depth-average horizontal velocity, g is the acceleration due to gravity and S is the source term comprising Coriolis coefficient, bottom friction, eddy viscosity, etc.

Several existing codes that are based on finite different mesh discretization of the shallow water equations that implement Equation (2.12) include MOST (Titov and Gonzalez, 1997), TUNAMI (Imamura *et al*., 2006) and NAMI-DANCE (Imamura *et al*., 2006), COMCOT the Cornell Multi-Grid Coupled Tsunami Model (Wang, 2009), and the CEA code used at CENALT (Gailler *et al*., 2013; Hébert *et al*., 2012; Reymond *et al*., 2012). For the codes that are based on finite-volume discretization scheme include VOLNA (Dutykh *et al*., 2011) and GeoClaw (George and LeVeque, 2006), a research code based on Galerkin methods is TsunaFlash or TAM (Pranowo *et al*., 2008).

(b) Boussinesq equations

The classical Boussinesq equations can be used to model wave propagation with frequency dispersion. The classical Boussinesq equations are valid for wavelengths down to roughly a few water depths. The fully non-linear shallow-water generalized Serre equations are used in FUNWAVE (Kennedy *et al*., 2000; Shi *et al*., 2012). The majority of codes use finite difference schemes, for example, the Pedersen and Løvholt model which is designed for long distance propagation of dispersive tsunamis (Pedersen and Løvholt, 2008). By using this model, the 2011 Japan tsunami across the Pacific Ocean can be modelled on a standard desktop with a few hours of CPU time.

(c) Navier-Stokes equations

The most complete description of fluid wave behaviour uses the 3-D Navier-Stokes equations and can be applied for the complex fluid-structure interactions. The basic equations express conservation of mass and momentum

$$\frac{\partial \rho}{\partial t} + \nabla \cdot \ (\rho \boldsymbol{v}) \ = 0 \qquad (2.13a)$$

$$\frac{\partial \boldsymbol{v}}{\partial t} + \boldsymbol{v} \cdot \nabla \boldsymbol{v} = -\frac{\nabla p}{\rho} + \frac{\mu}{\rho} \ \nabla^2 \boldsymbol{v} \qquad (2.13b)$$

An example of the application of Navier Stokes equation solver in tsunami modelling is shown in Abadie *et al*. (2012) and Abadie *et al*. (2010) where multi-phase model (air-water-slide) is used to simulate land-slide induced tsunamis. Another example of the implementation of Navier-Stokes equations in a multi-material adaptive grid Eulerian code is the SAGE hydrocode, a commercial code that has been applied to study asteroid impact-generated tsunamis (Gisler *et al*., 2004) and landslide-generated tsunamis (Gisler *et al*., 2006).

2.5.2 Numerical methods

A number of physical description approaches for the deterministic mathematical modelling of tsunami wave behaviour are presented in Section 2.5.1. Traditionally, the method of finite difference has dominated the field of tsunami simulation (Titov and Gonzalez, 1997; Imamura *et al*., 2006) but recent developments of tsunami wave software have used more sophisticated numerical methods for solving hyperbolic or weakly parabolic equations. The Galerkin-type methods have also been adapted to ocean modelling applications for their robustness with respect to complex computational domains (Harig *et al*., 2008). The main idea of Galerkin-type discretization schemes is to solve the solution by replacing the continuous function space with a finite-dimensional (discrete) approximation to that space, usually a piecewise polynomial representation. The finite volume methods use the flux form of the equations with a basic assumption on the description of Eulerian perspective of a fluid dynamics and have also used in tsunami numerical modelling. Recent application of the finite volume for tsunami modelling includes the VOLNA code (Dutykh *et al.*, 2011) and GeoClaw (Dutykh *et al.*, 2011) that use adaptive mesh refinement. Furthermore, the modelling of violent impacts of a tsunami-like bore on structure can be conducted using traditional grid-based methods such as OpenFOAM. Many of these approaches need special techniques to treat the highly distorted free surface and violent flows in particular the energy dissipated in the broken wave and bore. As will be explained in Chapter 3, more recently meshless methods (with no computational grid) have emerged which can predict the non-linear and violent process occurring during tsunami impact. An example is the weakly compressible smoothed particle hydrodynamics (SPH) model which can simulate the hydrodynamic forces of tsunami impacting coastal structures (Crespo *et al.*, 2015; Cunningham *et al.*, 2014; Barreiro *et al.*, 2013; Rogers & Dalrymple, 2008).

A conventional strategy to perform tsunami simulation is the single compute core optimization as demonstrated by Bader *et al*. (2010) for solving shallow-water equation. This is particularly suited for memory-limited hardware architecture. However, many simulations are too large or required excessive computational runtimes to be run on a single core. Hence, hardware acceleration of simulation becomes necessary. Options include parallelization which can be achieved by message passing (MPI) or multi-threading shared memory (OpenMP) programming paradigm that have been implemented by GeoClaw (George and LeVeque, 2006), and the operational code TsunAWI that combine single-core performance optimization with multi-threading (Rakowsky *et al*., 2013) and the Boussinesq solver (Sitanggang and Lynett, 2005). For more computationally expensive simulations, a more powerful computing paradigm is to use general-purpose graphics processing units (GPGPUs) that can be accessed by special programming tools such as CUDA or OpenCL. GPGPUs enable simulations involving large size of data. Castro *et al*. (2013) described an approach, based on a high-order ADER (arbitrary high-order derivative) scheme based on the discontinuous Galerkin method, which can accurately simulate a tsunami and this code benefits moderately from GPGPU architecture with a maximum speed-up of approximately 30 over the original CPU code. Software accelerated with a GPU will be used in this thesis.

2.6 Concluding Remarks

This review has examined the basic properties of a tsunami wave and its simulation using the popular representation of a solitary wave. An understanding about the tsunami behaviour, especially its runup, inundation and impact forces on inland structures are the main elements to be able to perform a numerical modelling of tsunami wave. Field surveys after rare tsunami events revealed the poor performance of low-rise residential structures and this limited amount of data is now being used by researchers to validate their experimental and numerical modelling. These investigations are intended mostly to improve existing design guidelines of tsunami resistance coastal structures. Since experimental testing campaigns are restricted mainly by available budget, numerical modelling which is supported by the fast development in computation technology, offers a promising alternative to encourage the research in this field. These elements are investigated in this thesis. The next chapter will present a review and validation of the numerical method chosen for the fluid simulations, smoothed particle hydrodynamics (SPH). This will be followed by the choice of structural response modelling and validation in Chapter 4.

Chapter 3

Smoothed Particle Hydrodynamics (SPH) Methodology

3.1 Introduction

This chapter presents an overview of the numerical method smoothed particle hydrodynamics (SPH) used throughout this thesis. This includes the background and description of the basic theory of SPH with the integral interpolant, weighting functions, the discretised conservation of mass and momentum, moving of particles, time-step algorithm, and boundary conditions. The chapter highlights the previous work on SPH for modelling tsunami-like waves. The DualSPHysics v3.0 open-source software is used in this research to simulate tsunami-like waves and is briefly described. Finally, the validation of a broken bore using DualSPHysics is presented in preparation for later work in Chapter 5.

3.2 Basic theory of SPH

Smoothed Particle Hydrodynamics (SPH) is a purely Lagrangian mesh-free method conceived in the late seventies for modelling astrophysical phenomena and, later extended for application to problems of continuum solid and fluid mechanics phenomena (Monaghan, 2005). The basic idea of SPH is to use the collective motions of large number of particles to represent a flow with a Lagrangian description of motion rather than the Eulerian description. In this method, the moving fluid is represented by a set of irregularly spaced particles each with associated properties, such as mass, density, velocity, pressure, etc. For a given time step, the properties of each particle are estimated according to the corresponding properties of the neighbouring particles situated within an influence domain (or support). Since SPH does not require a computational mesh it is capable of dealing with problems with large deformation such as the broken bore of a tsunami wave and many other flows of great complexity that are difficult for mesh-based methods. In addition, Rogers and Dalrymple (2008) reported that SPH has been one of the most popular and successful methods for modelling free-surface hydrodynamics compared to other techniques such as Eulerian grid-based Large Eddy Simulation (LES) and Reynolds-Averaged Navier-Stokes (RANS).

This chapter will describe the basis of SPH where the fluid is treated as a set of particles in SPH and each particle has physical variables (such as velocity, position, density and pressure) computed as the interpolation of the values of the surrounding particles. The integral of the equation of motion of fluid dynamics is solved at each point in the Lagrangian formalism. A transition from a continuous medium (fluid) to a discrete medium (particles) is represented by a discretization process using a weighting *(kernel)* function. This function is used to evaluate particle interactions where it has a compact support within a region determined by a characteristic distance called the smoothing length, *h*. For simulating free-surface flow, there are now two variants of SPH: (i) weakly compressible SPH (WCSPH) which solves the conservation of mass and momentum equations with weak compressibility permitted; (ii) incompressible SPH (ISPH) which enforces zero divergence of the velocity field and solves the pressure Poisson equation (PPE), see Lind *et al*. (2015). While ISPH provides smoother pressure fields, it has not yet been developed for acceleration using GPUs within SPH software such as DualSPHysics. Moreover, WCSPH has been shown to provide acceptable pressure fields for engineering applications (Crespo *et al*., 2011) and is used herein. Following Barreiro *et al*. (2013), more details on SPH basic equations are described below.

3.2.1 SPH interpolant

The main feature of the SPH method is based on integral interpolants. The fundamental principle is to approximate any function $A(\boldsymbol{r})$ by:

$$\langle A(\boldsymbol{r})\rangle = \int_{\Omega} A(\boldsymbol{r})W(\boldsymbol{r}-\boldsymbol{r}', h)d\boldsymbol{r}' \tag{3.1}$$

where $\boldsymbol{r}$ is the position, W is the weighting function or *kernel*, h is the interaction distance or smoothing length which controls the domain of Ω and $\langle ... \rangle$ denotes an approximation. Note, that the conventional symbol for the smoothing length is h, which is not to be confused with water depth used by authors mentioned in Chapter 2. Wherever necessary the distinction between water depth and smoothing length is made clear in the rest of the thesis. Equation (3.1), in discrete notation, leads to an approximation of the function at a particle (interpolant point) a:

$$A_a = \sum_b m_b \frac{A_b}{\rho_b} W_{ab} \tag{3.2}$$

where the summation is performed over all the particles b within the region of compact support of the kernel function as illustrated by Figure 3.1. The mass and the density of particles b are denoted by the m_b and ρ_b respectively, while $W_{ab} = W(\boldsymbol{r}_a - \boldsymbol{r}_b, h)$ is the weighting function or *kernel* evaluated between particles a and b. Herein, the angle brackets, $\langle ... \rangle$, denoting the summation approximation are dropped for ease of writing. The derivative of the interpolants can be obtained by using:

$$\nabla A_a(\boldsymbol{r}) = \sum_b m_b \frac{A_b}{\rho_b} \nabla_a W_{ab} \tag{3.3}$$

where $\nabla_a W_{ab}$ denotes the gradient of W_{ab} with respect to particle a. Equation (3.3) can be used to estimate the gradient of arbitrarily scattered data. In practice, however, a range of different expressions are used to approximate the gradient of a variable. The choice generally depends on the quantity being conserved (Monaghan, 1992) but sometimes also on accuracy (Lind *et al*., 2012).

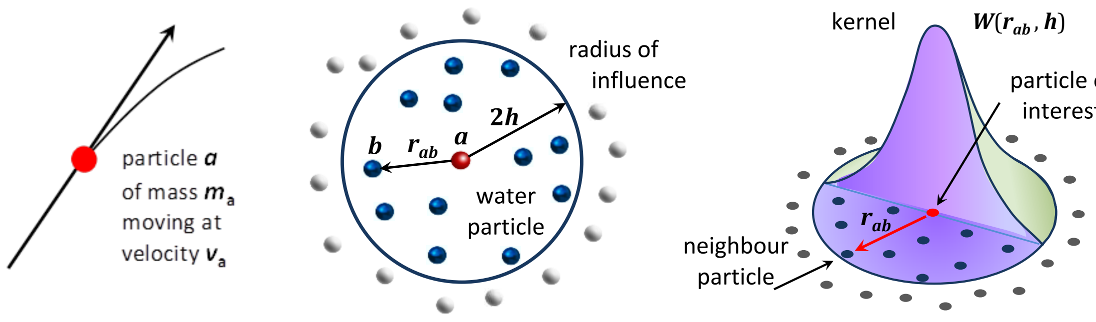

Figure 3.1 The diagram of SPH smoothing kernel

3.2.2 Weighting functions (Smoothing kernel)

The performance of the SPH model relies on the selection of the weighting functions that must satisfy the conditions such as positivity, compact support and normalization. The weighting functions depend on the smoothing length, h, and the non-dimensional distance between particles given by $q = r_{ab}/h$ where r_{ab} is the distance between particles a and ($r_{ab} = |\boldsymbol{r}_a - \boldsymbol{r}_b|$). The parameter h controls the size of the area surrounding particle a where the contribution of any other particles inside the area cannot be neglected.

Different weighting functions are available and based on different orders of polynomials used in the weighting functions, but the computational time also increases. In the DualSPHysics code used for simulations in this thesis, there are two options available for the weighting functions: the cubic-spline and quintic (Wendland);

$$\text{Cubic spline:} \quad W(q,h) = \alpha_D \begin{cases} 1 - \frac{3}{2}q^2 + \frac{3}{4}q^3 & 0 \le q \le 1 \\ \frac{1}{4}(2-q)^3 & 1 \le q \le 2 \\ 0 & q \ge 2 \end{cases} \tag{3.4}$$

where $q = r/h$, α_D is $10/(7\pi h^2)$ on 2D and $1/(\pi h^3)$ in 3D.

Traditionally, the cubic spline kernel is popular and widely used throughout the literature as a computationally cheap approximation to a Gaussian. The Wendland kernel is becoming increasingly popular since it is fifth order and computationally efficient.

Quintic-
(Wendland, 1995):

$$W(q,h) = \alpha_D \left(1 - \frac{q}{2}\right)^4 (2q+1) \qquad 0 \le q \le 2 \tag{3.5}$$

where $q = r/h$, α_D is $7/(4\pi h^2)$ on 2D and $21/(16\pi h^3)$ in 3D.

3.2.3 Momentum equation

In Lagrangian form, the momentum equation in continuous form is:

$$\frac{d\boldsymbol{v}}{dt} = -\frac{1}{\rho}\nabla P + \boldsymbol{g} + \boldsymbol{\Gamma} \tag{3.6}$$

where $\boldsymbol{v}$ is the velocity, t is time, P and ρ are pressure and density, respectively, $\boldsymbol{g}$ = (0, 0, -9.81) ms^{-2} is the gravitational acceleration and $\boldsymbol{\Gamma}$ is the dissipative terms. There are several ways to solve the dissipative terms; however, the most widely used due to its simplicity is the artificial viscosity proposed by Monaghan (1992) and is used herein.

There are numerous forms of an SPH gradient which are chosen according to the physics or numerical properties. With the classical formulation, the pressure gradient in SPH notation uses a symmetric form of the gradient to conserve momentum:

$$-\frac{1}{\rho}\nabla P = -\sum_b m_b \left(\frac{P_a}{\rho_a^2} + \frac{P_b}{\rho_b^2}\right) \nabla_a W_{ab} \tag{3.7}$$

where P_b and ρ_b are pressure and density of particle b. The artificial viscosity can be included in Equation (3.7) by adding the viscosity term $\boldsymbol{\Pi}_{ab}$ inside the bracket. Thus, the momentum conservation equation in SPH will be:

$$\frac{d\boldsymbol{v}_a}{dt} = -\sum_b m_b \left(\frac{P_a}{\rho_a^2} + \frac{P_b}{\rho_b^2} + \boldsymbol{\Pi}_{ab}\right) \nabla_a W_{ab} + \boldsymbol{g} \tag{3.8}$$

The artificial viscosity depends on the relative position and motion of the computed particles

$$\boldsymbol{\Pi}_{ab} = \begin{cases} \dfrac{-\alpha\overline{c_{ab}}\mu_{ab}}{\rho_{ab}} & \boldsymbol{v}_{ab}\cdot\boldsymbol{r}_{ab} < 0 \\ 0 & \boldsymbol{v}_{ab}\cdot\boldsymbol{r}_{ab} > 0 \end{cases} \tag{3.9}$$

where $\boldsymbol{v}_{ab} = \boldsymbol{v}_a - \boldsymbol{r}_b$, $\mu_{ab} = h\boldsymbol{v}_{ab}\cdot\boldsymbol{r}_{ab}/(\boldsymbol{r}_{ab}^2 + \eta^2)$, $c_{ab} = 0.5\ (c_a + c_b)$ is the mean value of the speed of sound, $\eta^2 = 0.01\ h^2$, and α is a free parameter that should be adjusted according to the configuration of the problem.

3.2.4 Continuity of equation

In WCSPH, the conservation of mass equation, or continuity, is solved in Lagrangian form as:

$$\frac{d\rho}{dt} = -\ \rho\nabla.\boldsymbol{v} \tag{3.10}$$

The changes in the fluid density are determined by solving the conservation of mass or continuity equation in SPH form:

$$\frac{d\rho_a}{dt} = \sum_b m_b\boldsymbol{v}_{ab}\cdot\nabla_a W_{ab} \tag{3.11}$$

The mass of each SPH particle is kept constant.

3.2.5 Equation of state

As the fluid is treated as weakly compressible in SPH, the fluid pressure can be determined by using an equation of state, which is faster than solving an equation such as Poisson's equation used in the incompressible approach. The following Tait's equation of state describes the relationship between pressure and density:

$$P = B\left[\left(\frac{\rho}{\rho_o}\right)^{\gamma} - 1\right] \tag{3.12}$$

The parameter B is a constant related to the fluid compressibility and can be determined from $B = c_0^2\rho_0/\gamma$, ρ_o = 1000 kg/m^3 is the reference density at the free surface, c_0 is the speed of sound given by $c_0 = c(\rho_0) = \sqrt{(\partial P/\partial\rho)|_{\rho_0}}$, and γ is the polytrophic constant ranging between 1 and 7. The polytrophic constant equal to 7 is used in DualSPHysics.

By choosing the speed of sound c_0 to be at least 10 times greater than the maximum particle velocity, $\boldsymbol{v}_{max}$, the local Mach number is $\boldsymbol{v}_{max}/c_0 < 0.1$. With the compressibility effects on the order of the Mach number squared, this equation of state permits small changes in density of less than 1% (Monaghan, 1992).

3.2.6 Moving the particles

The XSPH variant (Monaghan, 1989) is used to move particles;

$$\frac{d\boldsymbol{r}_a}{dt} = \boldsymbol{v}_a + \varepsilon \sum_b \frac{m_b}{\bar{\rho}_{ab}} \boldsymbol{v}_{ba} W_{ab} \tag{3.13}$$

where $\bar{\rho}_{ab} = \frac{1}{2}(\rho_a + \rho_b)$ and ε is a constant, whose the value ranges from zero to unity. The commonly used value for ε is 0.5.

The velocity of particle a is corrected using this method. The velocity correction is taking into account the velocity of particle a and the average velocity of all particles inside the compact support of kernel that interact with particle a. This correction allows particles to be more organized and prevents high velocity fluid particles penetrating through the boundaries.

3.2.7 Time-step algorithms

The physical magnitudes (velocity, density, position, and pressure) of particles change every time step due to the interaction of particles. To compute the new values of those physical quantities at the next time step of simulation, the time integration scheme must be at least second order to obtain accurate results. The equations of momentum (3.6), density (3.11), and particle position (3.13) are time-integrated in DualSPHysics using either the Verlet or Symplectic scheme.

3.2.7.1 Verlet scheme

The algorithm proposed by Verlet (1967) has two sets of equations. The first one which is used in most of the iterations is as follows:

$$\mathrm{v}_a^{n+1} = \mathrm{v}_a^{n-1} + 2\Delta t \frac{d\mathrm{v}_a^n}{dt} \tag{3.14a}$$

$$\rho_a^{n+1} = \rho_a^{n-1} + 2\Delta t \frac{d\rho_a^n}{dt} \tag{3.14b}$$

$$\mathrm{r}_a^{n+1} = \mathrm{r}_a^n + \Delta t \frac{d\mathrm{r}_a^n}{dt} + 0.5\Delta \mathrm{t}^2 \frac{d\mathrm{v}_a^n}{dt} \tag{3.14c}$$

The second equation of Verlet algorithm is used every certain number of steps, usually once after 50 steps to recouple the equations

$$\mathrm{v}_a^{n+1} = \mathrm{v}_a^n + \Delta t \frac{d\mathrm{v}_a^n}{dt} \tag{3.15a}$$

$$\rho_a^{n+1} = \rho_a^n + \Delta t \frac{d\rho_a^n}{dt} \tag{3.15b}$$

$$\mathrm{r}_a^{n+1} = \mathrm{r}_a^n + \Delta t \frac{d\mathrm{r}_a^n}{dt} + 0.5\Delta \mathrm{t}^2 \frac{d\mathrm{v}_a^n}{dt} \tag{3.15c}$$

This was not the preferred scheme here.

3.2.7.2 Symplectic scheme

Symplectic time integration algorithms are time reversible in the absence of viscous effects (Leimkuhler *et al.*, 1996). The symplectic method maintains geometric features that include energy time-reversal symmetry, causing improved resolution of long term solution behaviour. The form of an explicit Symplectic scheme is a first predictor step

$$\rho_a^{n+\frac{1}{2}} = \rho_a^n + \frac{\Delta t}{2} \frac{\mathrm{d}\rho_a^n}{\mathrm{d}t} \tag{3.16a}$$

$$\boldsymbol{r}_a^{n+\frac{1}{2}} = \boldsymbol{r}_a^n + \frac{\Delta t}{2} \frac{\mathrm{d}\boldsymbol{r}_a^n}{\mathrm{d}t} \tag{3.16b}$$

In a second time step the velocity is given by $\left(\mathrm{d}(\boldsymbol{v}_\mathrm{a})^{\mathrm{n}+\frac{1}{2}}\right)/\mathrm{dt}$.

The position of the particles at the end of each time step is determined by:

$$(\boldsymbol{v}_a)^{n+1} = (\boldsymbol{v}_a)^{n+\frac{1}{2}} + \frac{\Delta t}{2}\frac{d(\boldsymbol{v}_a)^{n+1}}{dt} \tag{3.17a}$$

$$\boldsymbol{r}_a^{n+1} = \boldsymbol{r}_a^{n+\frac{1}{2}} + \frac{\Delta t}{2}\boldsymbol{v}_a^{n+1} \tag{3.17b}$$

At the end of the time step $d\rho_a^{n+\frac{1}{2}}/dt$ is determined using the updated values $\boldsymbol{v}_a^{n+\frac{1}{2}}$ and $\boldsymbol{r}_a^{n+\frac{1}{2}}$ (Monaghan, 2005).

3.2.8 Variable time-step

A variable time step can be used throughout an SPH simulation to save computational time. The time step relies on the flow properties. For example, the time step decreases when the fluid interacts with fixed boundaries because the forces increase. The time step depends on the force per unit mass and the Courant condition. A variable time step Δt is computed according to (Monaghan and Kos, 1999):

$$\Delta t = C \cdot min\left(\Delta t_f, \Delta t_{CV}\right) \tag{3.18a}$$

$$\Delta t_f = \underset{a}{min}\left(\sqrt{h/|f_a|}\right) \tag{3.18b}$$

$$\Delta t_{CV} = \underset{a}{min}\, \frac{h}{c_s + \underset{b}{max}\left|\frac{h\boldsymbol{v}_{ab}\cdot\boldsymbol{r}_{ab}}{(\boldsymbol{r}_{ab}^2 + \eta^2)}\right|} \tag{3.18c}$$

The Δt_f is based on the force per unit mass $|f_a|$, while Δt_{CV} depends on the Courant condition and the viscosity of the system. C is a constant range between 0.1 and 0.3.

3.2.9 Boundary conditions

In DualSPHysics, the implemented boundary conditions include the Dynamic Boundary Conditions (DBCs) for solid walls and the Periodic Boundary Conditions (PBCs) for open boundaries. The boundary particles (BPs) and the fluid particles (FPs) in the DBCs satisfy the same equations but are not allowed to move in any direction except when externally imposed such as a flap or a piston in a wave maker or any other kind of moving objects including gates or elevators. In the DBCs, the FPs are free to move and interact with each other such that the density of BPs increases when a FP approaches it within a distance smaller than $2h$, leading to a pressure increase following the equation of state. This condition changes the force exerted on the FP based on pressure term in the momentum equation. In addition, the PBCs allows the particles close to the open lateral boundary to interact with the particles on the other side of domain since the particles' influence area extends beyond the lateral boundary. More details on the boundaries in DualSPHysics can be found in Crespo *et al*. (2007).

3.3 Previous use of SPH for modelling tsunami-like waves

3.3.1 SPH numerical modelling in 3-D

Nistor *et al*. (2010) conducted research by using SPHysics, a FORTRAN open-source code which is based on Smooth Particle Hydrodynamics (SPH), to model an experiment investigating hydraulic bore impacts on structural components. The aim of the work of Nistor *et al*. (2010) is to propose improved design guidelines which would address tsunami loading for design of structures constructed in tsunami-prone areas. Parameters they investigated include the effect of: (1) the repulsive boundary condition; (2) laminar viscosity with Sub-Particle Scale (SPS) turbulence formulation proposed by Dalrymple and Rogers (2006) to describe the viscous terms of the momentum equation; (3) quadratic smoothing kernel introduced by Johnson *et al*. (1996); (4) the symplectic algorithm for advancing time; and (5) the non-conservative formulation proposed by Parshikov (1999).

The simulation of wave impact on a circular column involved a computational domain consisting of 319,000 particles. The total time to complete a simulation of duration of 4.00 seconds was about 172 hours (using a 2 GHz Intel Xeon E5405 system with single processor and 16 GB RAM). The snapshots of the initial condition with upstream impoundment depth of 0.75 m, fluid particles flowing around a circular structure and estimated pressure over time are shown in Figure 3.2. The numerical model is shown to reproduce reasonably the results of the experimental work and improvement for the current SPH model to integrate the computed pressure distributions.

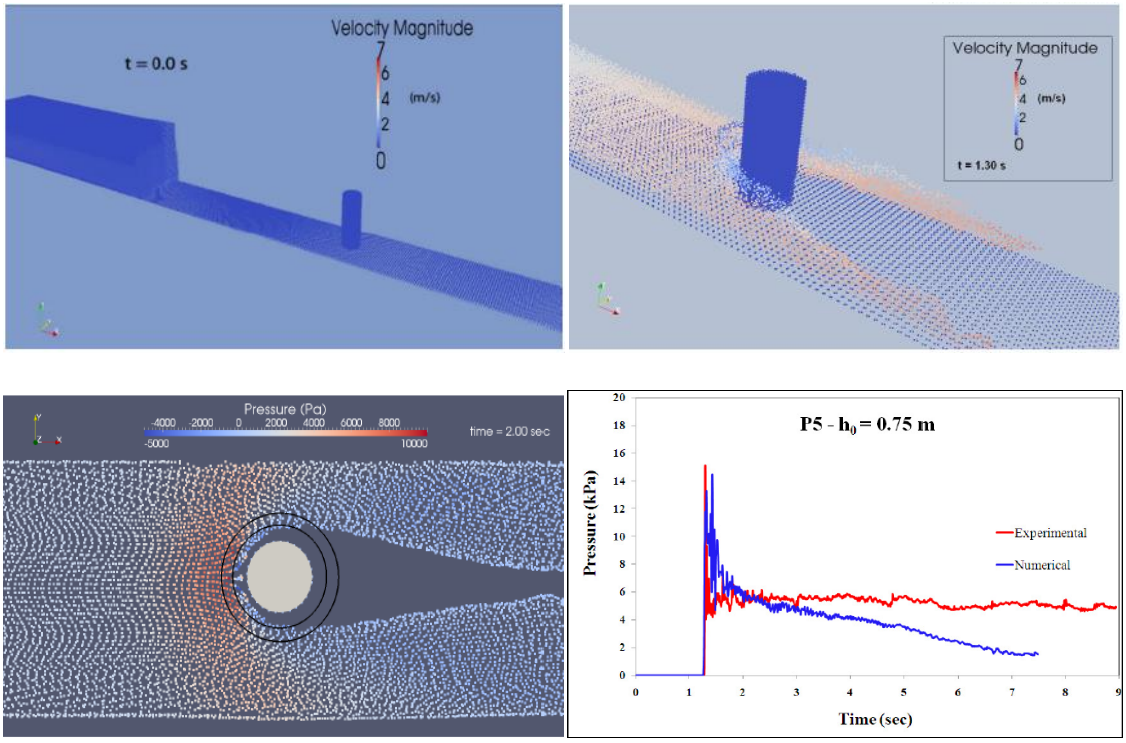

Figure 3.2 Results of numerical modelling using SPHysics by Nistor *et al*. (2010)

St-Germain *et al*. (2014) used single-phase 3-D weakly compressible smoothed particle hydrodynamics (WCSPH) to investigate the hydrodynamic forces induced by rapidly advancing tsunami-like bore impact on a square cross section free-standing column. The numerical time histories of wave surface elevation and force acting on the column were compared with large-scale physical experiment results. The experiments were conducted on the basis of analogies between tsunami bore and dambreak waves.

The work of St-Germain *et al*. (2014) used SPHysics (Gómez-Gesteira *et al*., 2010) to perform all numerical simulations in their study. Also, in all simulations, a dry bed condition was assumed since, based on work by Stansby *et al*. (1998) and Leal *et al*. (2006), it was found that the difference in downstream water layer thickness resulted in large differences between the propagation characteristics of numerical and experimental bore, and as a consequence resulted in considerable dissimilarities in the resulting forces exerted on the column. The sensitivity analysis regarding the inter-particle spacing was conducted by St-Germain *et al*. (2014). The implementation of high frequency (1000 Hz) related with the numerical output was highlighted because with high frequency the sudden rise in resulting force could be captured properly over short intervals covering the initial wave impact condition. However, the high frequency only applied for the short duration impact and the rest of the simulations were obtained at frequency of 100 Hz due to limited hard disk memory.

In their conclusion, St-Germain *et al*. (2014) were concerned about the presence of a thin water film that could become the source of discrepancies between the numerical and experimental wave impulsive impact force on structure. The elaboration of new design guidance for tsunami resistance structure and the development of multi-phase SPH model will become their focus in future research since single phase SPH unable to predict the entrained air bubble in the flow field that can significantly inhibit impulsive pressure at the initial impact.

Wei *et al*. (2015) numerically modelled dynamic impact of tsunami bore on bridge piers. The modelling was motivated by the observations of bridge damage during recent tsunami events. During the 2011 Japan tsunami alone there were more than 300 bridges washed away (Kawashima et al., 2011). The GPUSPH code was utilized for exploring hydrodynamic force caused by bridge pier blockage and the bore impact on structures. The GPUSPH code is a weakly compressible SPH-based method that uses the latest GPU parallel computing techniques. The results of numerical modelling by Wei *et al*. (2015) are validated against well-conducted physical experiments of bore impingement on vertical columns by Arnason *et al*. (2009), where the bore generation was based on the dambreak analogy. Wei *et al*. (2015) used a dambreak bore to simulate a tsunami bore due to their similarity based on Bryant (2014) where the tsunami undergoes shoaling and may eventually break into a series of bores once it approaches shallow water. The GPUSPH simulation of dambreak bore impacted vertical structures with different shapes: circular, square and diamond (rotated square) as shown by Figure 3.3.

Wei *et al*.'s (2015) use of the SPH method to simulate the experiment by Arnason *et al*. (2009) shows the advantage of the Lagrangian nature of SPH when applied for simulating free-surface flows since there is no need to deal with the free surface especially when the surface tension is not important. Another reason was that the SPH method is able to determine the dynamic force on structure directly. Wei *et al*.

(2015) stated that in an SPH model, the external force exerted by neighbouring particles on a particle is part of the numerical solution. Hence, the hydrodynamic force on the piers is determined from the summation of the external forces exerted by fluid particles on those boundary particles. The simulations by Wei *et al*. (2015) were quite similar with the SPH simulation done by St-Germain *et al*. (2014). However, Wei *et al*. (2015) were using higher resolution (particle size = 0.005 m) so that the accuracy and quantitative free surface solution are better than the results of St-Germain *et al*. (2014).

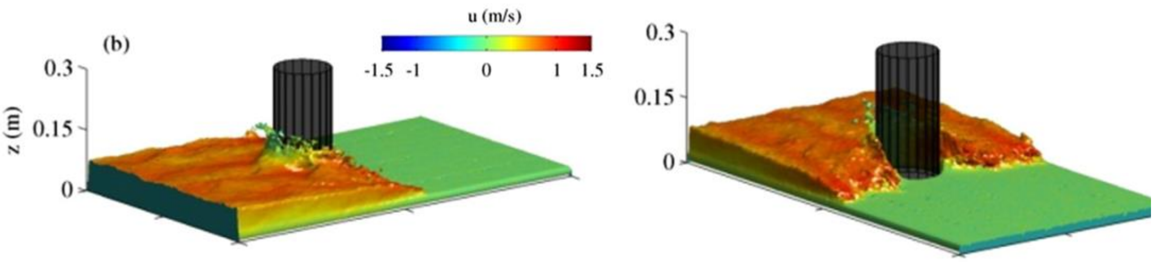

(a) Bore impact on cylindrical column

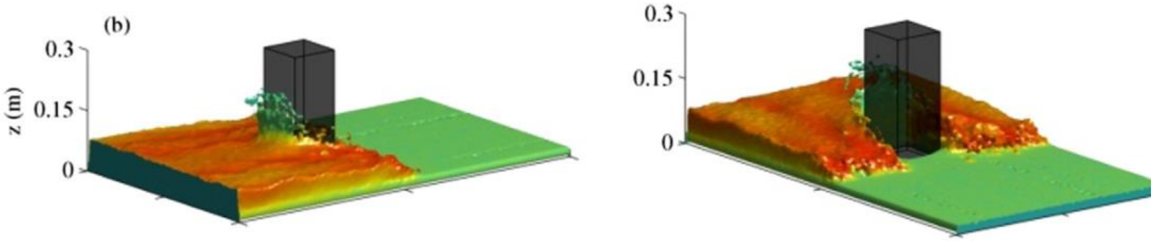

(b) Bore impact on rectangular column

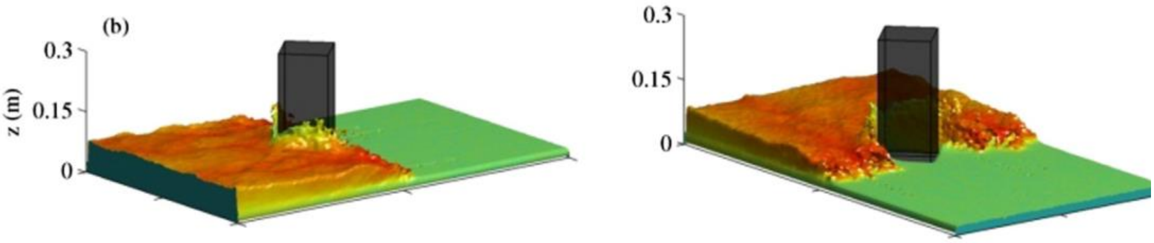

(c) Bore impact on diamond column

Figure 3.3 GPUSPH simulations of bore impacts on structures Wei *et al*. (2015)

Wei *et al*. (2015) showed that the highest numerical hydrodynamic total force predicted was for diamond-shape piers followed by square and circular shapes. The diamond-shape generated the highest total force because of it has largest area facing the incoming bore and also because the blockage effect due to shortest distance remain between the structure and boundary side wall. Furthermore, in Wei *et al*. (2015) the agreement between the measurement and the simulation is quantified using the coefficient of variation of the root-mean-square error divided by the mean of the measured force. It was found that the coefficient of variation values for the circular, square and diamond cases are 12%, 11% and 6%, respectively. These mean that the overall agreement obtained by the diamond-shape bridge pier is better than two other cases.

3.3.2 SPH numerical modelling in 2-D

Another recent SPH-based numerical modelling using SPHysics was conducted by El-Solh (2012) to study the wave-induced forces and loading on near shore structure (sloping seawall) and inland vertical structure (vertical wall). Three numerical models were conducted in 2-D and the results were compared with the corresponding physical data. The tests performed involved simulation of three different experimental cases: (i) experiments by Ramsden (1993) investigating solitary wave impact on an instrumented wall in a wave tank; (ii) an experimental investigation by Esteban *et al.* (2009) studying the effect of various types of solitary waves on the failure mechanism of armoured caisson; (iii) work by Hsiao and Lin (2010) involving a series of laboratory experiment to investigate the effect of wave impacting and overtopping an impermeable sea wall.

The sensitivity analysis of parameters for SPHysics was conducted prior to the modelling process of the three experimental works as mentioned above. This sensitivity analysis aimed to understand better the effects of several important parameters such as smoothing length, speed of sound, particle spacing, etc., on modelling results. Thus, each model was created by using different chosen values of parameters (mainly the particle spacing) that best fit the corresponding experimental data. The accomplishment of wave simulations were based on careful investigation on three stages of wave evolutions: wave generation, propagation and breaking.

El-Solh (2012) argued that the formation of solitary waves is precisely reproduced and the impacting bore profiles along with resulting pressures were accurately predicted, based on the results of numerical 2-D simulations. Figure 3.4 shows the comparison of the incident wave profile between the numerical model and the different experimental data where the maximum wave height is comparable; however, the pressure prediction of the numerical model underestimates the experimental results by more than a factor of two, as can be seen in Figure 3.5.

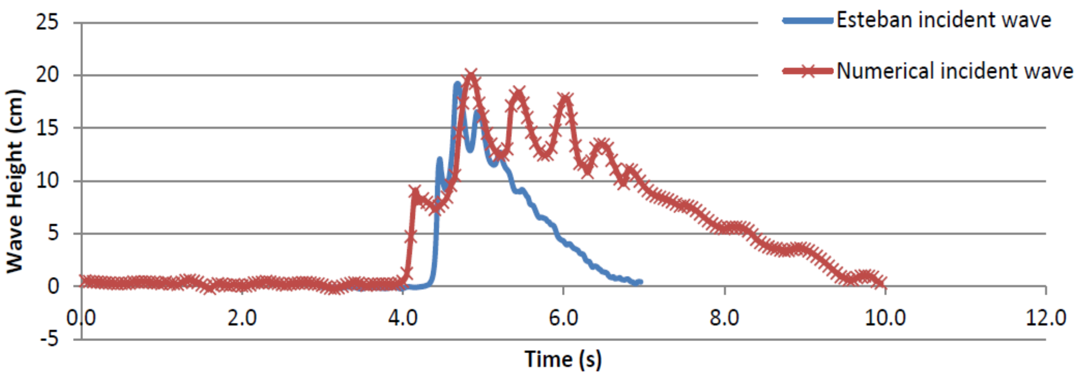

Figure 3.4 Comparison of the incident wave profile in El-Solh (2012)

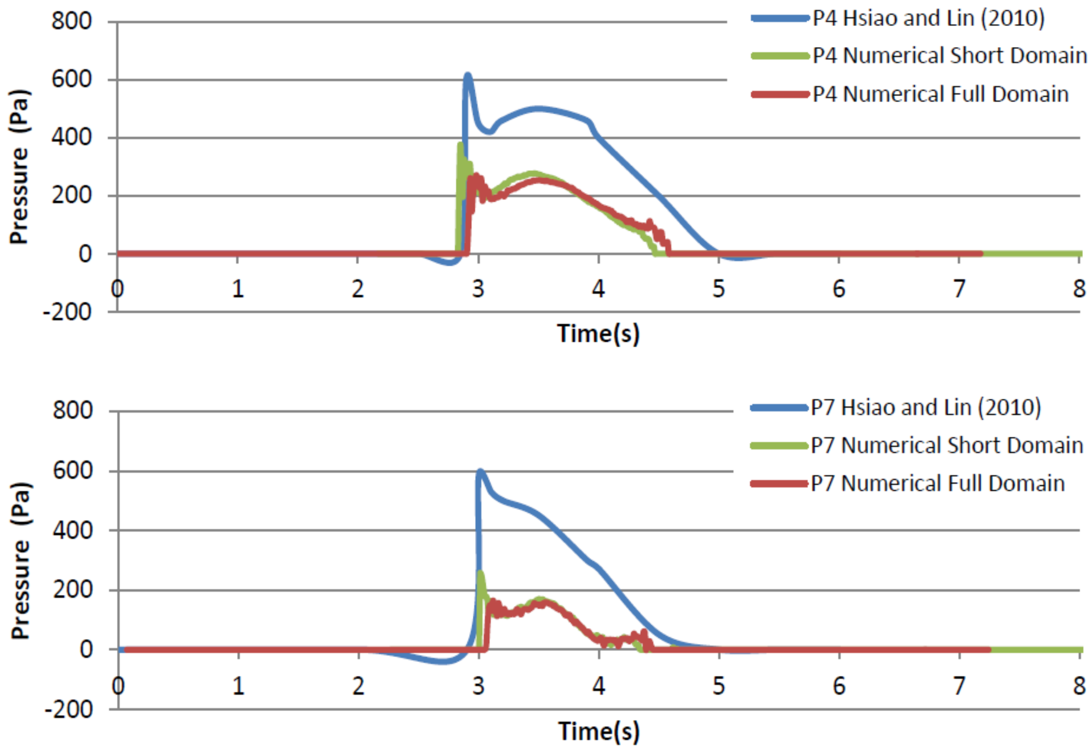

Figure 3.5 Comparison of the pressure time history in El-Solh (2012)

The work by El-Solh (2012) was based on a 2-D model simulation and only used a single central processing unit (CPU) to execute it. The total computational time that was needed to perform a single low resolution model involving 40,397 particles is

1.92 days, while to finish the same model with a higher resolution involving nearly 4.6 times more particles needed 15.2 days. This demonstrates that some form of hardware acceleration is required in order to improve the future modelling performance by extending the 2-D model to 3-D which requires a greater number of particles.

3.4 DualSPHysics

A short period of physical time for SPH applications requires a large computational time when running on a single central processing unit (CPU) due to the large number of interactions for each particle at each time step. For this reason, computational acceleration is necessary to perform faster computations for large domains involving millions of particles. Besides using high-performance computing (HPC) with thousands of CPU cores, another hardware acceleration that can be employed is using Graphics Processing Units (GPUs), a novel computing architecture that is highly efficient for treating large data flows as explained in Chapter 2.

Since GPU multi-processor technology has increased much faster than that of the CPU, as well as low-cost benefit and ease-of-maintenance of GPUs, GPUs now represent a viable alternative to accelerate simulations including SPH models. Harada *et al*. (2007) was one of the first to simulate successfully SPH acceleration by using GPUs. While both CPU and GPU can be used to perform SPH computational modelling, software named DualSPHysics that can be run on either the CPU or GPU architecture has been developed by the SPHysics group in a collaborative effort amongst researchers at the University of Vigo (Spain) and the University of Manchester (UK). DualSPHysics is part of long-term aim that previously follows the development of the SPHysics code which allows a fine description of the flow in the near shore areas but cannot be efficiently applied over large domains. By using a GPU in DualSPHysics validated and benchmarked software, the speed-up can be up to two orders of magnitude. More details about DualSPHysics program can be found in Crespo *et al*. (2011), Crespo *et al.* (2014), Gomez-Gesteira *et al*. (2012a), Gomez-Gesteira *et al*. (2012b) and Barreiro *et al*. (2013). DualSPHysics is a free open-source SPH code released online (http://www.dual.sphysics.org). It is used throughout this thesis.

3.4.1 Pre-processing

The DualSPHysics version 3.0 software package will be used in this project to model the tsunami and storm waves along with the structures surrounding coastal areas. Some steps should be completed in the pre-processing stage which can be accomplished by following the GenCase XML Guide that provides step-by-step procedures in order to create a model. This stage is divided into two main parts. The first part consists of several steps to define the initial geometry and configuration, while the second part deals with information that is needed for the execution process. In the XML file structure, both parts are named “casedef” and “execution”. An example XML file for DualSPHysics used to run cases in Section 3.5 is included in Appendix A.

The “casedef” XML input file consists of some important SPH constants, such as gravity, maximum water height, speed of sound. The fluid orientation in 2-D or 3-D and the system’s geometry are also determined in the “casedef”. Within the system’s geometry, the distance of particles and domain size can be defined. A domain reflects a space restricted by two points of “pointmin” and “pointmax” where the models are located. Other important features contained in the “casedef” XML input file are “initial”, “floating” and “motion”. The “initial” is a condition of particles before moving, while the “floating” is a description of a floating object which later can be used to model debris carried by waves and “motion” is a description of boundary’s movement, for example, the motion of a paddle to generate waves. The coastal topography, wave properties and coastal structures are created in the “casedef” XML file. A coastal structure such as a residential building with a complex geometry cannot only be drawn by applying specific commands for drawing in “casedef” XML input file, but can also be imported into the program. The formats of a file that can be read by DualSPHysics are VTK, PLY or STL.

The “execution” is defined in the XML file, but it can be also defined or changed by using “execution parameters”. This is the processing stage in DualSPHysics. More execution parameters that can be imposed are time stepping algorithm, choice of kernel function, value of artificial viscosity, the maximum time of simulation and time intervals to save the output data, etc. In this process, it is important to specify whether the simulation will be run in CPU or GPU mode, the format of the output files, and some other information about particles.

3.4.2 Post-processing

The post-processing stage of the modelling process comprises visualisation of boundaries and all particles from the output data. In this process, numerical measurement can be performed by using “measure tool” that computes different physical quantities using SPH summations (Equation (3.2)) at a set of given locations. The numerical values gained from this process can be compared to the experimental data. Moreover, the simulation of water flows can be visualized by using a surface created using the ‘marching cubes’ algorithm instead of particles. The following section provides a demonstration of the ability of DualSPHysics in modelling a dam break case which also used as a convergence study to identify the appropriate particle size for models presented later.

3.4.3 Application of DualSPHysics

Barreiro *et al*. (2013) demonstrated the application of SPH for coastal engineering problems with DualSPHysics. As a validation of the SPH method, Barreiro *et al*. (2013) tested the capability of DualSPHysics to simulate wave-structure interaction following experimental work by Yeh and Petroff at the University of Washington (Arnason, 2005) and the results showed that the DualSPHysics can reproduce the dynamic response of a structure by comparing the numerical and experimental force exerted on structure. Another comparison between the numerical model and experimental for wave propagation was also conducted by using the CIEMito flume of Universitat Politècnica de Catalunya (UPC). The comparison results show agreement between experimental data and numerical water simulation modelled with DualSPHysics.

Following the validations, Barreiro *et al*. (2013) applied the DualSPHysics to real engineering problems by creating a model involving coastal structures at full scale and examined the complexity of the flow around urban furniture such as balustrade of the seawalk and a lamp post, examining the wave force exerted on those structures. A detailed shape of full-scale structures dimension in the model was possible to be created in DualSPHysics by employed pre-processing tool for SPH models with complex geometries (Domínguez *et al*., 2011). This complex detail of structure generated a large number of particles (4 million) in the 3-D simulation, however since DualSPHysics is created to be able to manage huge number of data, the simulation for 9 sec of physical time only needed 9 hours to be completed using GPU card GTX480, while using CPU device the simulation would take days.

For the wave force exerted on the structure, Barreiro *et al*. (2013) observed the occurrence of a negative force when the wave impacted the balustrade. The negative forces that occurred after the wave interacts with balustrade were identified due to splash that projects some part of water in the opposite direction to that of the advance of the wave. With the force on structures, Barreiro *et al*. (2013) showed the role of the artificial viscosity that defined the magnitude of force where both parameters related to the momentum equation. Barreiro *et al*. (2013) concluded that the DualSPHysics software is efficient since it enables the simulations of millions of particle at a reasonable computational time and this can help to reduce the cost of research in particular areas and also help coastal engineers to create reliable measures to reduce coastal vulnerability and flood risk.

3.5 Validation of DualSPHysics: Dam-break case (Kleefsman, 2005)

A schematic simple case for validation purposes is needed to be performed before moving onto the more complex case for tsunami-like wave modelling. A very popular case for an SPH model validation is the dambreak case because the set up is relatively easy with no special in- or outflow conditions needed. The Kleefman's dambreak case (Kleefsman *et al*., 2005) that has been suggested by The SPH European Research Interest Community (SPHERIC) for validation purpose (Lee *et al*., 2010) was reproduced here.

The Kleefman's experiment is a simplified model of green water flow on the deck of the ship. As illustrated in Figure 3.6, a tank with dimension of 3.22x1x1 m is used with an open roof. At the right side of the tank a door restrained a 0.55m high column of water ready to flow when the gate is opened. A box is placed at the left side of the tank representing a scale model of a container on the deck of the ship. The measurements recorded during the experiment included water heights, pressures and forces. Four vertical probes (H_1-H_4) have been used: one probe placed in the reservoir and the other three probes placed in the tank. The box was also equipped by eight pressure sensors (P_1-P_8): four sensors mounted on the front and another four sensors mounted on the top of the box. The initial condition in the experiment consists of the water at the right-hand part of the domain at rest. Once the door is opened, the water starts to flow due to gravity into the empty region where the box was placed and followed by water impact on the surface of the box. The removal of the gate is considered fast enough to be neglected in the numerical simulations. Detail dimensions and layout of the experiment are depicted in Figure 3.6 and Figure 3.7. The water surface elevations and the wave impact pressures were measured by the vertical and pressure probes, respectively.

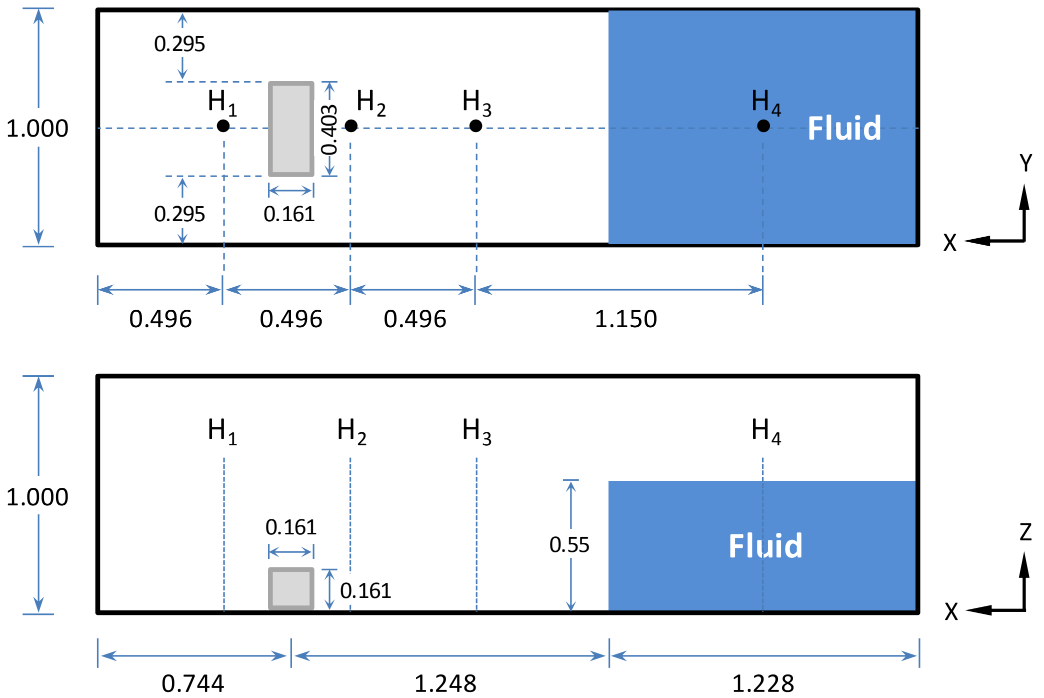

Figure 3.6 General description of the system. H_1, H_2, H_3, H_4 are water depth probes.

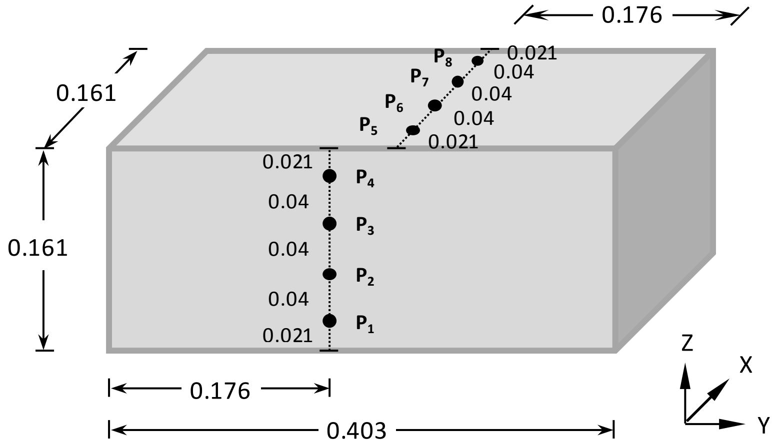

Figure 3.7 General description of the box. $P_1 - P_8$ are pressure probes mounted on the box.

The Kleefman's experiment was re-modelled by modifying the CaseDambreak that is available in DualSPHysics package that can be downloaded online from http://dual.sphysics.org. Different numbers of particles were involved in the numerical modelling process to identify the optimum particle size that can give close prediction to the experimental results. The quantitative comparisons between numerical model and experimental results were made with measured water height histories at probes and pressure time histories at sensors. The aim of this comparison is to investigate the influence of the resolution of particles on the accuracy of model's prediction.

3.5.1 DualSPHysics parameters

Some important input values for this dam break case is given in Table 3.1. These key values are mainly the constants and the execution parameters. In Table 3.1, the particle diameter is in metres. The lattice is staggered grid to locate particles. The CFL number is a coefficient in the Courant condition which is needed to compute the speed of sound. The "Coefficient value" in Table 3.1 is a coefficient needed to compute the smoothing length. The other parameters such as step algorithm, kernel type, viscosity and gamma are explained in Section 3.2 of this chapter. The Shepard step is used to determine the frequency at which the density filter is applied. Rho is the reference density of water in kg/m^3.

Table 3.1 DualSPHysics constants and input parameters

Parameter		Value	Parameter		Value
Particle diameter	:	0.008 - 0.016	Step Algorithm	:	2 (Symplectic)
Lattice number	:	1	Kernel type	:	2 (Wendland)
CFL number	:	0.2	Viscosity	:	0.1
Coef. of sound	:	10	Shepard steps	:	30
Coefficient value	:	0.75	Gamma value	:	7
Eps value	:	0.25	Rho	:	1000

3.5.2 The results of numerical dam-break modelling

A series of DualSPHysics dambreak numerical models were performed as part of a convergence study to find out the optimal model resolution that can give closest agreement to the experiment. The model resolutions were based on three different particle sizes denoted with $L/20$, $L/15$ and $L/10$, where L is the smallest length dimension of impacted structure, which was a box in this case, with smallest dimension 0.161 m for the width and height. Hence, the particle sizes used in the modelling were 0.008m, 0.011m and 0.016m for $L/20$, $L/15$ and $L/10$, respectively. The models we run using different types of GPU depending on availability; all have 14 multi-processors (448 cores) and 1.15 GHz clock rate. The only difference between the GPU is the global memory available: 5375 GB for Tesla M2070 and 2687 GB for both Tesla S2050 and M2050. The use of those GPU devices was arranged by the University of Manchester IT Service based on available devices for running the simulations. The details of the numerical model with different resolutions are given in Table 3.2. It can be seen that the finer the resolution the longer the simulation run-time required and this is due to the time needed for the larger number of particles within the domain. All simulations were run for 4 sec physical time.

Table 3.2 Details of models' resolution

Resolution of model	Diameter of particle	Number of particles	Simulation run time (sec)	GPU type
L/20	0.008 m	1,701,016	6,001	Tesla M2070
L/15	0.011 m	927,479	2,526	Tesla S2050
L/10	0.016 m	266,146	428	Tesla M2050

The pressures on the surface of the box measured by numerical probes are shown in Figure 3.8 and compared with experimental pressure data. Figure 3.8(a) and (b) show the pressure obtained by upstream probes P_1 and P_3, respectively.

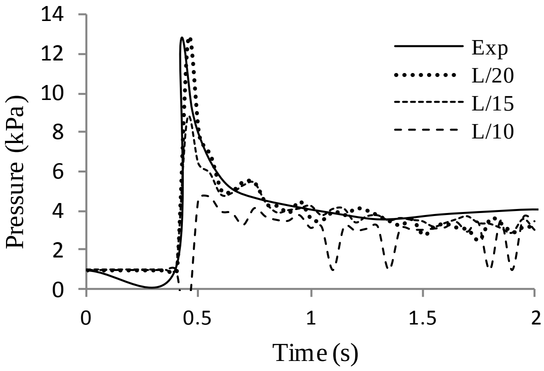

(a) Pressure at probe P_1

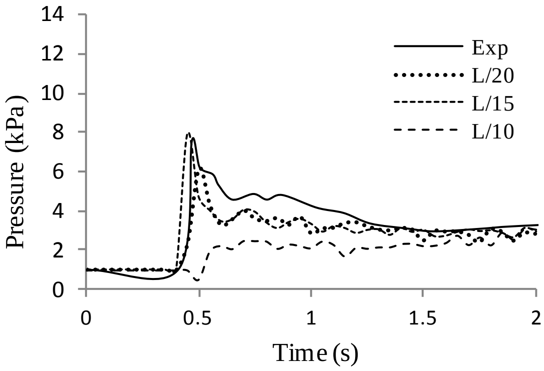

(b) Pressure at probe P_3

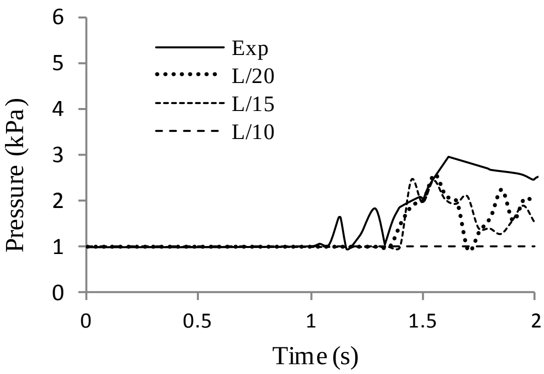

(c) Pressure at probe P_5

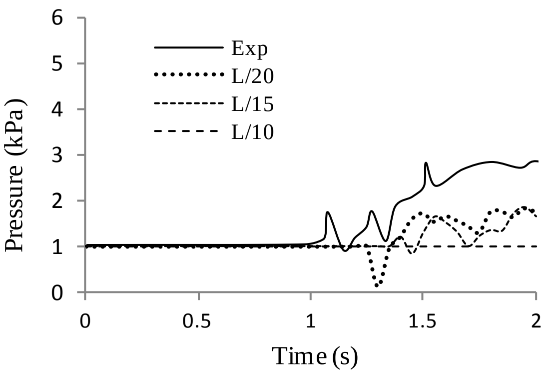

(d) Pressure at probe P_7

Figure 3.8 Dambreak wave pressures on the surface of the box

The first wave impacts on obstacle were marked by sharply increase pressure value. Figure 3.8 (a) illustrates that the peak impact times for all numerical model with resolution $L/20$, $L/15$ and $L/10$ generally do not differ much from the measured data, however, the closest numerical peak pressure to the measured data is given by the $L/20$ resolution model. A similar trend can be seen in Figure 3.8(b) where the $L/20$ resolution model gives closer prediction to the measured data compared with $L/15$ and $L/10$ resolution models. Figure 3.9 shows snapshots of the water surface.

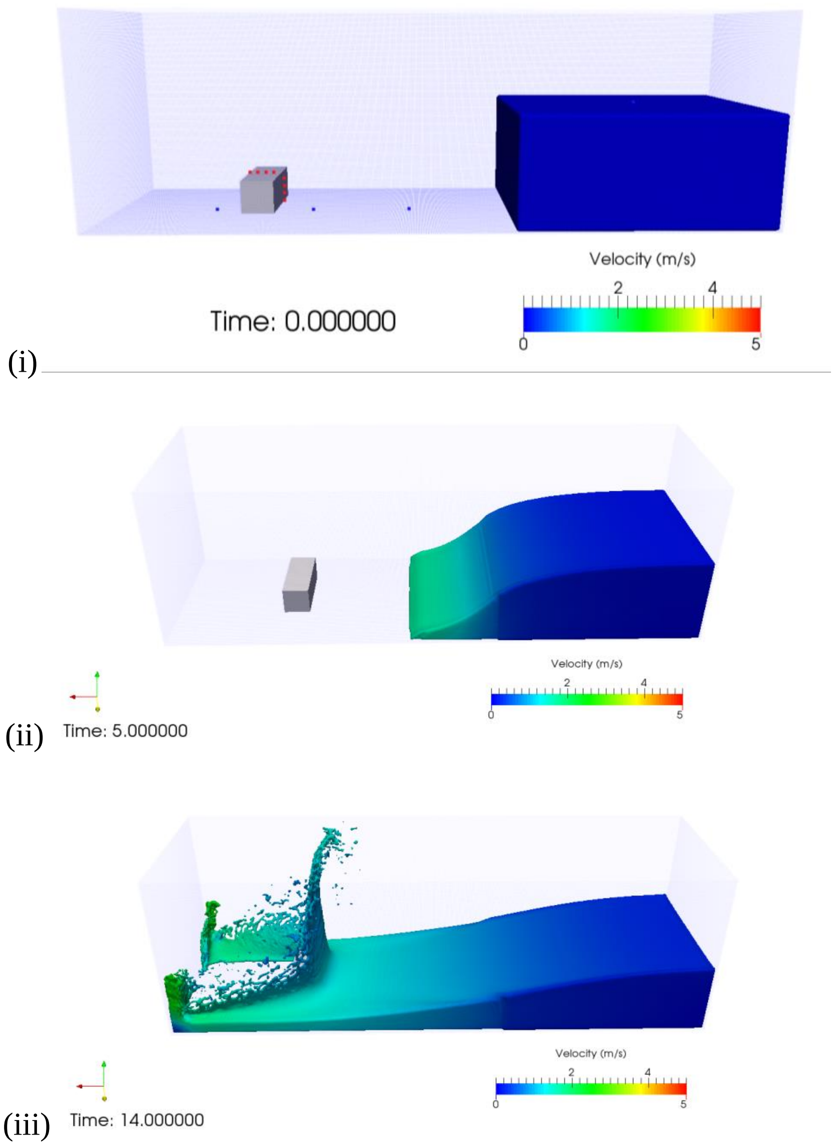

Figure 3.9 The snapshots of dambreak simulation: (i) at rest, (ii) before the water impacting the box, (iii) after the water impacting the box and the wall.

The impact pressures obtained by probes on the top surface of the box are depicted in Figure 3.8(c) and (d), where both figures show that the numerical model struggles to predict the experimental pressure and the first impact occurrence time. This was caused by overtopping wave behaviour due to different numerical model resolutions. For example, the pressure probes P_5 and P_7 did not measure any pressure for the case with $L/10$ resolution within the first 2 sec and on the plots these are shown by a zero value with a straight dotted lines, however, the other two models with $L/20$ and $L/15$ resolution provide pressure values even though they are different compared with experimental data. In the experiment, probes P_4, P_5 and P_7 were not completely covered by fluid and therefore their values are questionable. In conclusion, a particle size (d_p) or resolution of $L/20$ is required to capture the impact pressure on the obstacle due to a broken bore. This information is used to guide the choice of particle size for later simulations presented in Chapter 5

3.6 Concluding Remarks

The SPH method has been widely implemented to solve problems of computational fluid dynamics. The method has been proven to be partially suitable to reproduce the free-surface phenomena such as breaking waves, fluid-structure interaction and violent wave motion such as tsunami wave impact and many other flows of great complexity that are difficult for mesh-based methods. With the rapid development in technology, the SPH method now can be run on CPUs and/or GPUs. The SPH-based software SPHysics and DualSPHysics have been used by researchers to re-model experimental tests and both software packages are capable of capturing hydrodynamic phenomena and predict the pressure exerted on a square structure accurately especially in the modelling regarding the wave-structure interactions. In this chapter, the results of a broken bore dambreak convergence study using DualSPHysics gives close agreement with experiment data. The parameter values used in this validation will be used in the rest of the SPH numerical modelling in this research. The next chapter presents the modelling approach for simulating the structural response.

Chapter 4

Dynamic Analysis using the Finite Element Method (FEM)

4.1 Introduction

This chapter presents the use of the commercial finite element software ABAQUS to model structures under transient loading similar to that experienced during tsunamis. As a means of validating the ABAQUS models, a number of existing experimental studies will be simulated and the results compared. Details of the modelling process and associated results are given in the following sections.

4.2 Finite element modelling of structures under transient loading

The finite element method (FEM) can be used to predict the response of structures with high accuracy. FEM is widely applied to modelling structures and materials (Mishnaevsky and Schmauder, 2001) with many loading variations including transient loads (Boh *et al*., 2004). The applications of finite element methods for modelling structures consider several important aspects such as the geometric complexity of structure (Talaslidis *et al*., 2004) and also the technique to apply the loads (Børvik *et al*., 2009). In this research, the transient loading is considered since it is analogous to the impulsive tsunami-like wave impact loading characteristics. In addition to impulsive waves, other common sources of extreme transient loads on structures may be derived from blast loading, hurricane-force wind loads and seismic loads (Kumar *et al*., 2012).

In the literature, most FEM studies for transient loads focus on blast loads and the collision of solid bodies such as vehicle impact (Al-Thairy, 2012). The focus in the current study is transient loading caused by tsunami wave impact, nevertheless, the transient load caused by blast loading can be used as a point of reference since they have similarity in terms of the load vs. time profiles, i.e. short duration of the applied load. Existing research on finite element modelling with blast loads centres on the application of transient air-blast loads to many types of thin structures including a cylindrical shell (Clubley, 2014), quadrangular plates (Langdon *et al*., 2005), tubular steel (Jama *et al*., 2009), and offshore plates (Ali and Louca, 2008; Louca *et al*., 2004). The tested structural elements also consists of various materials including steel and aluminium (Bambach, 2008; Bambach *et al*., 2008; Jama *et al*., 2009), and also timber (Thampi *et al*., 2011). The other important aspects that play role in the modelling of blast loads are the boundary conditions (Bonorchis and Nurick, 2009), duration of loads (Clubley, 2014) and the stand-off distance between the explosive charge and the plate structure (Jacob *et al*., 2007).

Bonorchis and Nurick (2009) conducted the numerical modelling of rectangular plates subjected to localised blast loading. The AUTODYN-2D v6.1 software package with an Eulerian mesh was utilised for the explosive and air. The AUTODYN and similar codes are usually called “hydrocodes” that are particularly suitable for modelling blast, impact and penetration events. The AUTODYN software is able to handle complex problems where the Lagrange and Eulerian processors work side by side on the same problem. The Lagrange processor uses a mesh which deforms with the material and is typically used for solid continuum structures. The Eulerian processor has a fixed mesh in space which allows the material to move through it and is used for modelling gases, liquids or solids where large deformations are likely to occur. To model monolithic plates, the finite element program ABAQUS/Explicit v.6.56 was utilised. The steel plates were modelled and meshed using 3-D continuum 8-node linear brick elements with reduced integration and hourglass control (C3D8R). The edges of plates were clamped and meshed using 3-D 4-node discrete rigid brick elements (R3D4). The pressure load was applied using a Fortran VDLOAD subroutine in ABAQUS/Explicit. The numerical predictions were compared with experimental data for the plate midpoint deflection and plate deflection profile. By coupling the

AUTODYN and ABAQUS software, Bonorchis and Nurick (2009) has showed that the responses of rectangular plates under blast loading can be numerically well-predicted.

Sengupta *et al*. (2008) presented quasi-steady and transient wind load effects on a cubic building in a microburst and a tornado. The transient loading effects on a cubic building from a translating tornado for two different vortex core diameters were simulated using the tornado simulator. Measurements were made for two tornado vortex cases with core radii of 0.31 m (R1) and 0.56 m (R2), both had a maximum tangential velocity of 11 m/s. Aerodynamic force was measured on a 1:100 scale model of a 228.6 mm cubic building which was constructed with plywood. Two building orientations, normal and 45 degrees with respect to the tornado translation axis were tested. Tornado loading produced biaxial bending and twisting moments that are usually considered in design practice. Sengupta *et al*. (2008) did not extend their work to study the response of building subjected to high wind pressure generated by a tornado.

Thampi *et al*. (2011) conducted a finite element analysis regarding the interaction of tornados with a low-rise timber building. Tornados caused dynamic effects in terms of the changing internal and external pressures on the building. The finite element analysis was conducted following the experimental work. Thampi *et al*. (2011) used a full-scale building to be tested in their experiment. The chosen building was one-storey gable-roofed timber residential building with dimensions 15 m x 10 m that was located along the centreline of the tornado path (the Parkersburg tornado (EF5) of 25 May 2008). The reason for choosing this building was to compare the real condition of the observed building that was partially damaged with the predicted damage state of the building.

Thampi *et al*. (2011) used the ANSYS finite element (FE) software and utilized the shell and beam element to model the sheaths and studs of a timber building. The shell element is an 8-node quadrilateral structural shell with 6 degrees of freedom per node (ANSYS, 2009) and has shear, bending and membrane stiffnesses. The mesh size of the shell was set not more than 8 inches following the nail spacing on the plywood (as per IBC, 2006). The beam element has 6 degrees of freedom per node (ANSYS, 2009) and has axial and bending stiffnesses. Each connection was modelled by three independent non-linear springs with zero length to account for one axial and two lateral stiffnesses. The fixed boundary condition was used to simulate the sole plate anchorage to the ground.

The following failure criteria were chosen to determine the failure of the structural components. A complete failure is considered for the nails when the pullout exceeded 2 cm (ASTM-D1761-06, 2008). In addition to checking for loads, excessive deflection was also a reference for the failure of studs and sheathing components. The failure of the entire connection was considered when any one of the non-linear springs failed. The chosen failure criteria by Thampi *et al*. (2011) can be used as a reference to determine the failure of timber building components modelled using different finite element software.

4.3 The ABAQUS finite element model

As highlighted by the preceding studies, the finite element method is one of the most effective and accurate methods to simulate dynamic analysis of structures under impact loadings (Al-Thairy, 2012). The finite element analysis program ABAQUS/Explicit can be adapted to solve transient dynamic problems including blast and impact by applying explicit dynamic formulations. The explicit dynamic method is suitable for analysing high-speed and short-duration dynamics events such as tsunami wave impact that is investigated in present study (SIMULIA, 2010). Hence this thesis uses ABAQUS to model the transient response of a structure subject to tsunami bore impact.

ABAQUS/Explicit integrates the dynamic quantities (accelerations, velocities, dynamic stresses and strains) over the time increment where the dynamic quantities are extracted kinematically from one current time increment to the next one, while in the standard finite element procedure, the equations for dynamic quantities are solved simultaneously. The procedure implemented in ABAQUS/Explicit for calculating nodal accelerations, nodal velocities and nodal displacements ensure that the values at the end of any time increment are based on the same quantities as at the beginning of the current time step, making the method explicit. Thus, in order to achieve accurate results, the time increment must be small enough to assume the acceleration to be nearly constant throughout the time increment.

The simulation of the structure under transient impact loading includes the selection of the proper geometrical and material modelling parameters in order to gain accurate results. Moreover, other important aspects comprise the modelling of contact between elements, stability limit, time increment control and damping effects.

Geometrical modelling

The differences in the geometrical shape of structural members is represented by the use of the main element types such as solid, shell and spring elements (see Figure 4.1) which belong to the stress/displacement element library suitable for complex dynamic problems (ABAQUS, 2010). Solid elements are widely used in most numerical simulations and shell elements are used mostly for thin sections of structures, while a spring element can be used to model nails in a timber model for example. For solid and shell elements, ABAQUS/Explicit offers linear (first order) interpolation for calculating the internal stress and strains at any point in the element. Furthermore, to integrate various response outputs such as stress and strain over the solid and shell elements, ABAQUS/Explicit adopts a reduced integration technique that uses fewer Gaussian integration points than the full integration scheme. However, the application of a reduced integration technique and linear (first order) interpolation elements simultaneously leads to the so-called hourglass numerical problem and ABAQUS/Explicit introduces an artificial "hourglass stiffness" to overcome this problem. Linear elements with reduced integration have been implemented to model structural impact problems by Yu and Jones (1997), Zeinoddini *et al*. (2008), Dorogoy and Rittel (2008) and Thilakarathna *et al*. (2010).

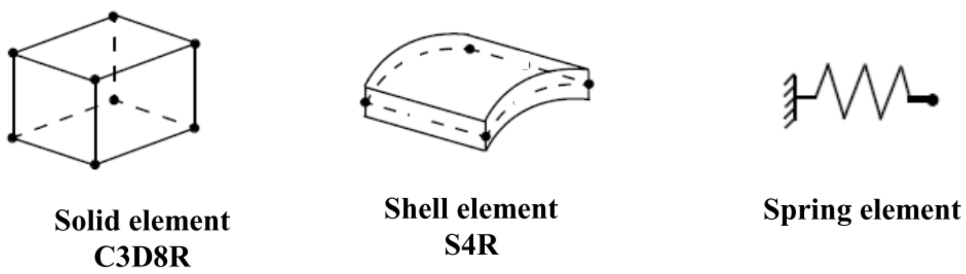

Figure 4.1 Linear brick, shell and spring elements in ABAQUS/Explicit

Material modelling

Johnson (1972) showed that high concentration stress waves propagate from the impact points towards other parts in a short of period of time when a body impacts a column. This stress concentration causes highly non-linear behaviour at the impact zone (Johnson, 1985). Following the impact events, a stress wave is generated and propagated along the column length causing global deformation and instability. To constitute both local and global deformations, the adopted material model must be able to trace the development and propagation of the yielding and inelastic flow of the material up to the failure point. Therewith, the strain rate and strain hardening effects are also important issues in the analysis of dynamic impact on a structure with strain rate sensitive materials.

4.4 Validation of finite element model: transient loading on plates

In this section, the results of model validations using ABAQUS version 6.10 will be presented. Two different cases were modelled based on experimental work by Jacinto *et al*. (2002), these being: Case 1 concerning the dynamic response of a blast loaded cantilever steel plate and Case 2 focussing on blast loading of a square plate fixed on all four edges are outlined in Section 4.4.1 and 4.4.2, respectively. Both cases were reviewed to demonstrate the capability of FEM in capturing the behaviour of structures under short duration impulsive pressures of a type similar to the transient loading of tsunami-like bores on coastal structures. In Case 1 and Case 2 the original experimental investigators also conducted their own numerical models using the finite element software ABAQUS/Standard 5.8. Herein, Case 1 and Case 2 were modelled to validate the efficacy of using ABAQUS 6.10 which will be used later in this work to simulate the dynamic response of timber structures under tsunami-like bore impact, as will be described in more detail in Chapter 6.

4.4.1 Dynamic response of cantilever plate (Plate A)

The structure that has been experimentally and numerically modelled by Jacinto *et al*. (2002) is a cantilever metallic thin plate and is referred to as Plate A. The dimension and boundary condition of Plate A can be seen in Figure 4.2. The dimensions of Plate A are 1 m wide, 1.5 m high and 2.1 mm thick, and the plate was assumed perfectly clamped at the bottom side. The material properties adopted for Plate A were: Young's modulus E = 180 GPa, Poisson's ratio ν = 0.3, density ρ = 7850 kg/m^3. Plate A was experimentally tested under blast loading and in the numerical analysis Plate A was loaded by a load-time history taken from the test as shown by Figure 4.3. The numerical dynamic analysis with 0.25 ms time step was conducted with modal superposition and the direct integration method applied to determine the stress. A mesh size of 5x5 cm was used in the model and this resulted in 600 mesh elements. The applied damping ratio was 0.6%.

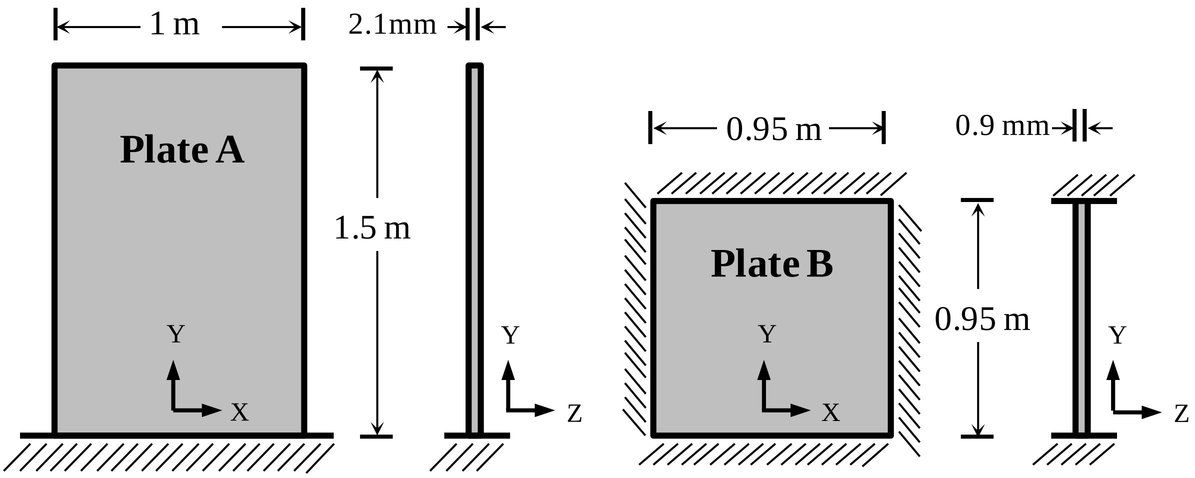

Figure 4.2 The sketch of Plate A and Plate B

To examine the influence of mesh size on the stress prediction, three different sizes of rectangular mesh were applied: 2.5x2.5 cm, 5x5 cm and 7.5x7.5 cm. The blast load-time history shown by Figure 4.3 (Jacinto *et al.*, 2002) was applied on the in-plane surface of Plate A and this load direction corresponds to the S22 (in the global Y direction) stress in ABAQUS . The mode shapes of the structure were examined along with the stress values and contours. For the results, it was found that the first four mode shapes of Plate A (see Figure 4.4) and also the frequency (see Table 4.1) are identical with associated mode shapes found by Jacinto *et al*. (2002).

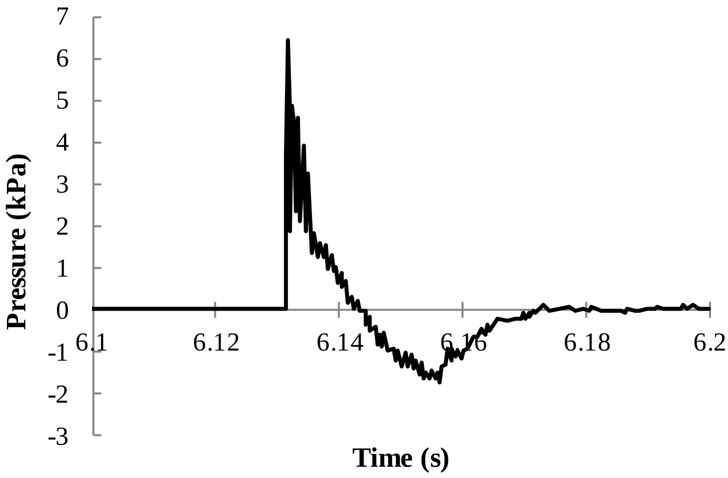

Figure 4.3 The blast load-time history for Plate A and Plate B (Jacinto *et al*., 2002)

The S22 stress values and contours are illustrated in Figure 4.5. The S22 stress is important because it shows the element stress in the global Y direction and this stress is the maximum with reference to the boundary condition of plate A which was a cantilever. It was found that a finer mesh gave higher S22 stress predictions. For the same mesh size, the maximum S22 stresses predicted by Jacinto *et al*. (2002) are slightly different with the results from the re-modelling one. This difference may due to imperfect figure-based re-plots of load time history taken from Figure 4 in Jacinto *et al*. (2002) and reproduced here as Figure 4.3.

Table 4.1 The comparison of frequency for the first four mode shapes of Plate A

Mode shape	Frequency		
	Experiment	Jacinto *et al*. (2002)	ABAQUS 6.0
1	0.72	0.74	0.7434
2	-	2.51	2.5090
3	4.99	4.63	4.6330
4	7.62	8.48	8.4787

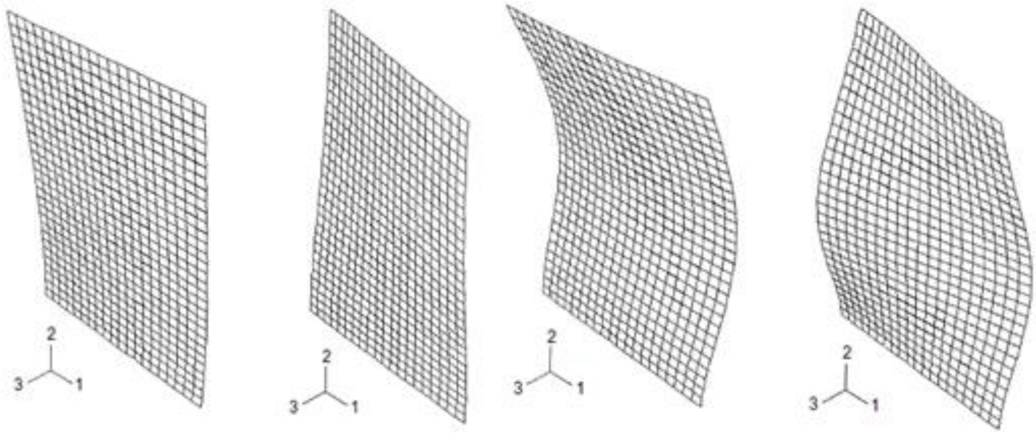

(a) First four modes of Plate A by Jacinto *et al*. (2002)

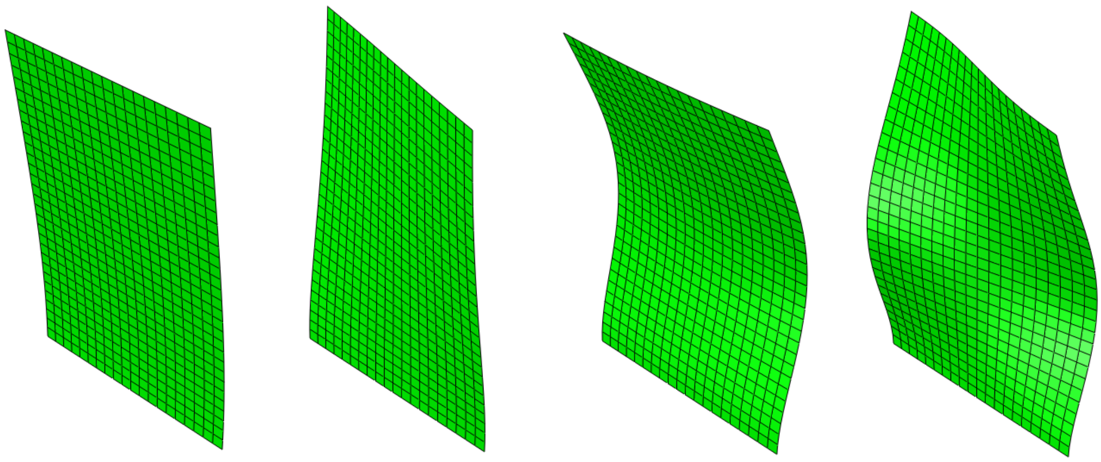

(b) First four modes of Plate A modelled using ABAQUS 6.10

Figure 4.4 The first four mode shapes of Plate A

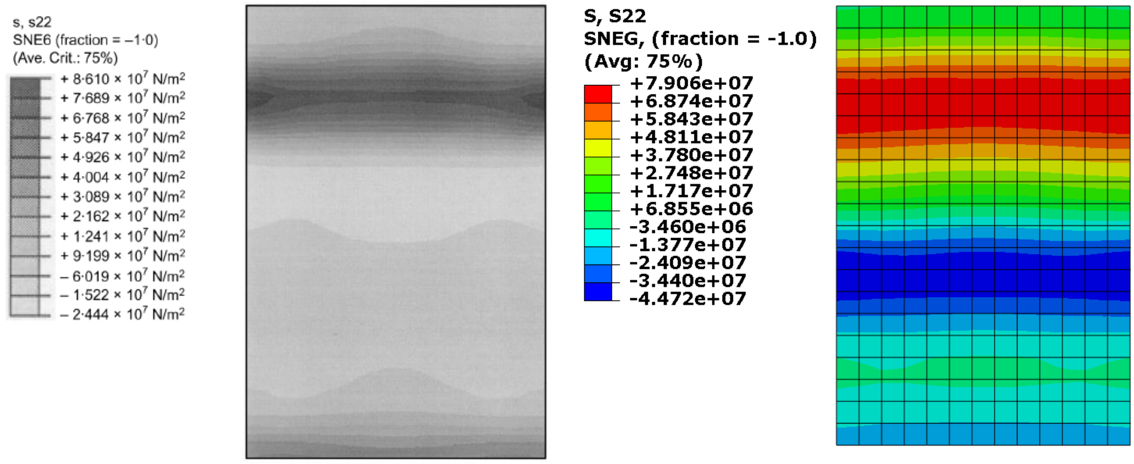

(a) Mesh size 5x5 cm (Jacinto *et al*., 2002) (b) Mesh size 7.5x7.5 cm

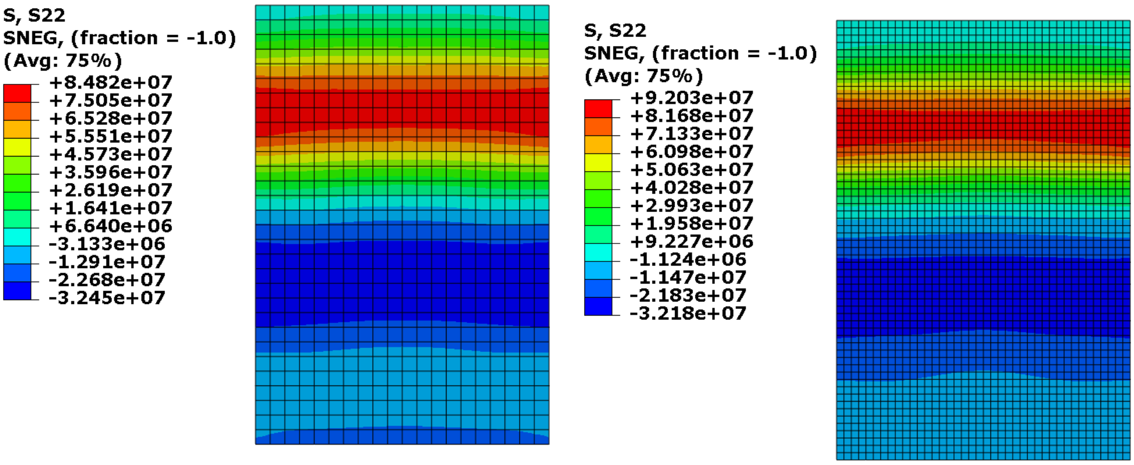

(c) Mesh size 5x5 cm (d) Mesh size 2.5x2.5 cm

Figure 4.5 The S22 (in the global Y direction) stress contours on Plate A based on different mesh sizes

4.4.2 Dynamic response of fully fixed plate (Plate B)

Plate B is a square metallic plate with the same material properties as plate A. The dimension of Plate B is 0.95 x 0.95 m with 0.9 mm thickness and clamped (i.e. fully fixed) around the four edges as illustrated in Figure 4.2. Jacinto *et al*. (2002) analysed Plate B with the same analysis method as with Plate A, but with a different damping ratio where the damping coefficient applied for the Plate B was 2.2% which was obtained experimentally. The mesh size for Plate B was 4.7x4.7 cm giving 20x20 mesh elements.

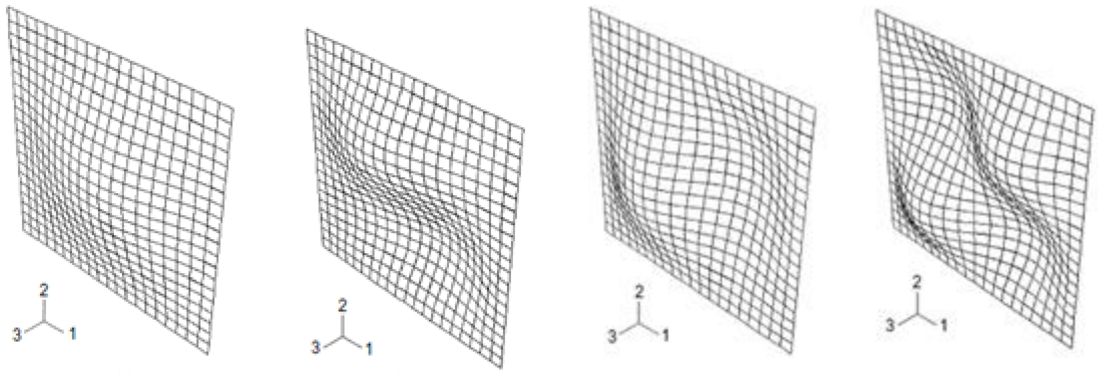

(a) First four modes of Plate B by Jacinto *et al*. (2002)

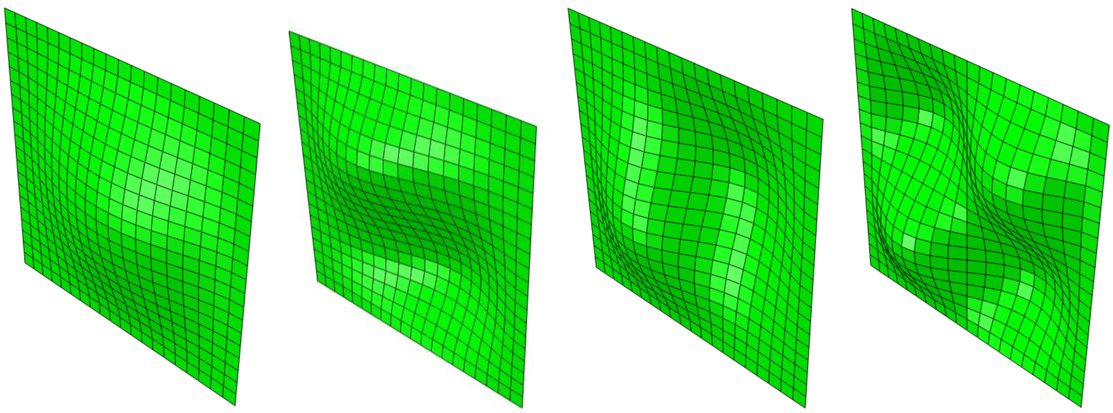

(b) First four modes of Plate B re-modelled

Figure 4.6 The first four mode shapes of Plate B

Plate B was also re-modelled using finite element software ABAQUS 6.10. Variation was made in the mesh size: 2.5x2.5 cm; 4.7x4.7 cm and 7.5x7.5 cm. The first four modes of Plate B are depicted in Figure 4.6 and these were found to be similar with mode shapes found by Jacinto *et al*. (2002). The mode frequencies were also comparable which can be seen in Figure 4.6a. Plate B is loaded in-plane using the load-time history shown by Figure 4 in Jacinto *et al*. (2002). For comparative purposes and based on the boundary condition of Plate B, the corresponding stress S11, i.e. stress in the global x-direction was used. The comparison of S11 stress between ABAQUS 6.0 and work done by Jacinto *et al*. (2002) can be seen in Figure 4.7 and it was found that the stress spatial distribution closely matches however, there is a little difference between the peak values, indicating the presence of mesh sensitivity. In both the experiments for Plate A and B, it was found that the plate did not yield, this is also suggested by the numerical results from the present study and by that conducted by Jacinto *et al*. (2002).

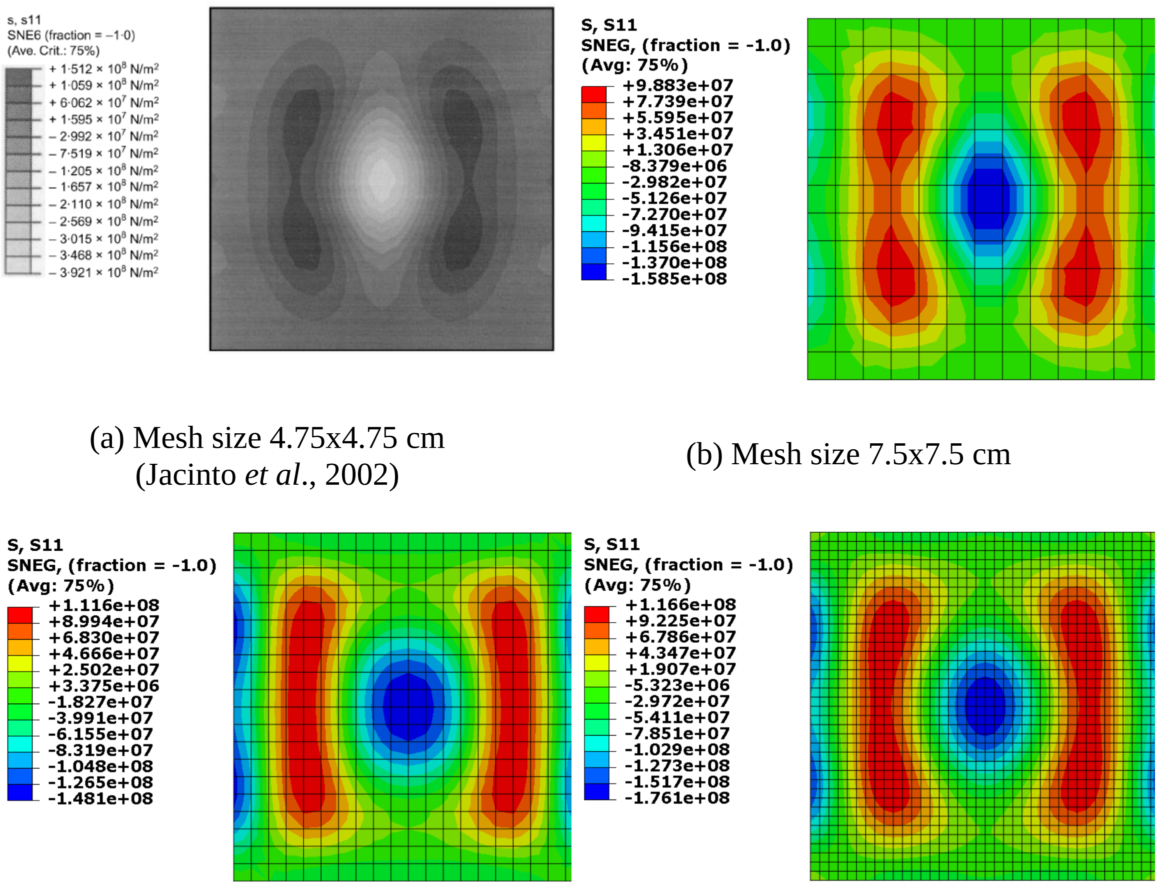

(a) Mesh size 4.75x4.75 cm (Jacinto *et al*., 2002)

(b) Mesh size 7.5x7.5 cm

(c) Mesh size 4.75x4.75 cm

(d) Mesh size 2.5x2.5 cm

Figure 4.7 The S11 stress contour on Plate B based on different mesh sizes

Table 4.2 The comparison of frequency for the first four mode shapes of Plate B

Mode shape	Frequency		
	Experiment	Jacinto *et al*. (2002)	ABAQUS 6.0
1	7.98	8.32	8.3197
2	16.22	17.14	17.141
3	23.70	25.23	25.233
4	27.94	31.32	31.326

4.5 Concluding remarks

The finite element modelling for structures under transient loading has been briefly described with special emphasis on the use of the ABAQUS software. The finite element modelling validation has also been performed for the simulation of blast loading on metal plates. The choice of using blast loading for the validation, besides the simplicity of the test cases, is due to the fact that because of the characteristics of air blasts loading are similar to those of transient tsunami bore impacts on structures. From the validation it was found that several parameters strongly influence the numerical response of the structure including the boundary conditions, damping ratio, mesh size and loading rate. Using the same approach as these validation tests, finite element modelling will be conducted on timber structures as will be discussed in Chapter 6.

Chapter 5

Hydrodynamic Modelling using DualSPHysics

5.1 Introduction

This chapter provides the results of the hydrodynamic modelling of tsunami bore impact using the DualSPHysics software. The simulation of tsunami-like wave impact on a 2-D non-discrete vertical wall is discussed and followed by the discussion for the results of tsunami-like wave impact on discrete rectangular and cylindrical structures in 3-D. The simulation of tsunami-like wave impact on a group of structures with different orientations is also included.

5.2 Tsunami bore impact on vertical wall in 2-D

5.2.1 Description of case: geometry

The sketch of the water tank and the set up of measuring probes for the simulation of tsunami bore impact on 2-D vertical wall can be seen in Figure 5.1. For this numerical simulation, data from experimental investigation of tsunami bore impact on vertical timber wall conducted in Oregon State University (Linton *et al*., 2013) will be used for comparison with the SPH model. The numerical water tank consists of a paddle wavemaker at the left-hand side, water particles and vertical wall at the right hand side. In the physical model, a 3.66 m wide x 2.44 m high timber stud wall was subject to forces from solitary waves. The wall was positioned on shore, just above the still-water line and spanned across the width of the test flume. The experimental tank was 104 m long with 1:12 sloping bed while the numerical water tank was simplified and has shorter dimension with 33.6 m long and 1:10 sloping bed. The application of smaller water tank dimensions was intended to reduce the number of particles and as a consequence reduce the time needed to complete the analysis. The depth of water in the numerical model was kept the same as in experimental model. To measure the water surface elevation during the experimental tests, 10 wire wave gauges (WG) and 4 ultrasonic wave gauges (USWG) were set along the water tank between paddle wavemaker and the wall. Due to the limitation of the model with a shorter numerical domain and the limited data available in the referenced journal article, the comparisons were performed only for 7 probes (WG3-WG10) which in the numerical model were placed at the same position as in the experiment. At the front surface of the vertical wall, numerical pressure probes were arranged vertically with spacing equal to the diameter of a particle and put at a distance $2h$ horizontally from the surface of the structure (where h is the smoothing length not depth h_0).

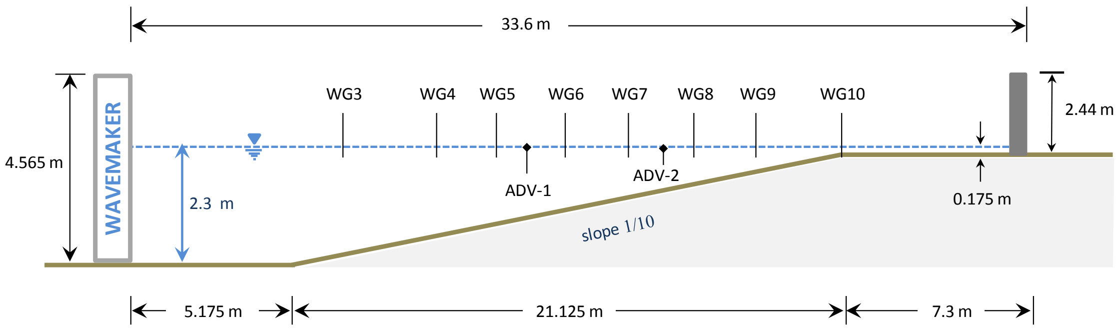

Figure 5.1 The boundary for the 2-D model of tsunami bore impact on vertical wall (not to scale).

Given the linear nature of the geometry, a 2-D approach was adopted for the numerical model. In SPH modelling, the particle size is a critical parameter affecting the accuracy of the model and the speed of analysis as shown in Chapter 3. For this model, a particle size of 0.02 m was adopted and this resulted in a total of 97,400 water particles in the model domain. In order to offset the effect of bed friction between the water particles and the boundary particles, the onshore areas were submerged (wet bed) by 0.175 m or just over eight times the particle diameter. As mentioned, the length of the numerical flume was reduced to minimise the number of SPH particles involved;

this also allowed a reduction in the analysis time. In comparison with the experimental work, this reduction in flume length caused the distance between the paddle wave-maker and the wall structure to be approximately 45% shorter. The position of the paddle, which is 5.175 m from the toe of the slope, is designed to maintain an accurate model of the wave characteristics, critically the water surface elevation, velocity and pressure. The tsunami-like waves were generated by using Goring's method (Goring, 1978), which is similar to the method used in the experiment. Based on Goring's method, for a still- water height of 2.3 m, the best approximation to experiment is given when H/h_0 (targeted wave height to still-water height) equals 0.9. To generate the targeted wave height in this simulation, the maximum stroke of the paddle is 1.6 m and the paddle trajectory is depicted in Figure 5.2. In this SPH model, due to the reduction in the length of the model, WG1 and WG2 were outside the numerical domain, so no data are available for comparison regarding these probes. For comparison purposes, data from eight probes (WG3 to WG10) were investigated.

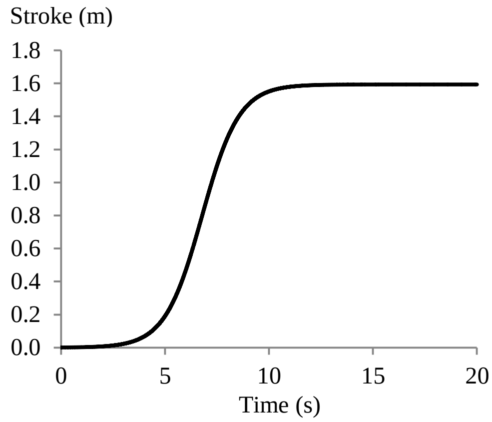

Figure 5.2 Paddle trajectory of the numerical model

5.2.2 Water surface elevations

Figure 5.3 shows the water surface elevation at eight probes that were placed in the numerical model at similar distances from the wall to the experimental test. Overall, the numerical prediction is in good agreement with the experimental results. It can be clearly seen from the graph in Figure 5.3 that the best prediction of numerical modelling is at WG6, which is 17.5 m from the wall or around the half-length of the numerical tank where the bed is sloping. Closer to the wall, the numerical water surface elevations slowly decay, but are still in an acceptable range as compared with measured data. Following modification of the length of the tank, the generated numerical waves were targeted to match the experimental wave properties (water surface elevation) at the location of at least one probe as it propagates along the tank. Based on several trials, the best prediction of wave surface elevation occurred at a probe located in the mid-length of the tank. So, this probe was then used as a reference and the numerical time simulation was then shifted to mimic the wave profile at this probe. The numerical water surface elevations at other probes thereupon follow the reference probe. This may explain the observed wave decay in Figure 5.3, in addition to the fact that the decaying wave may also result from the loss of energy during its propagation. The largest difference between numerical prediction and physical data occurs at WG3, where the numerical model prediction is 12.4% higher than measured data. (Note that quoted % differences henceforth are based on numerical value/experimental value.) The reason for this is that WG3 is the closest probe from the numerical paddle where the generated wave still has much energy, while the experimental wave has already propagated much further.

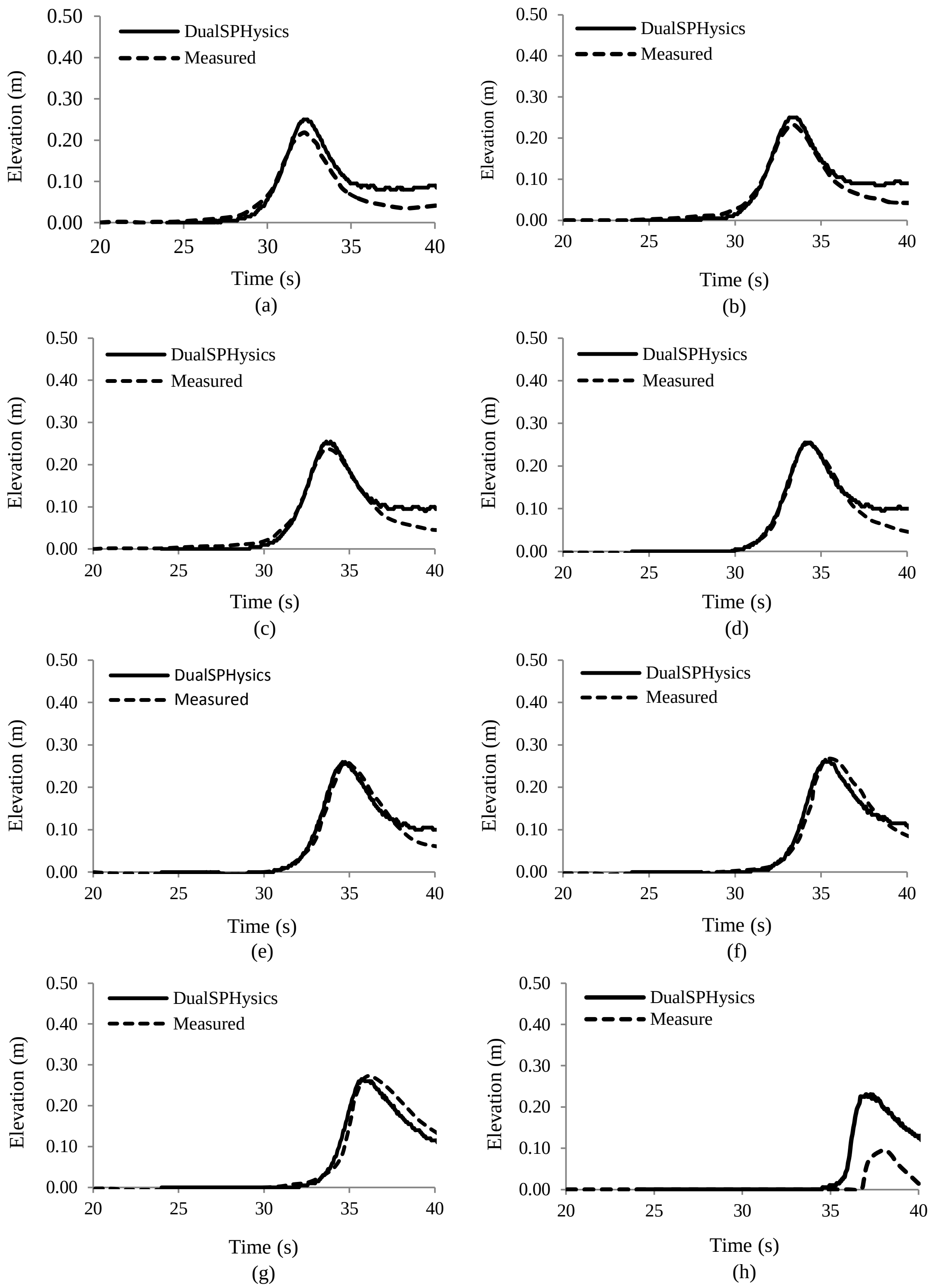

Figure 5.3 Comparison of water surface elevation measured at wave gauge (WG)

(a) WG3 (25.39 m from the wall); (b) WG4 (20.72 m from the wall); (c) WG5 (18.88 m from the wall); (d) WG6 (17.05 m from the wall); (e) WG7 (15.21 m from the wall); (f) WG8 (13.07 m from the wall); (g) WG9 (10.93 m from the wall); (h) WG10 (6.89 m from the wall)

5.2.3 Wave Velocity

Figure 5.4 shows the velocity of solitary waves during its propagation from offshore. Figure 5.5 depicts the snapshot of the 2-D numerical simulation in DualSPHysics as the wave impacts the wall. Figure 5.5(a) shows the velocity contours of the water particles, where the maximum velocity occurs at the leading tip of the wave and gradually decreases to the minimum at the corner and bottom areas of the boundary. The maximum velocity is nearly 1 m/s. Figure 5.5(b) shows the associated pressure contour of the water particles where the maximum pressure is just less than 4 kPa. Numerical pressure probes (not shown) are located at 2*h* in front of the back wall at vertical intervals of 0.02 m from the bed. Figure 5.6 shows that the numerical model prediction underestimates the velocity of wave as compared with the measured velocity. At velocity probe ADV1 which is 17.97 m from the wall, the numerical model maximum velocity is 0.52 m/s, which is approximately 20% lower than measured maximum velocity. Similarly, the velocity at probe ADV2 which was placed 3.68 m next to the ADV1, the numerical model maximum velocity is 0.63 m/s, this is approximately 19% less than measured data.

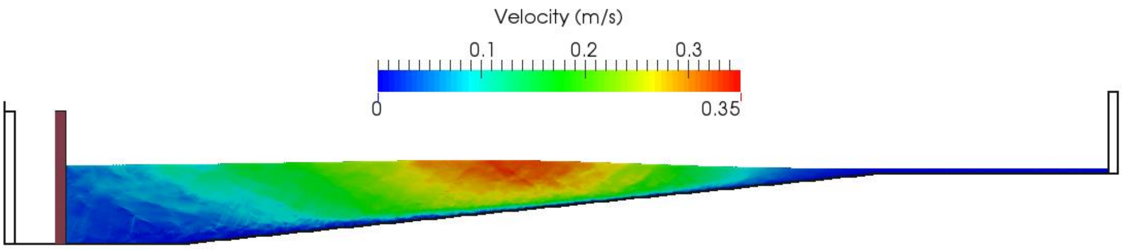

Figure 5.4 The offshore velocity of propagating solitary wave

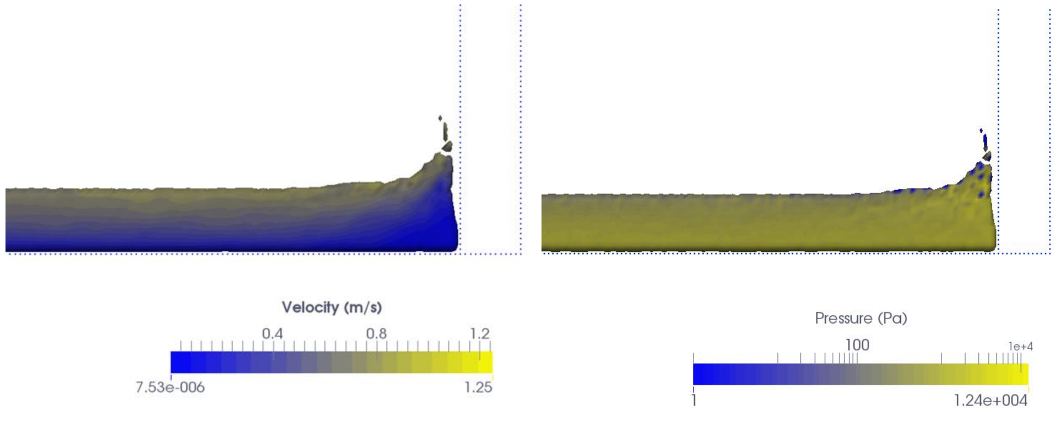

(a) (b)

Figure 5.5 SPH model output showing wave impacting at wall: (a) velocity; (b) pressure

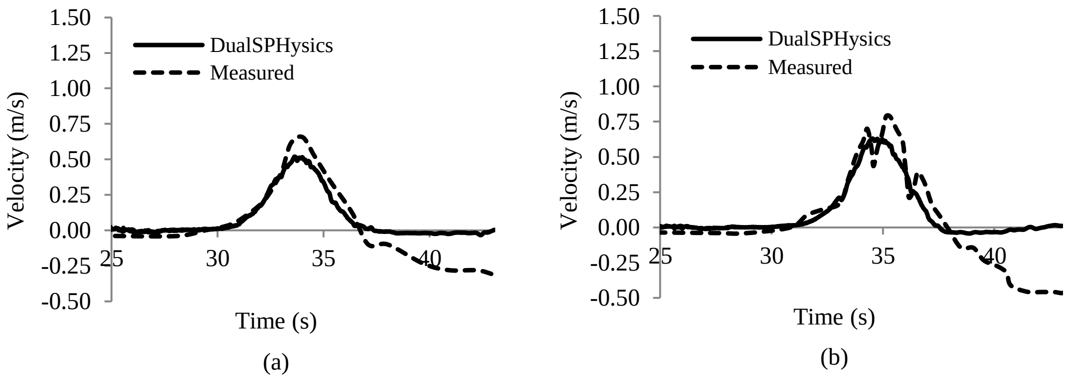

Figure 5.6 Comparison of water velocity: (a) velocity at ADV1 (17.97 m from the wall); (b) velocity at ADV2 (14.29 m from the wall)

5.2.4 Water Pressure

In the experiments of Linton *et al*. (2013), as the wall experienced impact forces, the pressure over time was collected by two sensors that were placed at heights of 0.2 m and 0.64 m from the toe of the wall, as shown by Figure 5.7. At this juncture, it is useful to explain the process of obtaining the numerical pressures within DualSPHysics by way of the MeasureTool function. The MeasureTool is able to compute different physical quantities such as pressure, velocity and water surface elevation, at a set of given points. The MeasureTool can also compute the magnitude of physical quantities at locations that change position with time, such as moving particles. The use of numerical pressure values to compute force is explained in detail in Section 5.3.3. As described by Figure 5.7, the measured peak value of wave pressure at the lower (height = 0.2 m) sensor P2 is 4.69 kPa, whereas the numerical sensor prediction is 5.46 kPa, which is 16.4% higher than the measured value. Even though the peak values are different, the pressure pattern over time shows comparable behaviour, as shown in Figure 5.7. Moreover, at the higher (height = 0.64 m) sensor P5, both measured pressure and numerical prediction are very close when considering the peak value. The short duration of pressure at P5 indicates that a small number of numerical particles act at this level of elevation. From the numerical pressure data it can be read that the leading tip of the wave reaches over 0.7 m in height of the wall, which is only about three times the particle size from P5, so this may explain the short duration of wave occurrence. The snapshots of wave pressure contour taken at different times in the simulation are depicted in Figure 5.8.

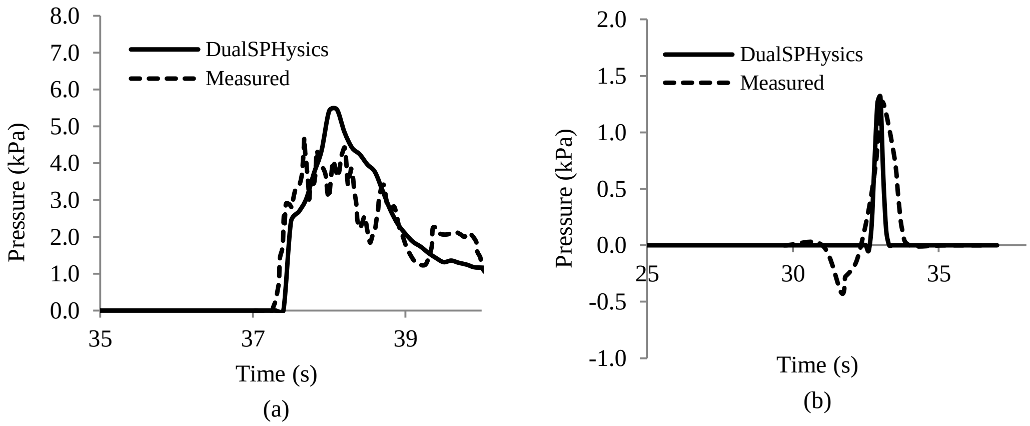

Figure 5.7 Comparison of pressure on wall surface: (a) pressure at P2 (height = 0.2 m from toe of wall); (b) pressure at P5 (height = 0.64 m from toe of wall)

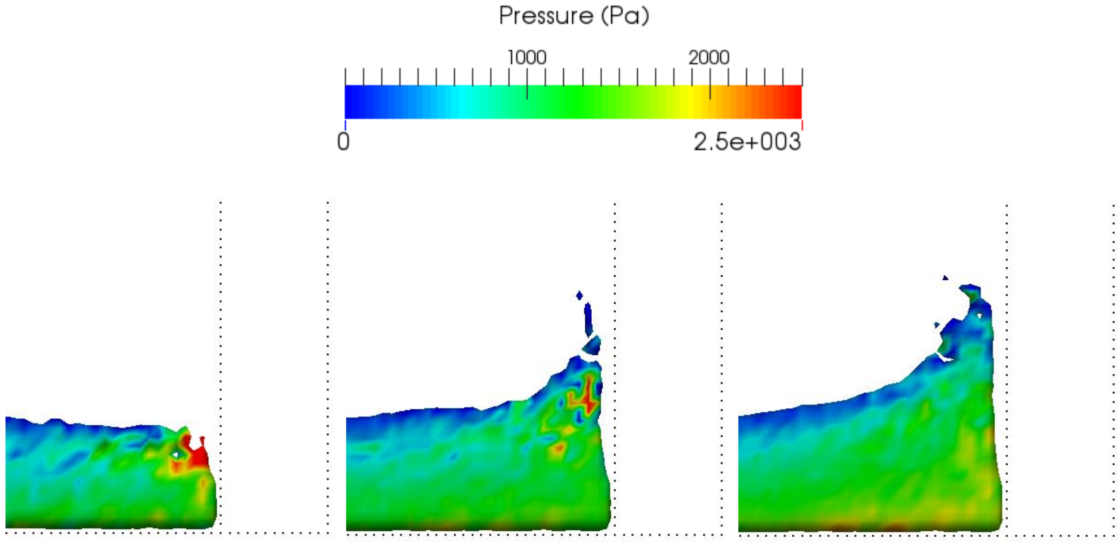

(a) (b) (c)

Figure 5.8 The pressure contours as the wave impacts the wall: (a) maximum impact at t = 306 sec; (b) post impact at t = 310 sec; and (c) maximum runup at t = 313 sec.

5.3 Tsunami bore impact on a discrete rectangular structure in 3-D

5.3.1 Description of case: geometry

The boundary of the 3-D model domain was designed to mimic a nearshore topography and this is a typical boundary used by researchers to simulate tsunami wave impact using a water tank in laboratory (Thusyanthan and Madabhushi, 2008). It consists of an offshore region containing water with a certain height, an inclined seabed and onshore section where the coastal structure is located. The location of the paddle, the flat bed, the incline beach, the flat land and ratio of wave height to water depth are chosen to ensure a broken bore is impacting the structure. The geometry of the water tank used here is shown in Figure 5.9 where the total dimension is 15 m long and 5 m high. The tank was designed to have 2 different alongshore widths: 3 m and 5 m, to enable the structure to be placed either 1 or 2 metre distances from the side wall, respectively. With those variations, contributions of different structure-to-wall distance on force acting on the structure will be examined.

A notation of D was used in the model to represent a characteristic length or distance (1 m) such that the size of model components or lengths in the geometry was a multiple of D. For example, the size of structure and the depth of still water are D, the distance of the structure to the shoreline and to the rear boundary wall are $2D$, and the width of water tank and the height of paddle wavemaker are $3D$. This was intended to help non-dimensionalise the analysis results. This non-dimensional value will be necessary for its application at different scales. Figure 5.9 shows an eye which is intended to give a direction from where the pressure distribution can be viewed and this is related with snapshots shown later in Section 5.3.4.

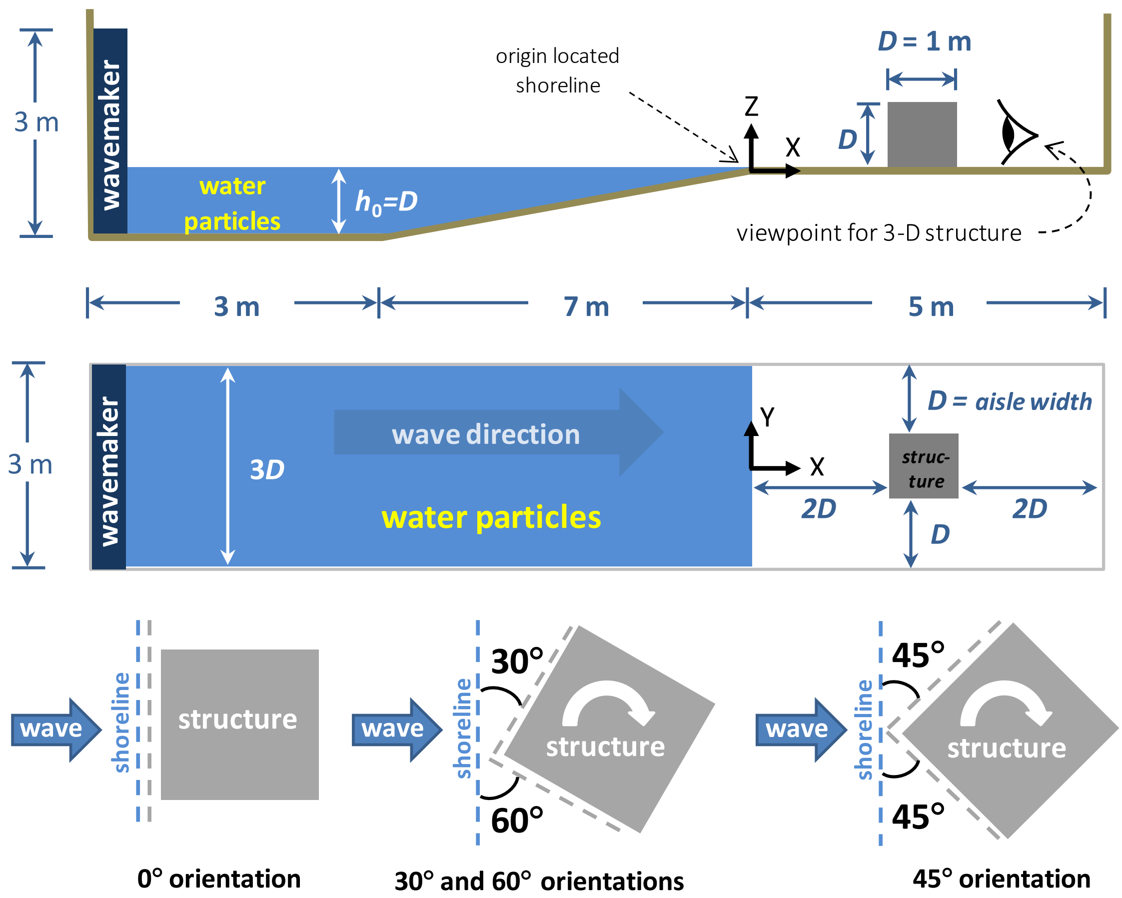

Figure 5.9 The side and top view of 3-D model with simple structure with different orientations (not to scale)

The parameters used in the simulations consist of structure orientation (angle of rotation which is sometimes referred to as angle of attack), wave height and aisle width. The wave heights were designed based on the ratio of the targeted wave height and still water level (H/h_0). Three different values of H/h_0 were used: 0.1, 0.3 and 0.5 that provide the respective wave height 10, 30 and 50 cm for h_0 = 1 m. Those wave heights generate a broken bore as it reaches onshore and impacts the structure. Variation of the aisle width and hence the distance from the structure to the side wall helps to represent the presence of neighbouring structures.

In the case of wave impact on a discrete structure, the numerical modelling was performed in 3-D to study the impact of the wave on a structure with different orientations. A simple rectangular structure was chosen as a representative of a coastal structure as an impact target. The dimensions of the rectangular structure are 1m x 1m x 1m which is treated as a cube. The structure with one of its surfaces normal to the direction of incoming wave was used as the reference (zero degree orientation). Variation in surface orientations for other cases was undertaken by rotating the structure around its vertical axis. The design angles of the surface of structure for other cases were 30, 45 and 60 degrees. All these orientations were run in different simulations, except for the 30 and 60 degrees that can be represented by a single simulation with one structure.

The total number of simulations for cases with different orientations in this sub-chapter is 18. The details can be seen in the following Table 5.1. The results for all cases were focused mainly on wave impact pressure on the surface of structures. Other data collected include wave velocity, wave height, wave impact pressure on boundary wall surrounding the structures, and also wave transformation such as wave diffraction as the wave passes around a barrier.

Table 5.1 Run simulations for structure with different orientations

Orientation	H/h_o	Aisle width, D	Run case
0-degree	0.1	D, 2D	2
	0.3	D, 2D	2
	0.5	D, 2D	2
30&60-degree	0.1	D, 2D	2
	0.3	D, 2D	2
	0.5	D, 2D	2
45-degree	0.1	D, 2D	2
	0.3	D, 2D	2
	0.5	D, 2D	2
Total number of run cases			18

5.3.2 SPH Parameters

The SPH simulation parameters used are identical to those presented earlier during the convergence study in Chapter 3. The number of particle layers for the boundary in the SPH model known as lattice number was set equal to two which means that the boundary line composed by a double layer of particles. This double layer of particles is effective to prevent water particles penetrate the boundary location.

The zero axes for the numerical models lies within the model domain and located at the shoreline as shown in Figure 5.9. Since DualSPHysics is a single precision code, the position of zero axes can influence the accuracy of measurements of quantities such as pressure. In other words, a model with the zero axis located inside the domain is less likely to suffer from precision errors than when its zero-axis position is situated at the end of or much further from the model domain (Longshaw and Rogers, 2015). Another advantage of the zero axis position inside the domain, at the shoreline in this model for instance, is the ease to modify parts of model at both end of the water tank. For example, when it is necessary to adjust the paddle distances from shoreline or change the positions of coastal structure (together with the measuring probes) at the opposite end of water tank, it can be done without changing large parts of the *xml* input file.

The choice of water particle size (d_p) is crucial in SPH modelling. It largely influences the overall simulation including the behaviour of waves, the accuracy of pressure prediction and the time simulation. As a rule of thumb, the size of the initial particle size can be taken as 1/10 of the shortest characteristic length in the model; however there is no exact rule since every model is unique. An inter-particle distance of $L/20$ or 0.05 m is used in all models with discrete structure. This particle size was based on the convergence study presented in the preliminary SPH dambreak test as described in Chapter 3. In the *xml* DualSPHysics input file, the lattice number for boundary water particles is set equal to one, following a comparison that shows no significant difference in terms of wave impact pressure when using single or double layer of particles for the water.

5.3.3 Description of procedure for computing pressures and forces on structure

The output of DualSPHysics provides the time history of pressure value for each numerical measuring probe. This pressure value can be used to estimate the force. As illustrated in Figure 5.10, the force (F_i) per unit length of a particular probe in a 2-D model is obtained by multiplying its pressure (P_i) with the associated height (Δz_i), see Equation (5.1). Thus, the total force (F) in a 2-D model is the sum of the forces for the total number (n) of measuring probes and can be calculated using Equation (5.2). Similarly, the force (F_i) at a certain point in a 3-D model can be determined by multiplying the pressure (P_i) with the area (A_i) of probe i, see Equation (5.3). Hence, the total force (F) acting normal to a surface can be determined using Equation (5.4) by summing the total number (n) of forces acting on the surface.

For 2-D

$$F_i = P_i \Delta z_i \tag{5.1}$$

$$F = \sum F_i = \sum_{i}^{n} (P_i \Delta z_i) \tag{5.2}$$

For 3-D

$$F_i = P_i A_i \tag{5.3}$$

$$F = \sum F_i = \sum_{i}^{n} (P_i A_i) \tag{5.4}$$

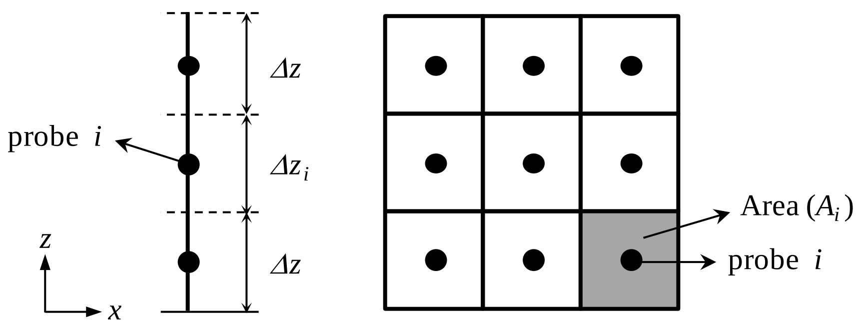

(a) 2-D (b) 3-D

Figure 5.10 The arrangement of probes in a line for (a) 2-D model and (b) in an area for 3-D model

The measuring probes were placed at several locations inside the model domain. Probes for measuring wave velocity and wave height were placed along the longitudinal axis of the tank shown in Figure 5.1. For the structure, the pressure probes were evenly distributed on all surfaces of the cube structures (following structure's orientations) and on the surface of surrounding boundary walls, see Figure 5.11. The spacing of pressure probes on structures surface facing the incoming waves is 0.05 m or similar with the diameter of particles. This 0.05 m spacing was chosen to capture pressure distributions that in previous trials were unable to be perfectly captured by probes with 0.2 m spacing distance or greater. The pressure probes spacing on the surface of surrounding walls are set equal to 0.2 m and 0.25 m since those areas are larger, less prominent and of less interest. The probes start at height of 0.05 m from the bed.

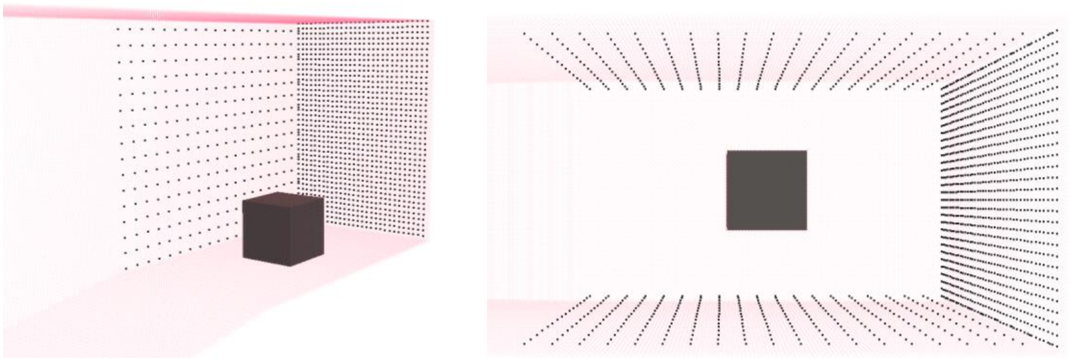

(a) (b)

Figure 5.11 Pressure probes (black dots) on boundaries; (a) side view and (b) top view.

5.3.4 Numerical simulation results of discrete rectangular structure in 3-D

This section discusses the tsunami bore impact pressures for the simulations presented in Table 5.1. The normalised peak pressure values ($P/\rho g h$) exerted on the structure's surface are given in Table 5.2. The numerical modelling results show that the structure's orientation influences the pressure imposed by the structure. The bigger the degree of rotation, the lower the peak force exerted on the surface of structure. This is because the magnitude of the pressure directly proportional to the surface area facing the oncoming waves. A smaller aisle width (shown in Figure 5.9) is equivalent to a reduced spacing between the discrete structure and an adjacent larger building. Therefore decreasing the aisle width corresponds to increasing the blockage ratio (structure width to channel width) and hence the build-up of pressure during the bore impact.

Table 5.2 Normalised peak pressure values ($P/\rho g h_0$) based on orientations of structure

Row number	Case		Degree rotation			
	Aisle width	H/h_0	0	30	45	60
1	2D	0.5	2.913	1.548	1.167	0.672
2	2D	0.3	2.459	0.942	0.537	0.377
3	2D	0.1	0.136	0.094	0.096	0.077
4	1D	0.5	3.036	2.018	1.539	0.928
5	1D	0.3	1.889	0.747	0.400	0.405
6	1D	0.1	0.293	0.117	0.075	0.087

The structure's orientations also influence the total force on its surfaces. This can be seen from Figure 5.12 which shows the comparisons of total force as it varies over time on the surface of an individual face for different orientation of structures. From Figure 5.12, the larger the projected area exposed to the incoming waves, the higher total force imposed by its surface. In Figure 5.12(a), for wave with $H/h_0 = 0.5$, the force patterns for all degree orientations show small variation. However, for the other $H/h_0 = 0.3$ and 0.1, the force patterns between 0-degree and other degrees are different and this difference shows that for weaker bore, the first impact was only significant for the 0-degree structure orientation.

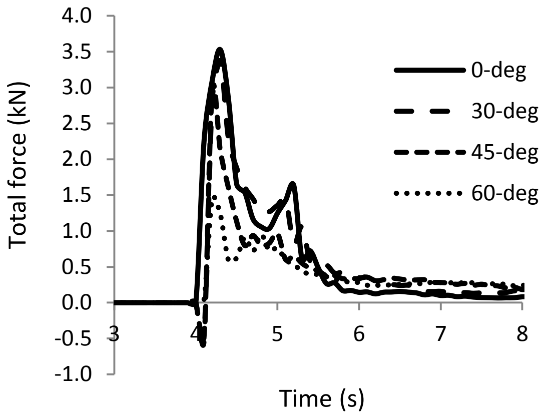

Figure 5.12(a) H/h_0 = 0.5

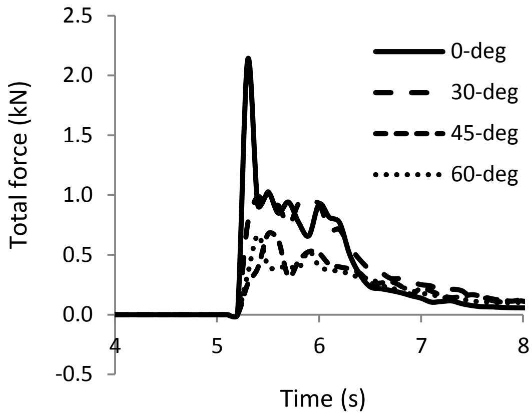

Figure 5.12(b) H/h_0 = 0.3

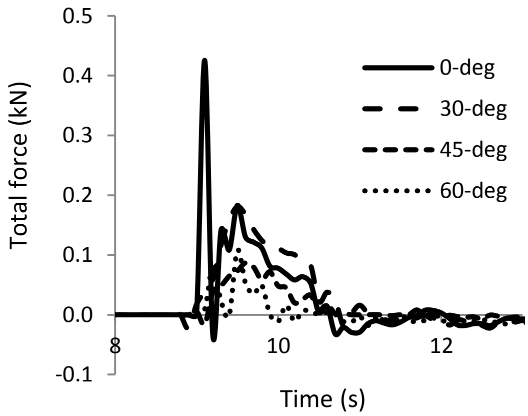

Figure 5.12 (c) H/h_0 = 0.1

Figure 5.12 Total force on the surface of structures with different orientations

5.3.4.1 Water surface elevation

Previous validation for the SPH water surface elevation generated by a solitary wave was presented by Cunningham *et al*. (2014). Here, we present the results for different wave height to water depth ratios. Figure 5.13 shows the probe positions for measuring water surface elevation regarding the propagation of the solitary wave for cases with different H/h_0. The water surface elevations were measured at certain probes along the tank. H1 is placed 1 m from shoreline and followed by H2 through H7 at a constant 1 m spacing. The properties of the offshore solitary waves and onshore bores can be seen from Figure 5.14 and Figure 5.15 and also from Table 5.3.

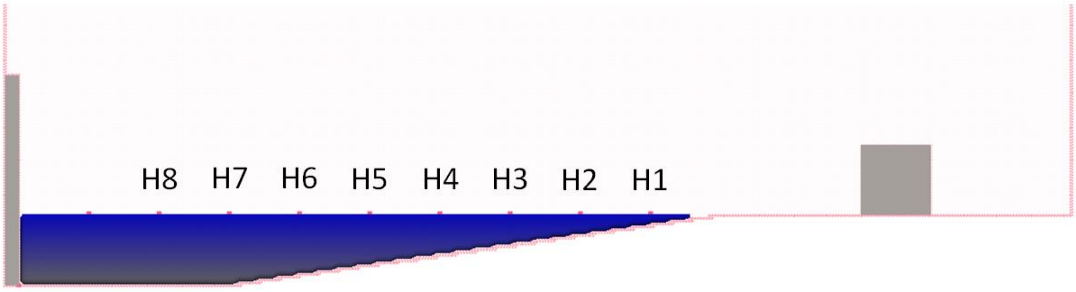

Figure 5.13 Layout of water surface elevation probes H1-H7

Figure 5.14 depicts the SPH simulation of the solitary wave propagation offshore for the case with H/h_0 = 0.5. From the four snapshots given in Figure 5.14(a) to Figure 5.14(d), the changes in the solitary wave profile/shape can be observed. Near the shoreline at probe H1, the solitary wave started to break and its elevation decreased as illustrated in more detail in Figure 5.15.

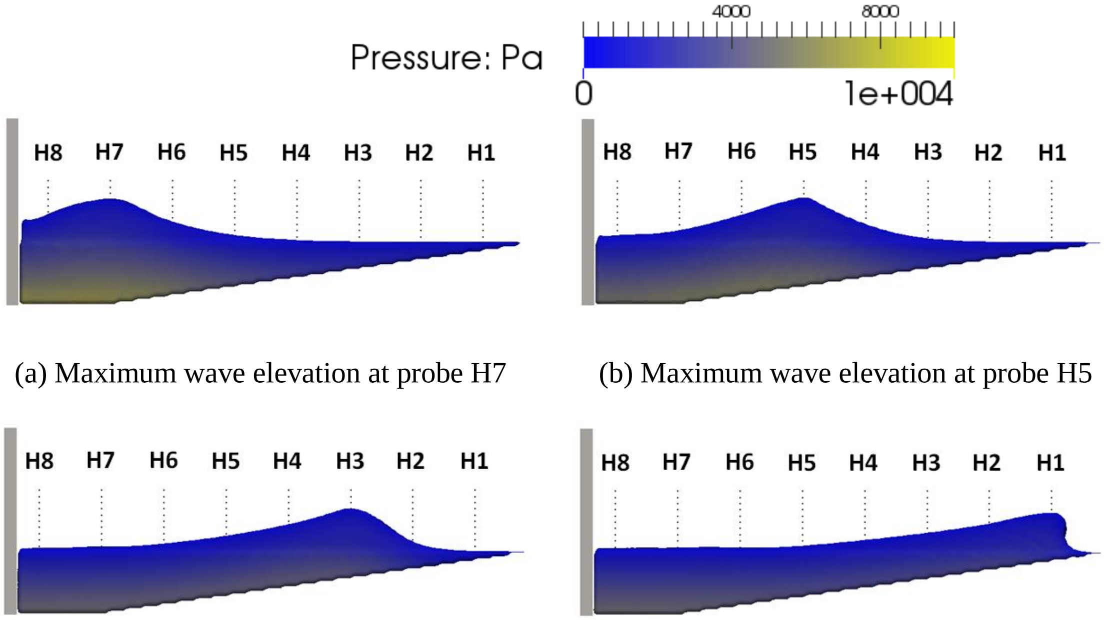

(a) Maximum wave elevation at probe H7

(b) Maximum wave elevation at probe H5

(c) Maximum wave elevation at probe H3

(d) Maximum wave elevation at probe H1

Figure 5.14 SPH simulation of solitary wave height and pressure during propagation from probe H7 through probes H1 for case with H/h_0 = 0.5

Figure 5.15 shows the comparison of solitary wave elevations based on different *H/*h_0 during propagation towards the shoreline.

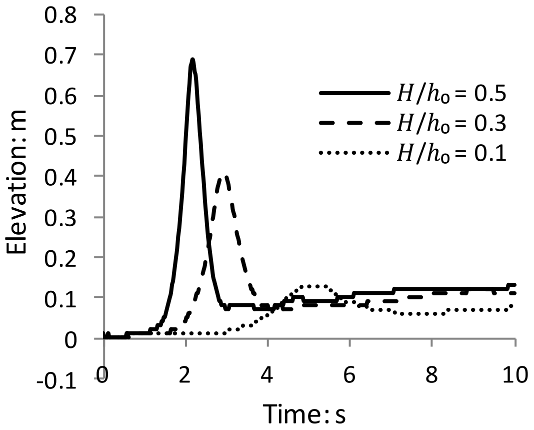

(a) Probe H7

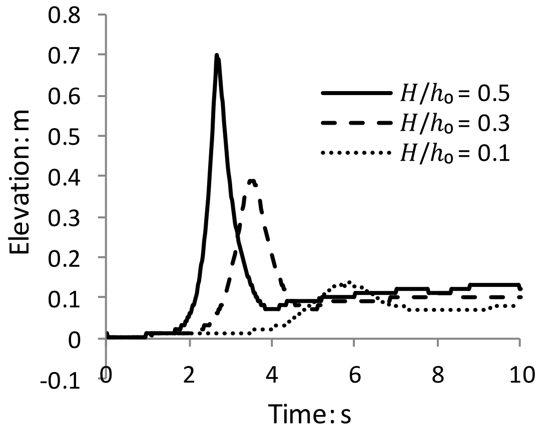

(b) Probe H5

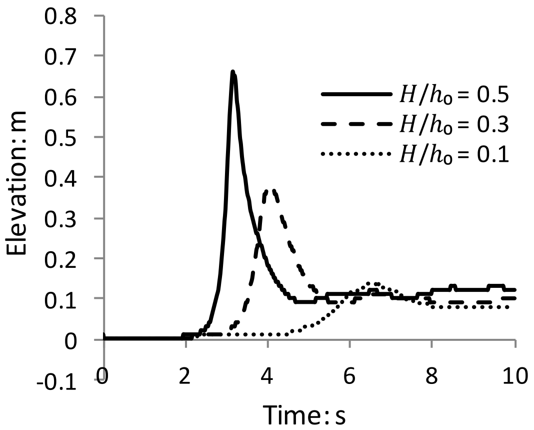

(c) Probe H3

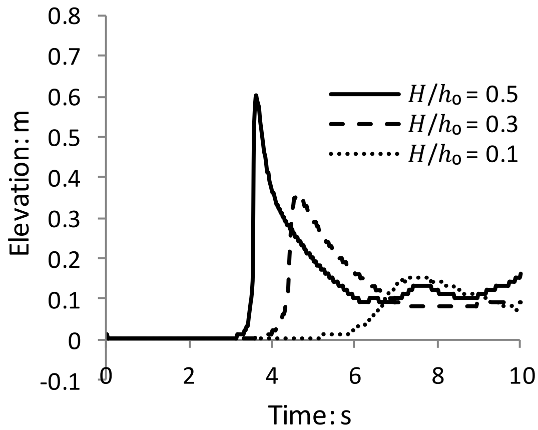

(d) Probe H1

Figure 5.15 The comparison of solitary wave elevations for different H/h0 measured at probe H7, H5, H3 and H1.

The surface elevations were measured at four different probes H7, H5, H3 and H1. The wave elevations were measured from the surface of water at rest. From H7 until H1, it can be seen that generally the solitary wave elevation slowly decreases. The maximum elevations of the solitary wave for the case with H/h_0 = 0.5 is almost 100% higher than the case with H/h_0 = 0.3, and almost three times higher than the case with H/h_0 = 0.1. The differences in wave elevation correspond to the differences of the associated bore impact forces on the structure.

5.3.4.2 Bore Height and Velocity

The onshore bore heights and velocities were measured by probes placed in front of the structure. The values of these properties are important in determining the exerted pressure on the surface of structure. The snapshots of the bores including velocities can be seen in Figure 5.16 and the variation of bore heights are depicted in Figure 5.17, for simulation cases with H/h_0 = 0.3 and 0.5.

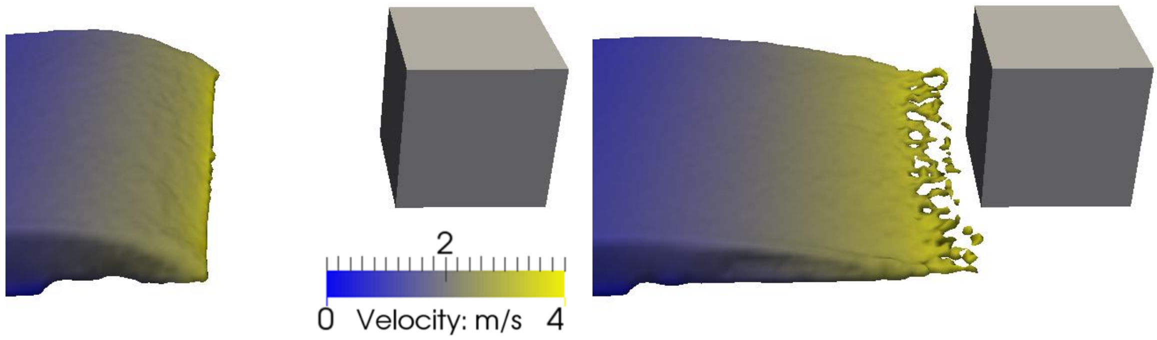

(a) near the shoreline (b) onshore

Figure 5.16 SPH simulation of bore velocity for the case with H/h_0 = 0.5.

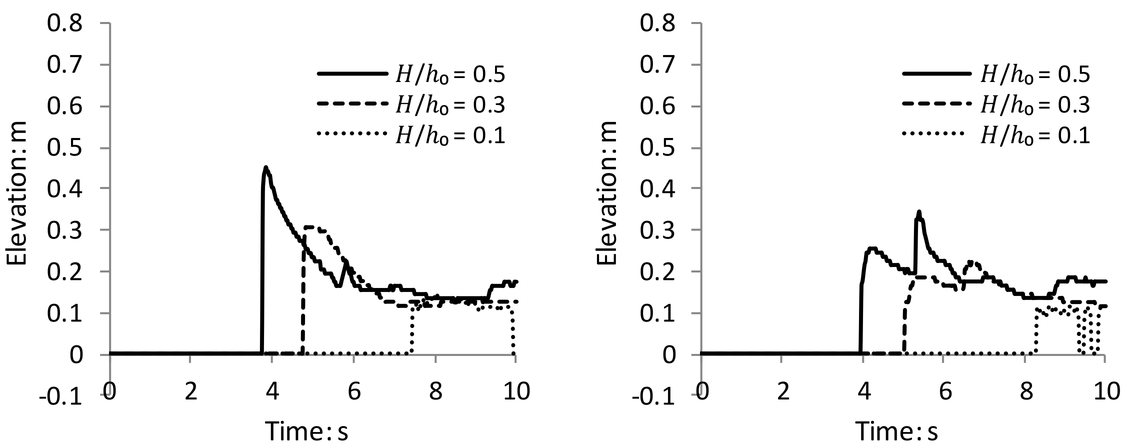

(a) Shoreline (b) Onshore

Figure 5.17 Bore height measured from still water level at (a) shoreline, (b) onshore.

Table 5.3 shows the offshore water surface elevation and wave length of solitary waves and the corresponding onshore bore characteristics (height and velocity). It can be observed that offshore, the maximum velocity increases proportionally with the design height of the solitary wave. The maximum solitary wave velocities offshore are also proportional to the bore height and velocity onshore. This is in general qualitative agreement with bore impact behaviour. Direct comparisons are not made with other numerical techniques, such as Boussinesq-type approach, since they do not model violent flow.

Table 5.3 Solitary wave and bore properties

H/h_0	Offshore solitary waves			Onshore bores	
	Maximum elevation	Maximum velocity	Wave length	Maximum height	Maximum velocity
0.5	0.7 m	3.94 m/s	5.0 m	0.32 m	5.65 m/s
0.3	0.4 m	2.13 m/s	6.5 m	0.20 m	4.05 m/s
0.1	0.15 m	0.68 m/s	7.7 m	0.11 m	1.19 m/s

5.3.4.3 Pressure for structure with orientation θ = 0°

The thesis now takes advantage of using SPH to investigate the effect of structure orientation. Initially a zero degree orientation is described. Typical output from the 3-D SPH simulation is shown in Figure 5.18 and Figure 5.19 for the case with H/h_0 = 0.5. Figure 5.18a depicts the snapshot of a propagating solitary wave which is then followed by a bore impact on the structure as shown by Figure 5.18b. The peak pressure impact occurred at t = 4.150 sec and the peak pressure took place at the lowest level of pressure probes as indicated by the circle in the Figure 5.19a. In addition, Figure 5.19b shows the pressure distribution for the maximum bore run-up on the surface of the structure that occurred at t = 4.325 sec and corresponding with Figure 5.18b. Pressure distributions in Figure 5.19 were seen from the rear of the structure (see illustration indicating direction of view in Figure 5.9) by assuming the cube structure is visually transparent.

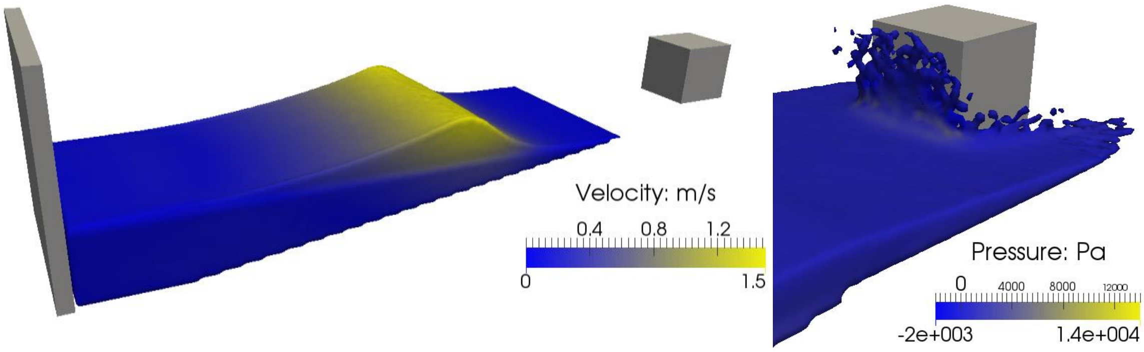

(a) (b)

Figure 5.18 Oblique view of the 3-D simulation for case $H/h_0 = 0.5$; (a) solitary wave propagation at t = 3.150 sec., (b) bore impacting structure at t = 4.325 sec.

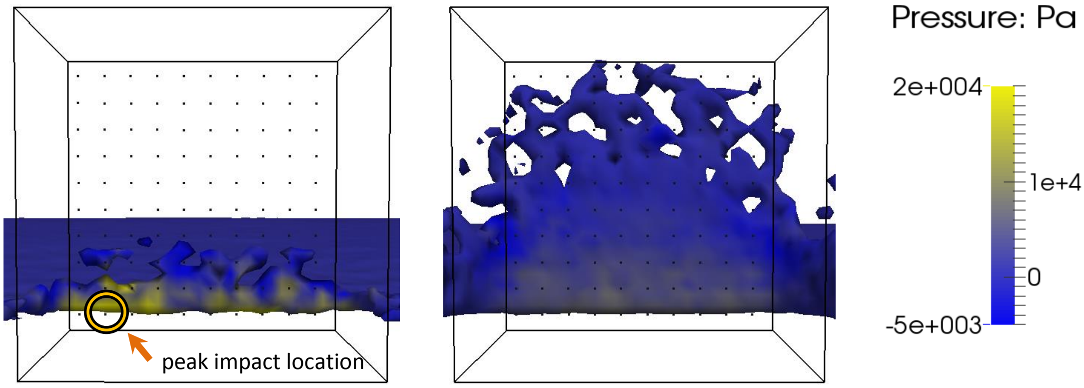

(a) (b)

Figure 5.19 Pressure distribution on vertical surface at $H/h_0 = 0.5$; (a) first impact at t = 4.150 sec, (b) peak impact occurred at the circled probe at t = 4.325 sec.

5.3.4.4 Pressure for structure with orientation θ = 30° and 60°

Figure 5.20 shows two snapshots of the 30° and 60° rotated cube surfaces. The peak pressure on both surfaces occurred at different times as measured by the probes at the lowest row. The 30° surface experienced its first peak impact 0.275 sec or 11 time steps earlier than the 60° surface. This difference is due to the time of arrival of the broken wave front at each surface. From snapshots (a) and (b) in Figure 5.20, it can be seen that the pressure value is very low and the fluid is scattered. The non-dimensionalised peak pressure value ($P/\rho g h_0$) for the 30° and 60° cases are 0.07 and

0.03, respectively. The solitary wave for case H/h_0 = 0.1 was not sufficient to produce a bore on flat onshore surface where the cube structure is situated.

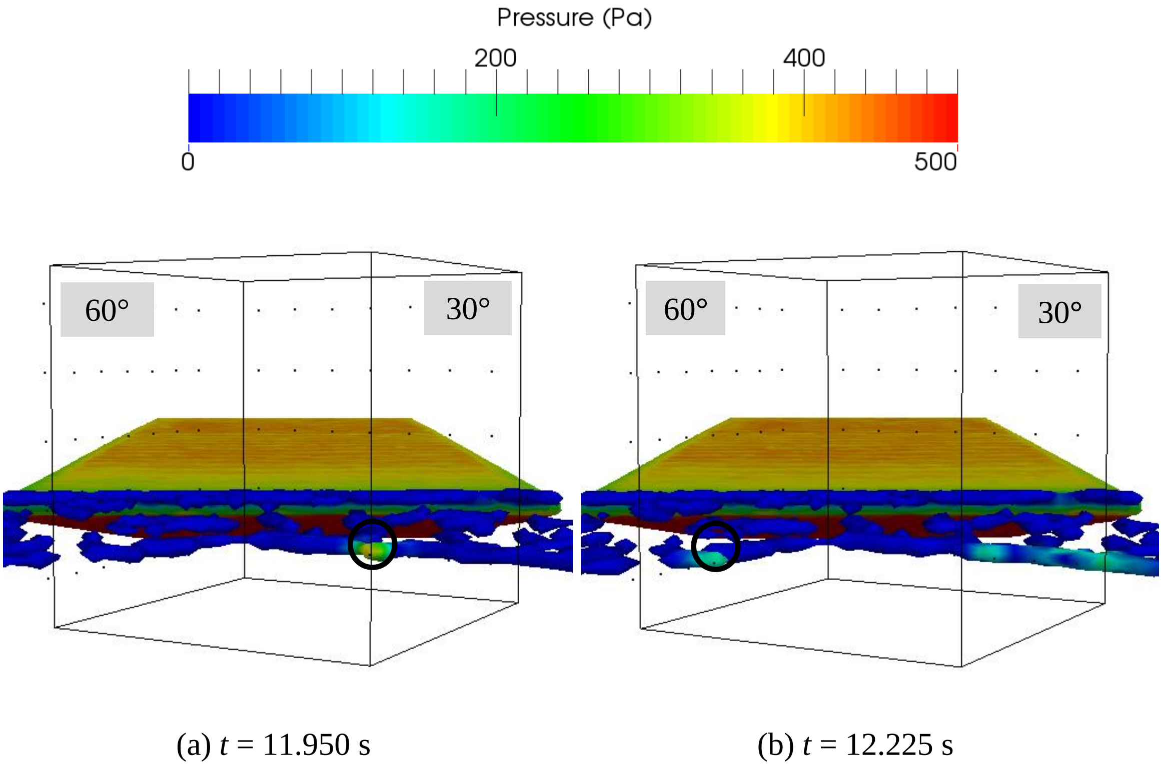

Figure 5.20 Pressure distribution on 30° and 60° surface with H/h_0 = 0.1; (a) peak impact of 30 degree surface at t = 11.950 sec, (b) peak impact of 60 degree surface at t = 12.225 sec.

Four snapshots in *Figure 5.21* show bore impact for case H/h_0 = 0.3; snapshot (a) shows the first bore reached the cube structure at t = 5.325 sec and then followed by the maximum impact pressure on the 60° surface recorded by the nearest pressure probe to the incoming wave, as shown by snapshot (b). At t = 5.350 sec, the peak impact occurred on the 30° surface as depicted by snapshot (c), however this peak value was not measured by the first or nearest probe to the incoming wave but by middle probe at the lowest level. The non-dimensionalised peak impact values ($P/\rho g h_0$) related to (b) and (c) are 0.75 and 1.59, respectively. For case H/h_0 = 0.3, the peak impact on 60° surface is 52 percent less than the 30° surface. The maximum wave runup on the both surface of cube can be seen in snapshot (d), where higher runup occurred at the 30° surface. The difference of maximum wave runup height is about D/5, where D is the height of the cube.

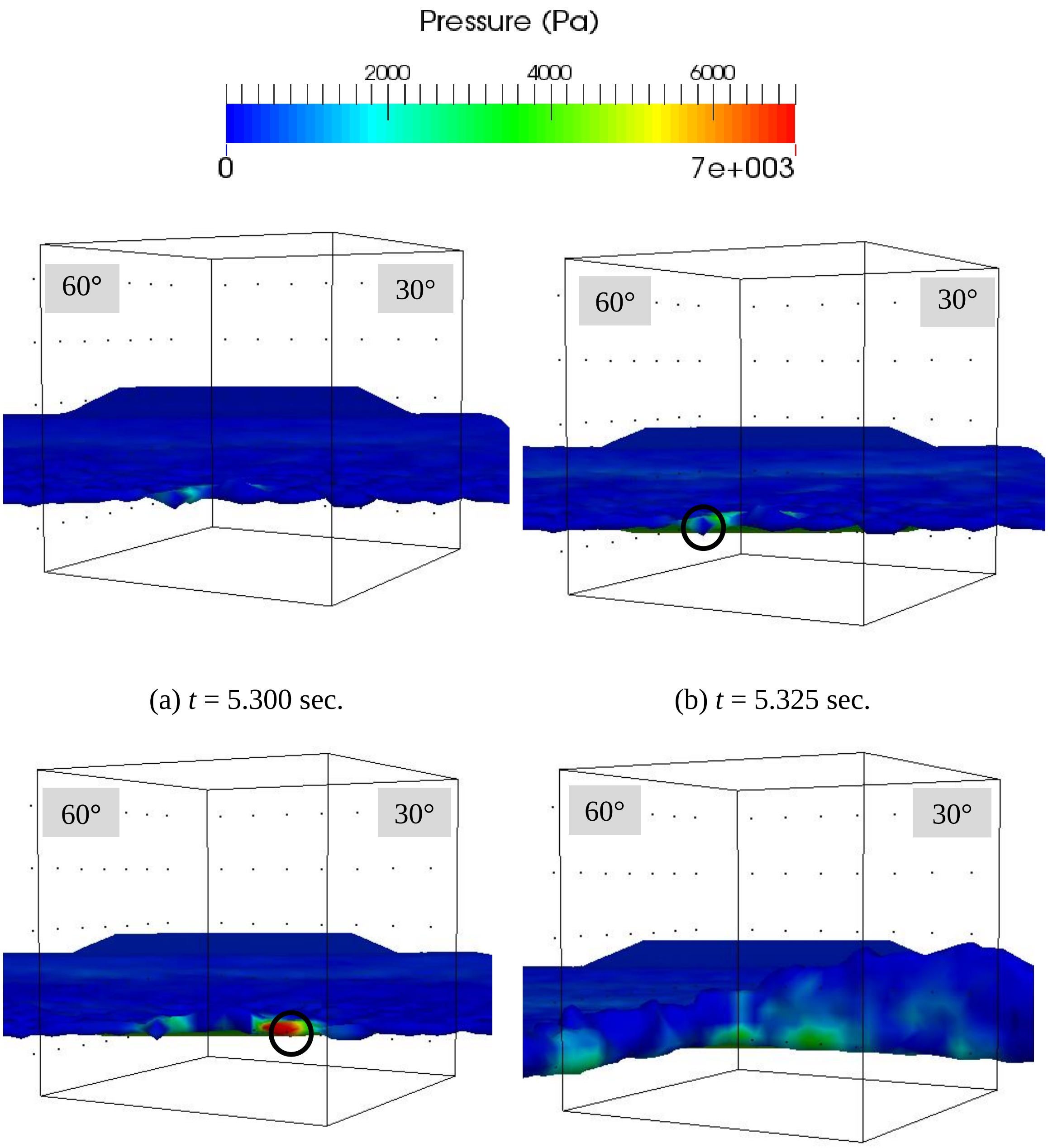

(a) t = 5.300 sec.

(b) t = 5.325 sec.

(c) t = 5.350 sec.

(d) t = 5.625 sec.

Figure 5.21 Pressure distribution on 30° and 60° surface with H/h_0 = 0.3; (a) first impact at t = 5.325 sec, (b) peak impact of 60° surface at t = 5.325 sec, (c) peak impact of 30° surface at t = 5.350 sec and (d) maximum runup at t = 5.625 sec.

Figure 5.22 depicts four snapshots of wave impact on cube at different time occurrences for case H/h_0 = 0.5. Snapshot (a) shows the first impact which is also when the peak impact occurred at t = 4.100 sec on the 30 degree surface where the peak impact point is located at the lowest probe. Snapshot (b) shows the peak impact on the

60° surface. The non-dimensionalised pressure value ($P/\rho g h_0$) of the 30° and 60° surface are 3.25 and 1.46, respectively.

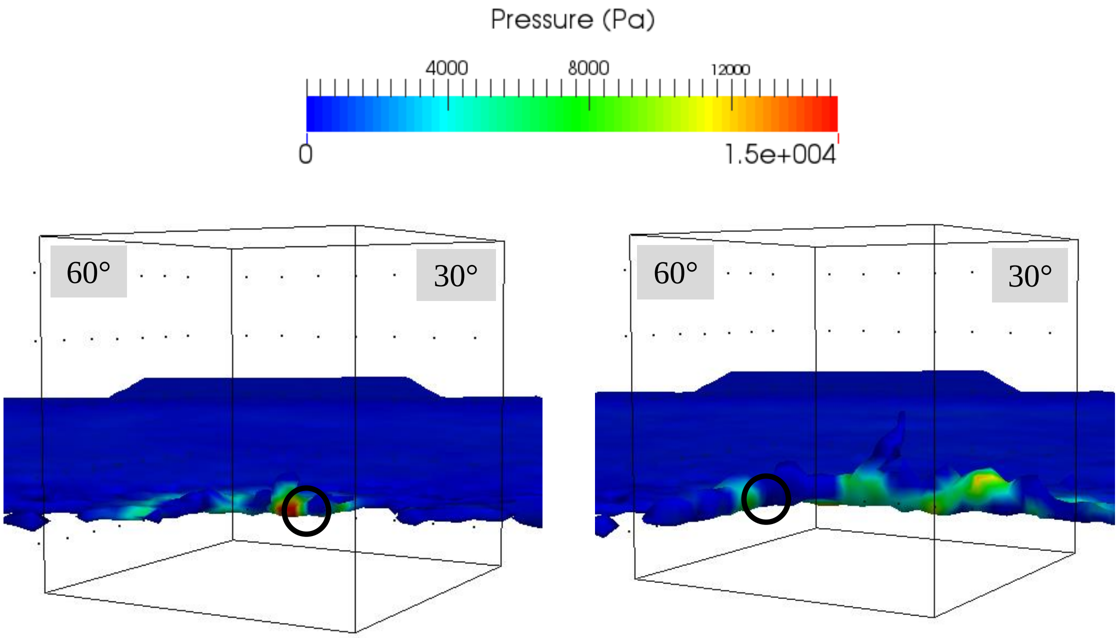

(a) t = 4.100 s

(b) t = 4.150 s

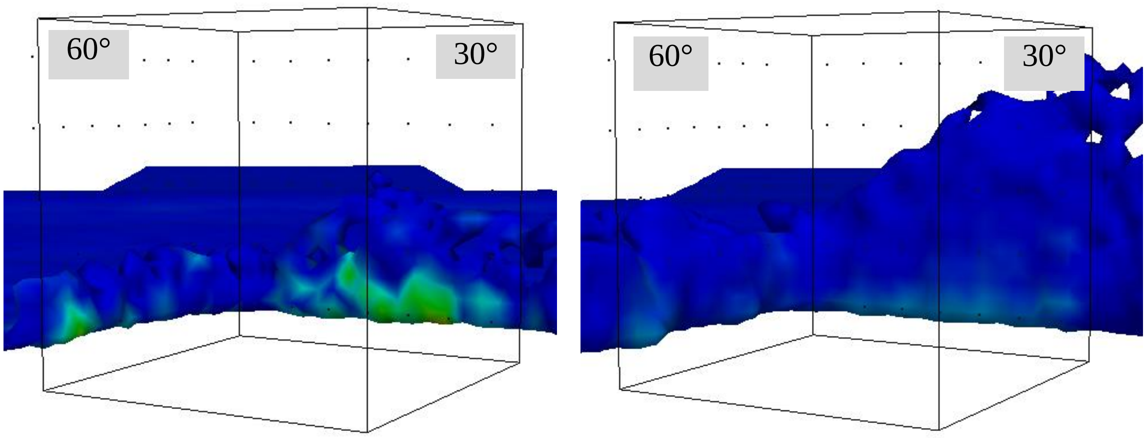

(c) t = 4.225 s

(d) t = 4.525 s

Figure 5.22 Pressure distribution on 30° and 60° surface with H/h_0 = 0.5; (a) first and peak impact of 30° surface at t = 4.100 sec, (b) peak impact of 60° surface at t = 4.150 sec, (c) post peak impact at t = 4.225 sec and (d) maximum runup at t = 4.525 sec.

The difference between the two is 55 percent. Snapshot (c) shows the post peak impact distribution on both the cube front surfaces until the wave runup reaches its maximum height as depicted by snapshot (d). The last two snapshots illustrate the wave runup is higher on the 30° surface than the 60° surface, and this is also consistent with case H/h_0 = 0.3.

By reviewing the location of peak impact in cases H/h_0 = 0.3 and H/h_0 = 0.5, it can be seen that the peak impact did not always occur at the nearest probe to the incoming wave as the case shown by Figure 5.21 and Figure 5.24 (a). The unpredictable peak impact location implies that the maximum impact may occur at any point in a row near the bottom of the face. Hence, to use this numerical result as an input loading for design, it is reasonable to apply a maximum impact value gained from a probe at a point or an area of the same level/height. However, since the peak impact occurs for a very short time duration (0.05 sec), the mean value from all probes in a row/level is used for the applied load-time history for design purposes.

5.3.4.5 Pressure for structure with orientation θ = 45°

Figure 5.23 shows two snapshots of the 45° rotated cube surfaces. Snapshot (a) shows a condition when the fluid initially impacts the structure and snapshot (b) shows the peak impact pressure measured by the third probe at the lowest row. Similar to Figure 5.20, this case with H/h_0 = 0.1 also results in a small pressure on the wall where the non-dimensionalised peak pressure value ($P/\rho g h_0$) is 0.09 and this value is 29 percent higher than the 30° case and almost twice higher than the 60° case.

Figure 5.24 illustrates bore impact for case H/h_0 = 0.3; snapshot (a) shows the first and peak impact that occurred at t = 5.250 sec as measured by the first probes at the lowest row and snapshot (b) shows the post peak condition at t = 5.625 sec when the maximum runup reached 1/3 of the height of the cube. The non-dimensionalised peak impact values ($P/\rho g h_0$) for this case is 0.97 and this value is in between the non-dimensionalised peak impact values for the 30° and 60° surface. It is 38 percent lower than the 30° surface case and 29 percent higher than the 60° surface case.

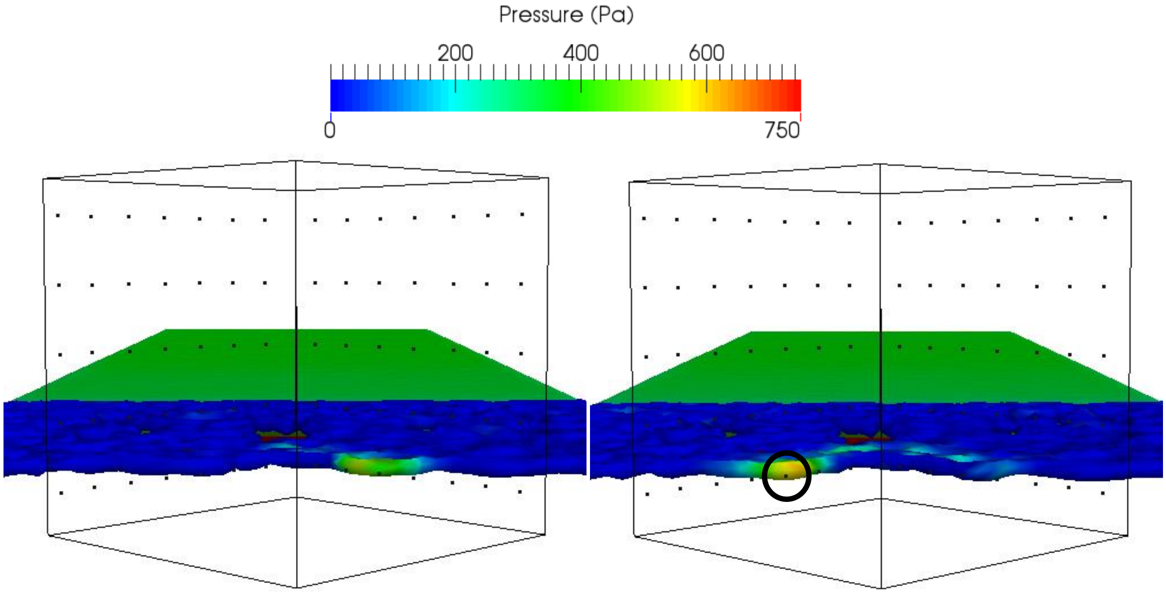

(a) t = 9.450 s (b) t = 9.500 s

Figure 5.23 Pressure distribution on the 45° surface with H/h_0 = 0.1; (a) first impact at t = 9.450 sec, (b) peak impact at t = 9.500 sec.

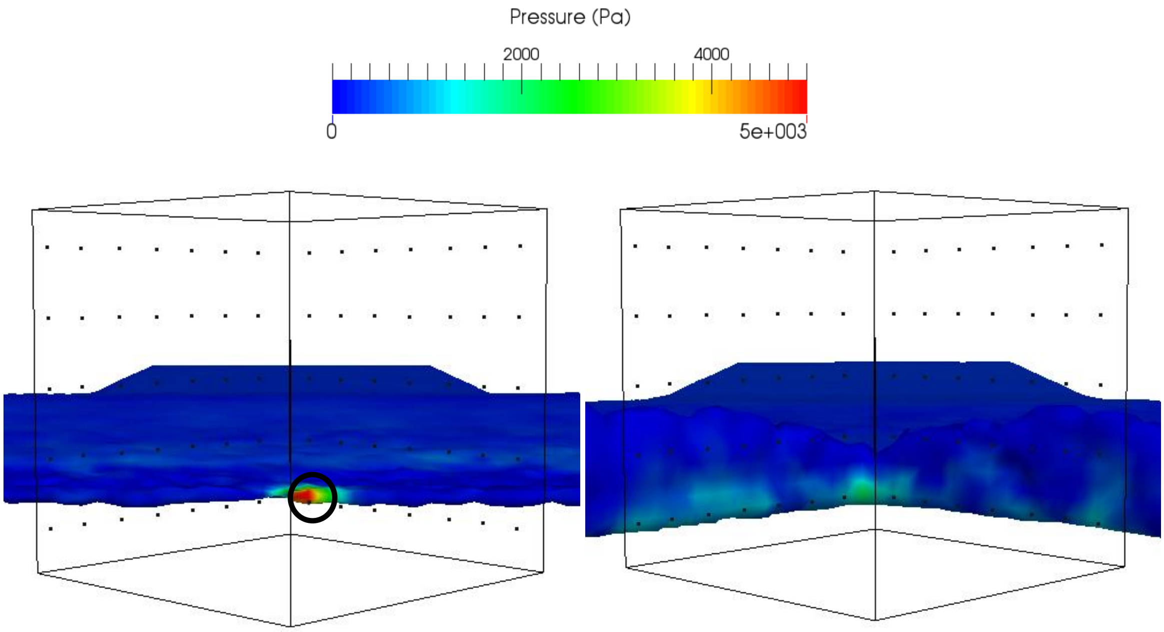

(a) t = 5.250 s (b) t = 5.625 s

Figure 5.24 Pressure distribution on 45° surface with H/h_0 = 0.3; (a) first and peak impact at t = 5.250 sec, (b) post peak impact at t = 5.625 sec.

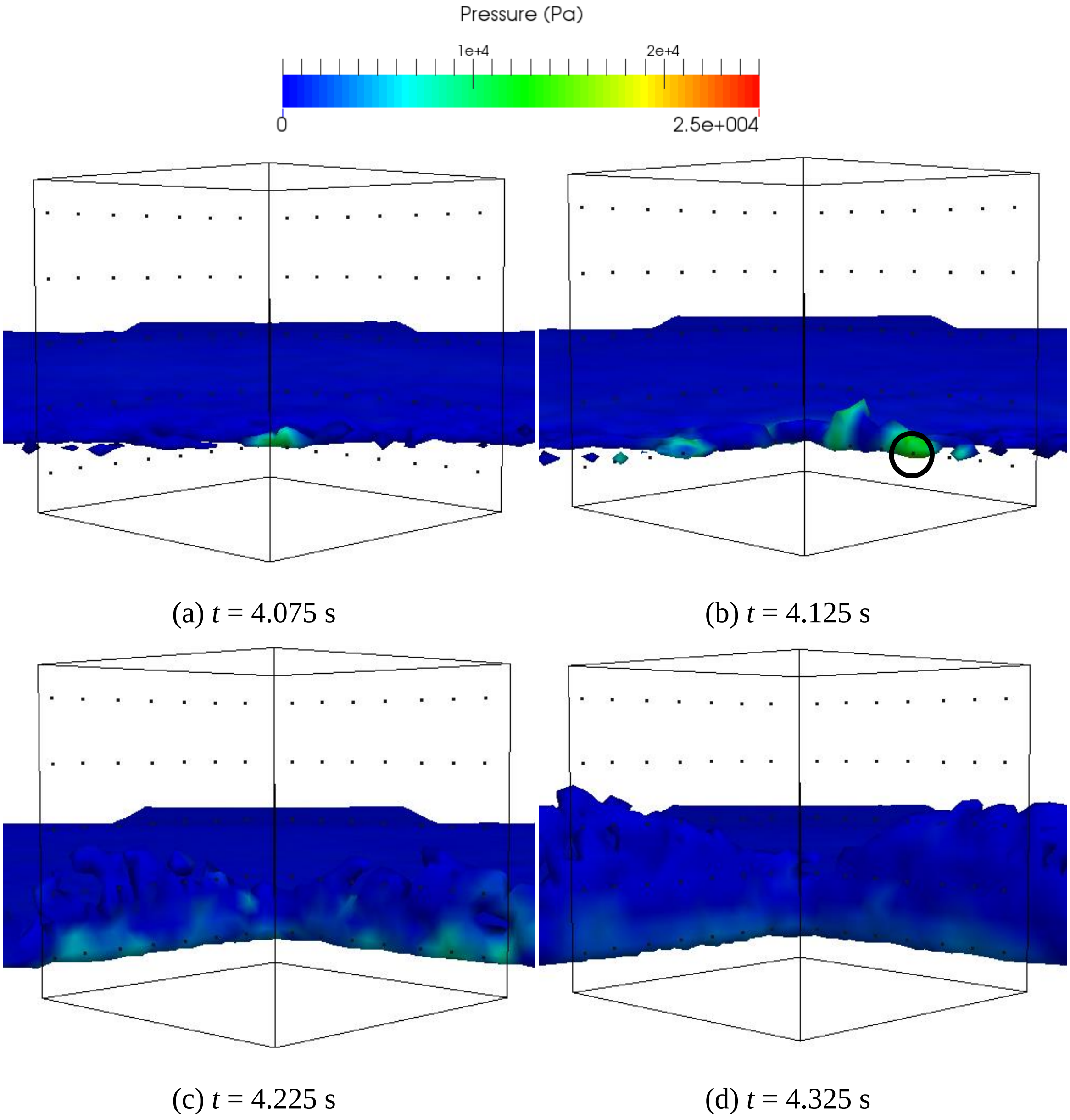

Figure 5.25 Pressure distribution on 45° surface with H/h_0 = 0.5; (a) first impact at t = 4.075 sec, (b) peak impact at t = 4.125 sec, (c) post peak impact at t = 4.225 sec and (d) maximum runup at t = 4.325 sec.

Figure 5.25 shows the pressure distribution for case H/h_0 = 0.5. Snapshot (a) shows the first impact occurred at t = 4.075 sec and then followed by the peak pressure measured by the third probes as can be seen from snapshot (b). The non-dimensionalised peak pressure value ($P/\rho g h_0$) is 3.07 and this value is slightly less (5 percent) than the 30° case but more than double (110 percent) as compare with the 60° case for the same $H/h_{0.}$ Snapshots (c) and (d) show the post peak pressure distribution and the later depicts the maximum runup up to half the height of the cube. From snapshots (c) and (d), it can be seen that the fluid runup on the cube surfaces are almost identical. This may be caused by the DualSPHysics software applying single precision instead of double precision

5.3.5 The force prediction of SPH versus design codes

The tsunami forces prediction from SPH and semi-empirical design equations are compared in this section. The comparison is intended to assess the performance of each design equation when it used to predict the total force on a certain case study where in this case is the tsunami bore impact on a discrete structure that relatively close to the shoreline and sit on the dry onshore bed. It should be noted that each semi-empirical design equation was derived from an experimental (or analytical) study with different boundary conditions and assumptions, so their performance will vary depending on the loading conditions.

The force predictions from Equations (2.6) to (2.10) in Chapter 2 are compared with SPH total forces exerted on the vertical surface of structure. More specifically, the numerical simulations that are being compared are the 0° orientation structure with H/h_0 = 0.3 and H/h_0 = 0.5. The case with H/h_0 = 0.1 is not incorporated since it has insufficient onshore bore height and velocity. The case of 0° orientation structure is considered since this is the basic assumption that is only considered by those equations. For an easier identification, the predicted forces determined by design equations will be named in this section as OSU (Equations (2.6)), Cross (Equations (2.7)), Asakura (Equations (2.8)), Fujima (Equations (2.9)) and OCADI (Equations (2.10)). The predictions of forces from those equations are plotted against SPH model force-time histories as shown in Figure 5.26 and Figure 5.27.

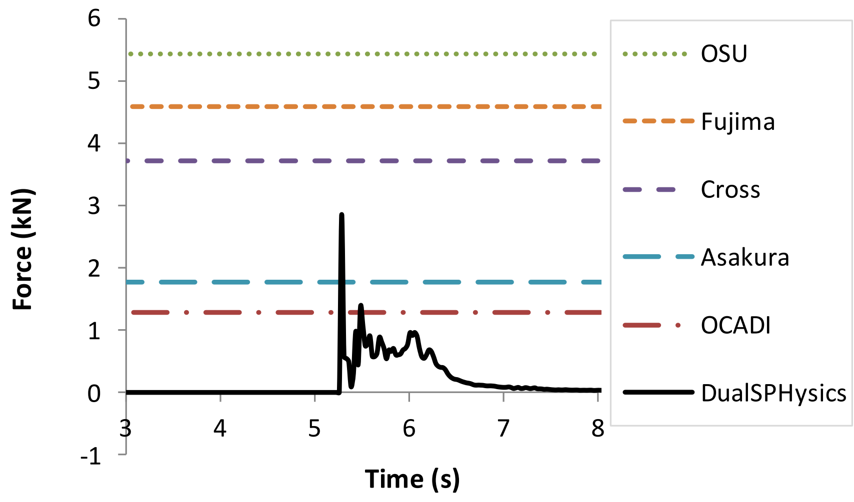

Figure 5.26 SPH vs semi-empirical forces prediction for the case of H/h_0 = 0.3.

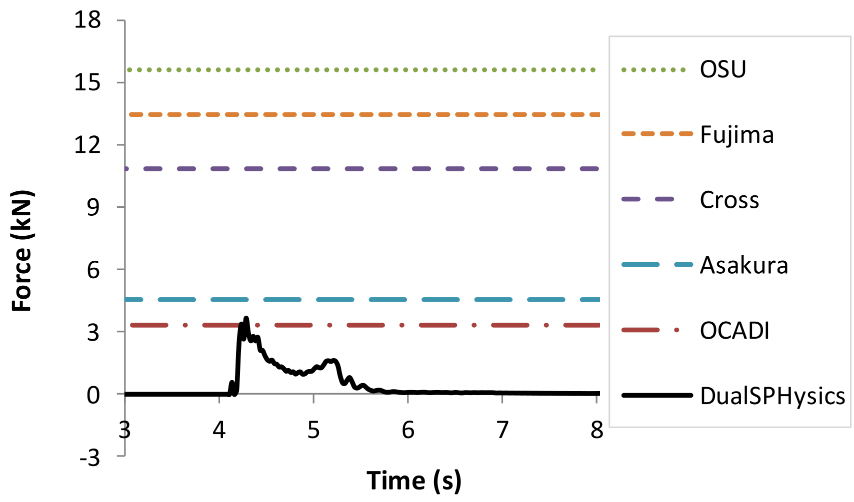

Figure 5.27 SPH vs semi-empirical forces prediction for the case of H/h_0 = 0.5.

In Figure 5.26 for the case study with of H/h_0 = 0.3, the SPH peak force lies in between the peak force prediction of five design equations, but in Figure 5.27 for the case with H/h_0 = 0.5 or higher bore depth, the design equations includes the OSU, Fujima and Asakura over-predict compared to the SPH result significantly. These results are likely to be related to the different experimental and assumptions involved in the derivation of those equations. For example, the OSU equations are derived based on experiments involving non-discrete wall structures that included a thin layer of water in front of the targeted structure (or wet bed condition). On the other hand, the SPH simulation herein utilised a discrete structure with dry bed condition. These difference boundary conditions could have explained the results.

The present comparison results raise the possibility that those design equations are highly sensitive to the change or variation of the values of bore characteristics that are mainly dominated by bore velocity and bore height, by looking at the significant increase in force predictions due to different $H/h_{0.}$ One of the issues that emerge from this finding is the inconsistent force prediction from the existing design codes. For the design purposes, the large discrepancy shown by existing equations can give cause to engineers to question the safety of structure designed to withstand future tsunamis. The discrepancy of force prediction between those design equations suggest that significantly more study in this research areas is needed. The SPH force predictions above could be improved by the use of a higher resolution simulation or multi-phase model. It can thus be suggested that the improvement in the SPH modelling is also needed in this research area.

5.4 Tsunami wave impact on a discrete cylindrical structure in 3-D

To demonstrate the suitability of SPH modelling of tsunami wave forces on discrete, non-orthogonal structures, the experimental data published by Zhang (2009) were used for comparison with a 3-D SPH analysis. In the experimental model, a vertical cylinder with a diameter of 1.22 m and height of 1 m was placed in a large-scale multidirectional wave basin with the following dimensions (Figure 5.28): 48.8 m long, 26.5 m wide and 2.1 m deep. In the numerical model, a reduced size of wave basin was adopted with the following dimensions; 16 m long, 10 m wide and 2.5 m deep. The wave-maker motion in recent research is based on Goring's method (Goring, 1978). The maximum paddle stroke is 1.11 m and reaches its maximum displacement within 2.5 s. The water depth in this case is d = 0.6 m and the ratio of the targeted wave height (H) to the still-water level, H/h_0, is 0.6. The smaller size of tank, compared with the experimental, was used in order to reduce the number of particles involved in the simulation. In this model, more than six million water particles were involved, using a particle size of 0.02 m and 0.6 m height of water along the water tank. The arrangement of probes for measuring surface elevation and velocity can be seen in Figure 5.28 and includes six pressure probes mounted on the surface of the cylindrical structure divided into two layers.

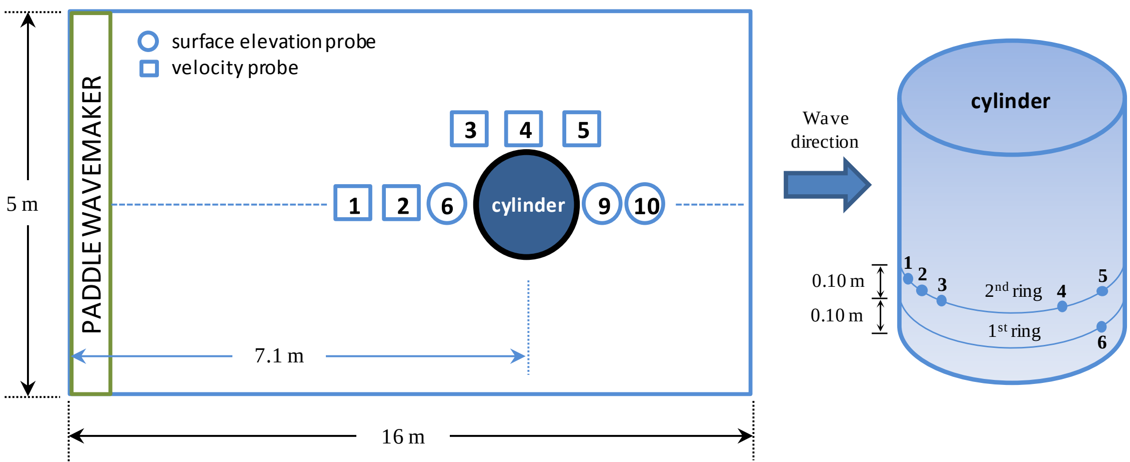

Figure 5.28 Wave flume layout and instrumentation locations.

5.4.1 Modelling results

In the physical experiment, pressure probes were arranged as shown in Figure 5.28, these probes were flush mounted around the cylinder and arranged in four rings at different layers. Figure 5.29 shows snapshots from the SPH model detailing the propagation of the wave. Figure 5.30 details the comparative results for wave surface elevation. At probes WG6 the numerical model prediction is 0.39 m, which underestimates the measured water surface elevation by 9.3%. At probes WG9, the numerical model prediction is very similar to the measured data. At WG10 about 1.8 m behind the cylinder, the numerical prediction of surface elevation is 0.4 m, which is 25% higher than the experimental measured value. Figure 5.31 illustrates the comparative results for dynamic pressure; in general the numerical model predictions overestimate the experimentally measured data by a greater or lesser degree. The significant difference mainly occurred at the first three probes (probes 1, 2 and 3) close to the incoming waves. The differences between numerical prediction and measured data for the respective probes 1, 2 and 3 are 22.2%, 28.6% and 26%. The numerical model predictions at the three probes on the other side of the cylinder do not differ significantly.

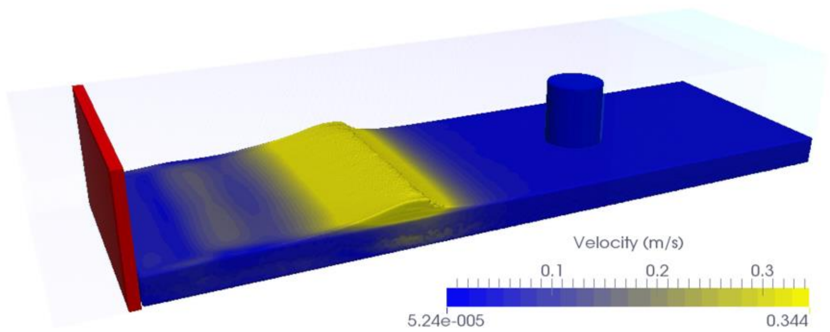

Figure 5.29 (a) Snapshot at t = 9.75 s

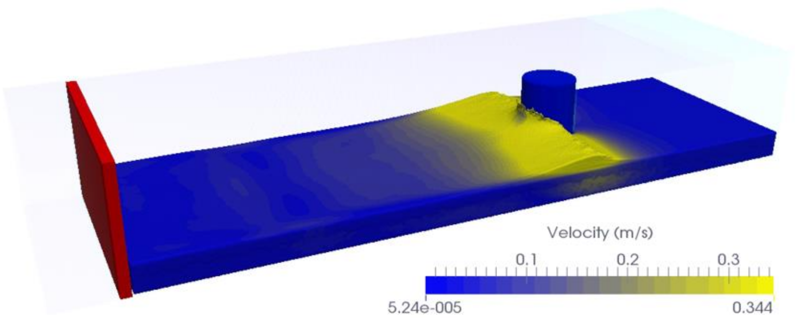

Figure 5.29 (b) Snapshot at t = 11.5 s

Figure 5.29 Simulation of DualSPHysics model: (a) wave propagation, (b) wave impacting cylinder

In contrast to the pressure prediction, the velocity prediction from the numerical modelling underestimated the measured velocity at all five probes (see Figure 5.32). The difference between numerical prediction and measured data is between 15.2% and 22%. The largest difference occurred at ADV3 and ADV5. Hence, although the simulation of such circular cylinder is not investigated further, SPH can produce results in satisfactory agreement with experimental data for differently shaped cylinders.

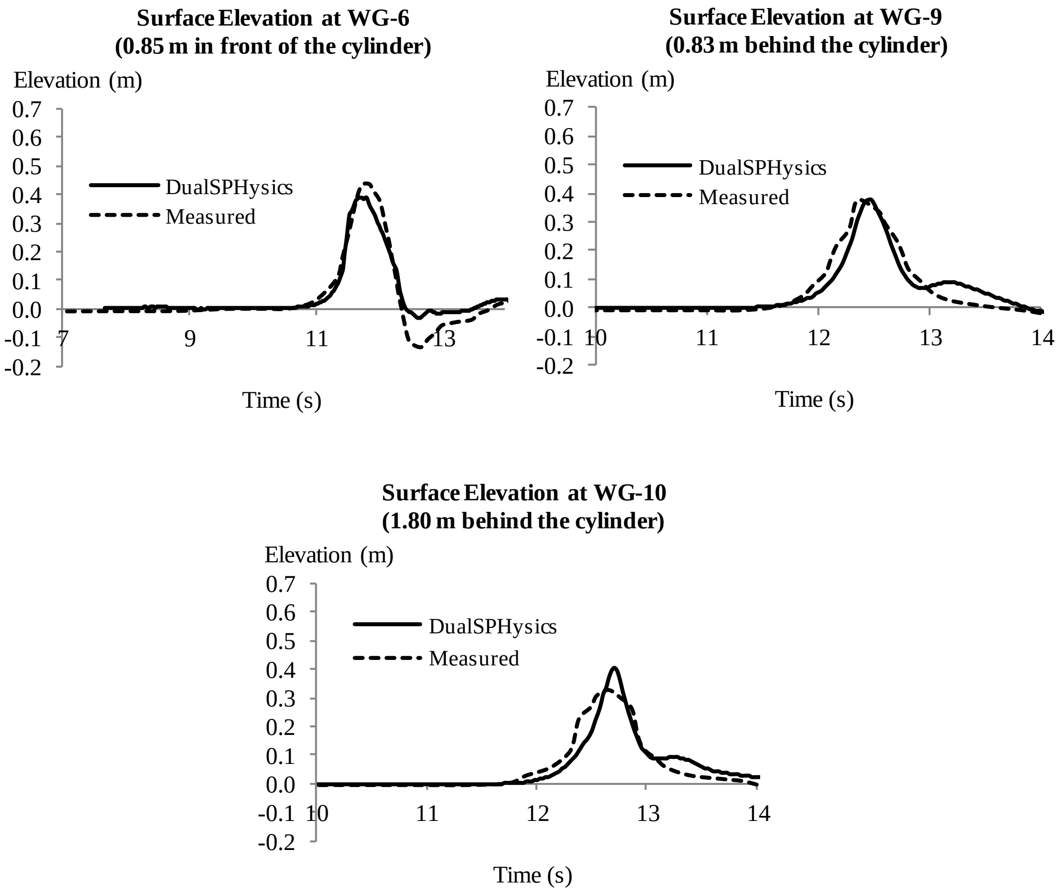

Figure 5.30 The comparison of water surface elevation

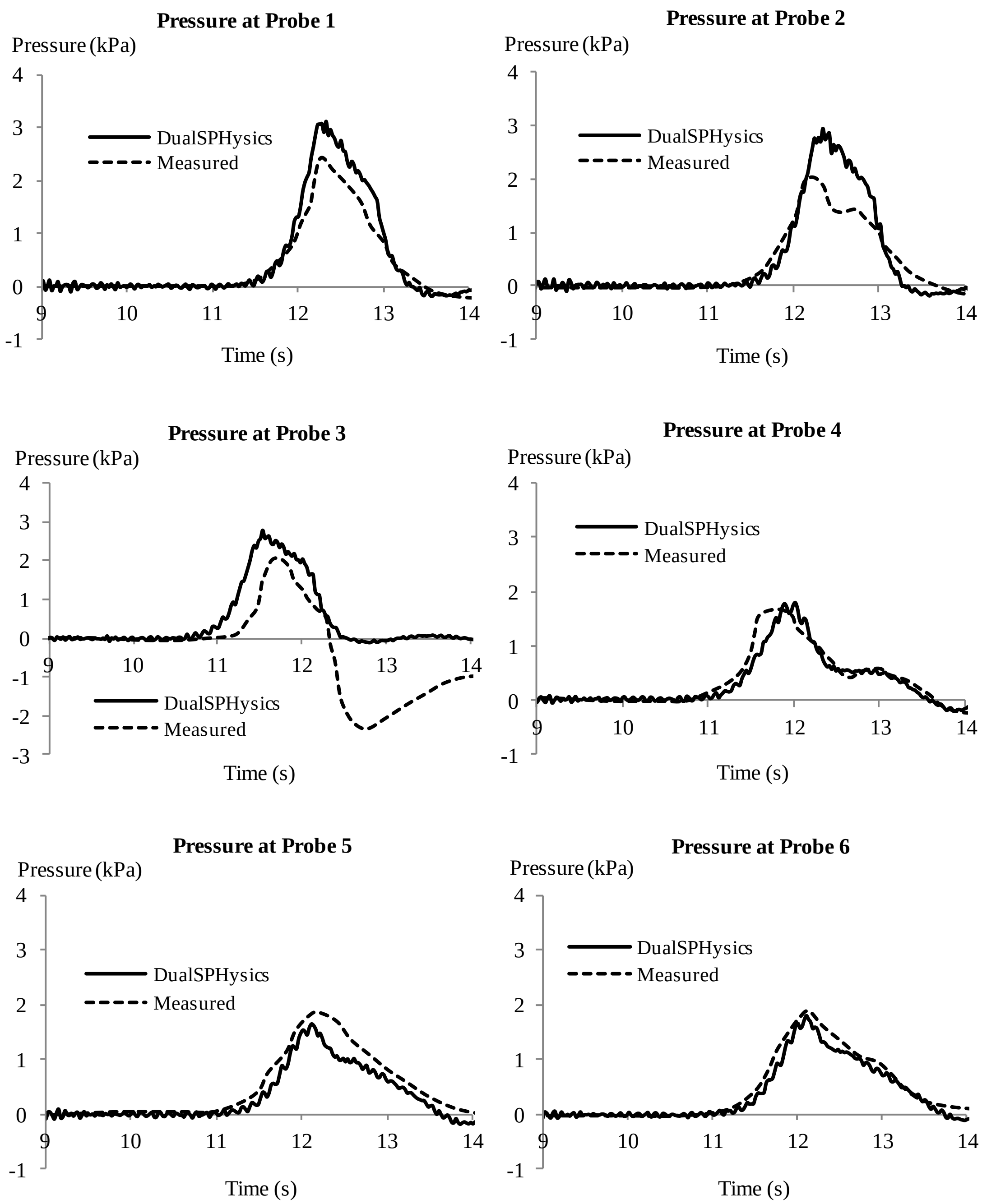

Figure 5.31 The comparison of dynamic pressure for selected gauges for plane solitary waves

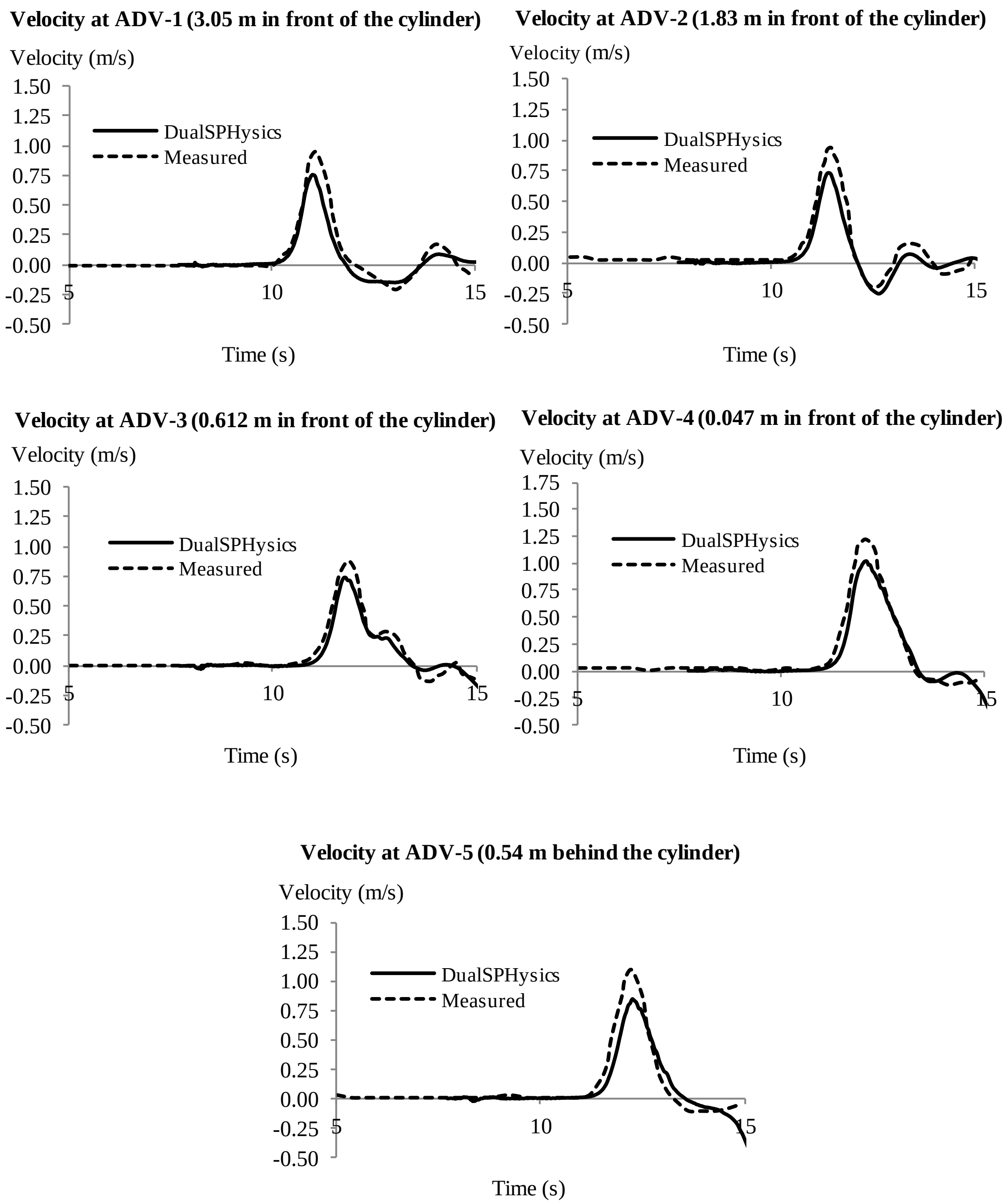

Figure 5.32 The comparison of wave velocity

5.5 Tsunami bore impact on multiple discrete structures in 3-D

The 3-D SPH modelling in this section was performed to study the effects of shielding and flow focussing of tsunami bore to the coastal onshore structures. As described in Chapter 2, these effects caused serious damages to multi-storey buildings made of concrete and steel and it could be worsened if the impacted building structures were made of lighter weight materials such as timber. In this section the numerical simulations examine the shielding and flow focusing effects on multiple structures at different angle of rotations as an idealisation of a low-rise timber houses. The multiple structures in this section consist of three cubes, with two structures located at the front and one structure at the rear. Both front structures provide a shielding to the rear structure and at the same time the gap between two front structures can generate a flow focusing effects to the rear structure.

5.5.1 Structures with 0° orientation

The plan view of the boundary model for simulating shielding and flow focusing effects on structures can be seen in Figure 5.33. Three structures named A, B and C were situated at the onshore part, with A and B acting as the front structures closer to the shoreline while C is the rear structure. The distances in the domain are expressed in the multiple of D which is equal to 1 m. The centre-to-centre distance between A and B (d_{AB}) is $2D$, similar to the centre-to-centre distance between front and rear structures. The depth of still water h_0 is 1 m and the paddle wavemaker motion was designed to create a solitary wave with maximum height to be equal to H/h_0 = 0.5. Several probes were set up to measure the characteristics of the solitary waves and the following bores. The offshore water surface elevations were measured by probes at the centreline of the water tank. Pressure probes were located on the surroundings of structures A, B and C, and also along the inner sides of the onshore boundary wall. The velocity and water surface elevation probes were arranged in 5 lines to measure the onshore bore flow characteristics.

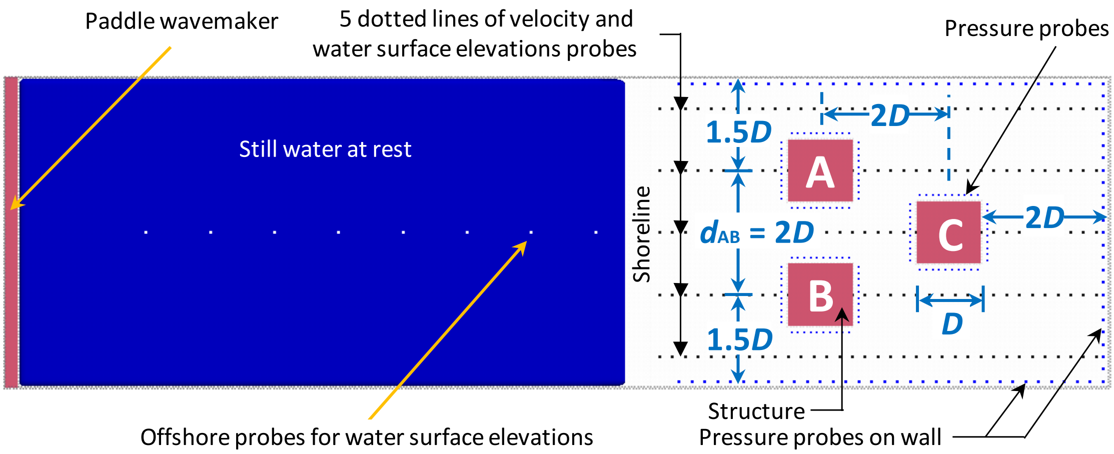

Figure 5.33 Plan view of a group of structures with 0° orientations

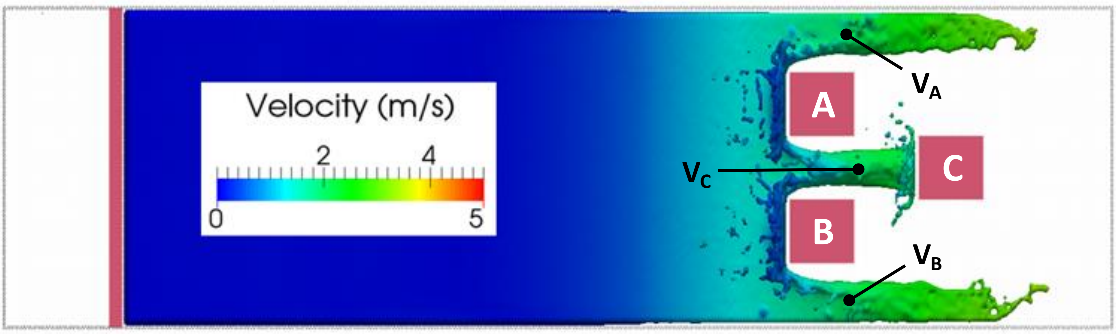

Figure 5.34 Numerical simulation of wave impacts on a group of structures with 0° orientation (d_{AB} = 2D) at t = 4.68 s.

A plan-view snapshot of an SPH simulation on multiple structures with 0° orientation can be seen in Figure 5.34 showing the bore impacting structures A, B and C with particles coloured according to velocity at t = 4.68 s. Of interest in this simulation are the pressures exerted on the surface of structures, where the pressures are provided in terms of normalised total pressure ($P/\rho g h_0$). The normalised total pressure for the simulation shown by Figure 5.34 can be seen in Figure 5.35. Figure 5.35(a) shows that total pressure on both front structures A and B are not the same even though located at the same distance from the shoreline. Two peak pressures in Figure 5.35(a) caused by the splashing water of first impact hit the pressure probes for the second time. Figure 5.35(b) indicates that the rear structure C experience higher impact pressures caused by flow focusing effects and this can be clarified by the comparison of the total pressure in the case of the absence of A and B (or C only) that shows lower total pressure. Significant negative pressure is also depicted in Figure 5.35(b) with magnitude almost 50% higher than its positive pressure. The negative pressure also occurred at the case for structure C (C only) in the absence of A and B but with much lower magnitude.

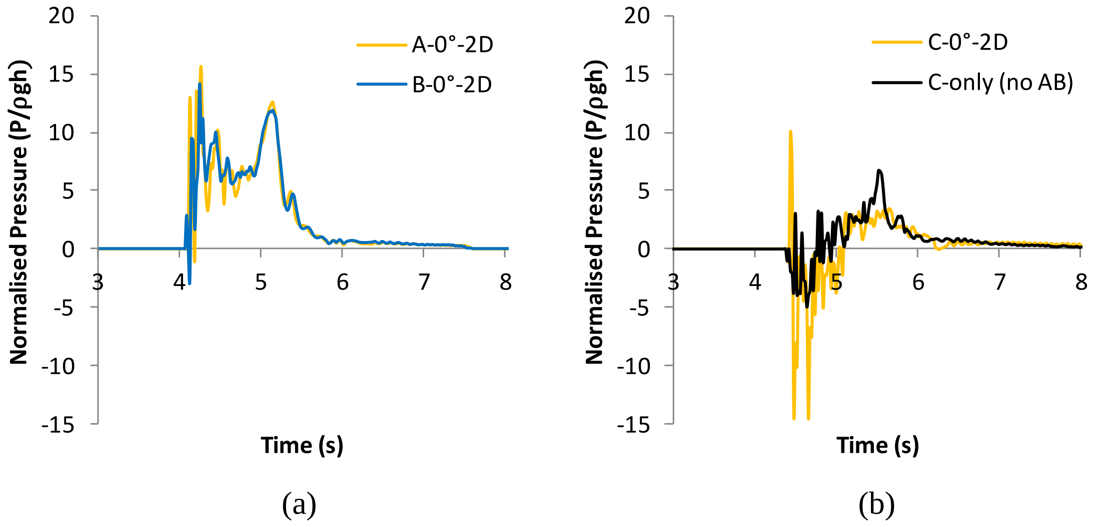

Figure 5.35 Total pressure on the front surface of structures A, B and C (associated with Figure 5.33) for A-B separation distance of $d_{AB} = 2D$.

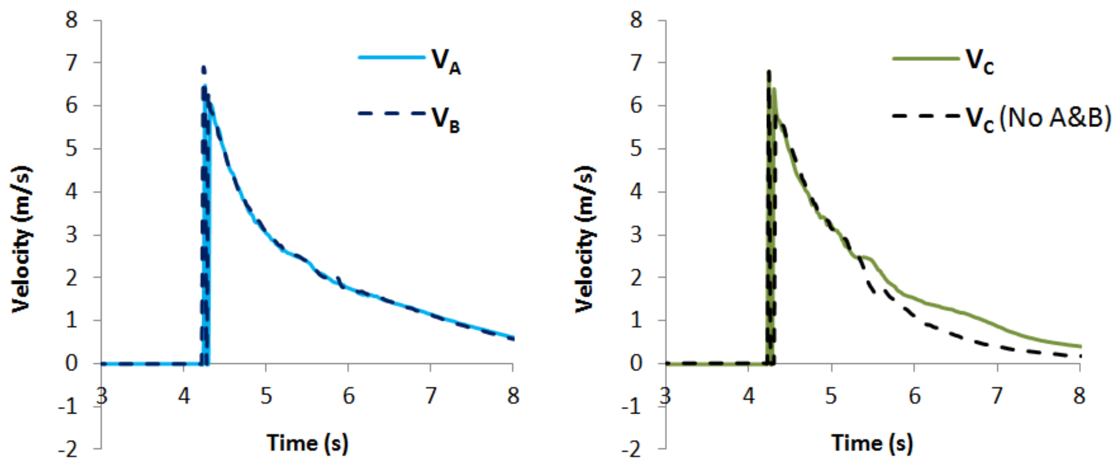

Figure 5.36 Bore velocity at V_A, V_B and V_C (see Figure 5.34) at height of 0.1 m

The bore velocity in the simulation was examined in 3 locations denoted by V_A, V_B and V_C in Figure 5.34. Figure 5.36 shows the velocity of bore measured by probes at height 0.1 m from the onshore bed and it can be seen that there is no significant difference. However, measurement by probe at height 0.2 m above the onshore bed shows significant differences as shown by Figure 5.37, especially for V_C, and this can explain a higher total pressure exerted on the surface of structure C. The total pressure of bore is the function of bore velocity and bore height, and higher total pressure is clearly caused by the flow focusing effect.

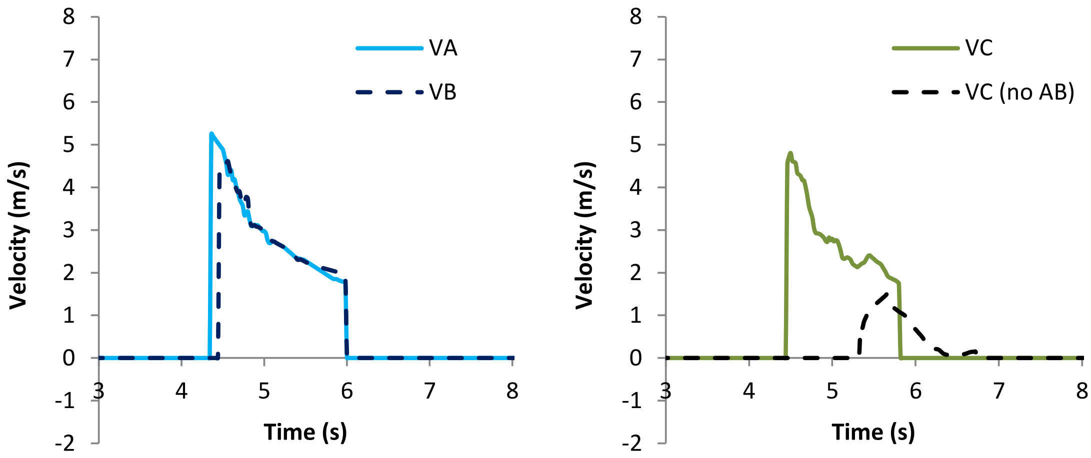

Figure 5.37 Bore velocity at V_A, V_B and V_C (see Figure 5.34) at height of 0.2 m

5.5.2 Structures with 30° orientation

In this section, the shielding and flow focusing effects are simulated on multiple structures with orientation. The orientation of 30° had been chosen since by a single rotation two different vertical surfaces are obtained (the 30° and 60°). The plan view of 30° oriented multiple structures with d_{AB} = 2D is illustrated in Figure 5.38 where the centres of each cube structure have the same separation as for θ = 0° in Figure 5.33. The simulation is shown in Figure 5.39. The velocity of the impacting flows on C is less than for θ = 0°. To investigate the focusing effect, the gap between two adjacent front structures A and B was increased to become 3D as represented by Figure 5.40 and a snapshot of the simulation is provided in Figure 5.41. The comparison of the total normalised pressure can then be made for the case with d_{AB} = 2D and d_{AB} = 3D.

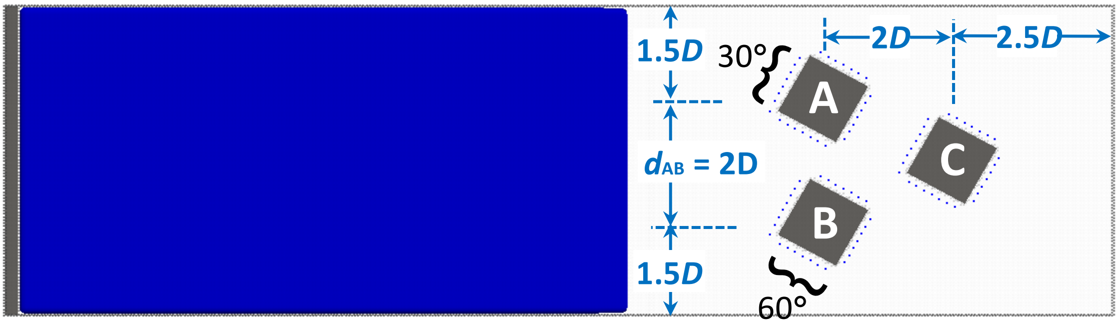

Figure 5.38 Plan view of a group of structures with 30° and 60° orientations (d_{AB} = 2D)

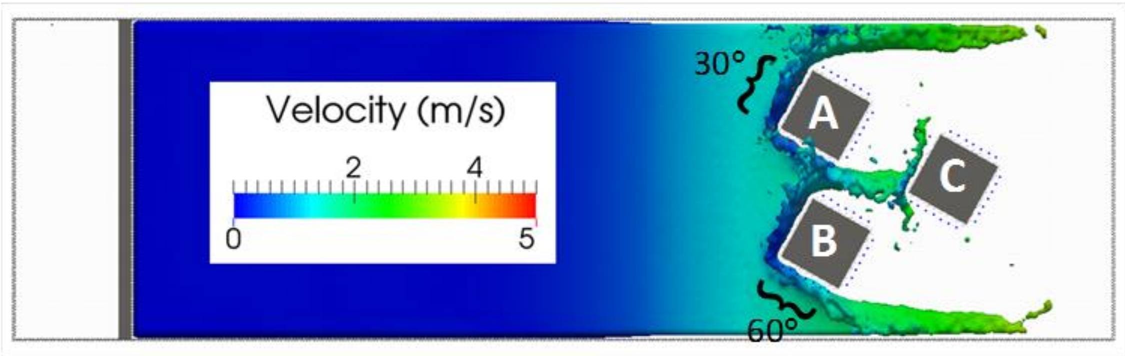

Figure 5.39 Numerical simulation of wave impacts on a group of structures with 30° and 60° orientations (d_{AB} = 2D) at t = 4.68 s.

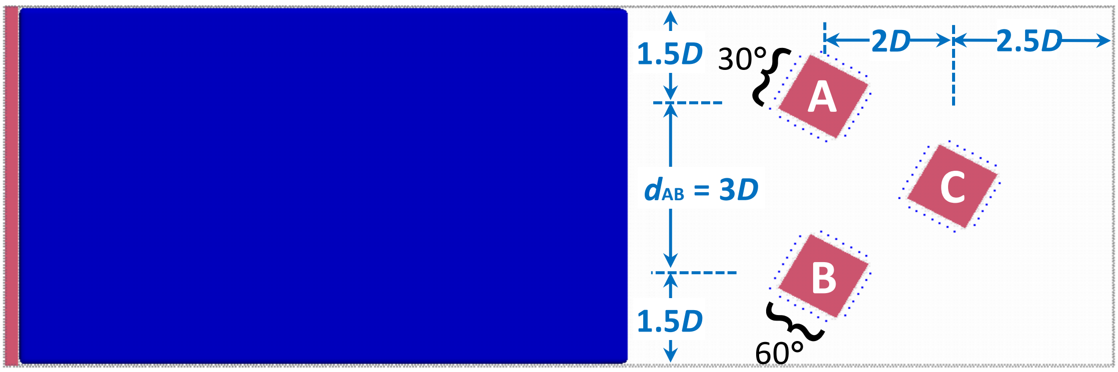

Figure 5.40 Plan view of a group of structures with 30° and 60° orientations (d_{AB} = 3D)

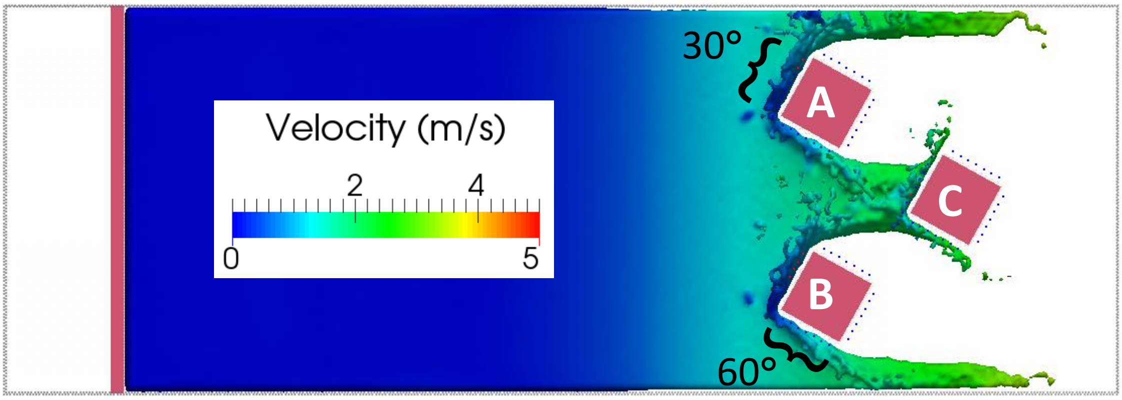

Figure 5.41 Numerical simulation of wave impacts on a group of structures with 30° and 60° orientations (d_{AB} = 3D) at t = 4.68 s.

The total forces exerted on structure A are given in Figure 5.42 where it can be seen that the 30° vertical surface of structure A experienced higher pressure than its 60° surface. This is consistent with the results of section 5.3.4.4 because the projected area of the 30° surface to the oncoming bore is higher than the 60°.

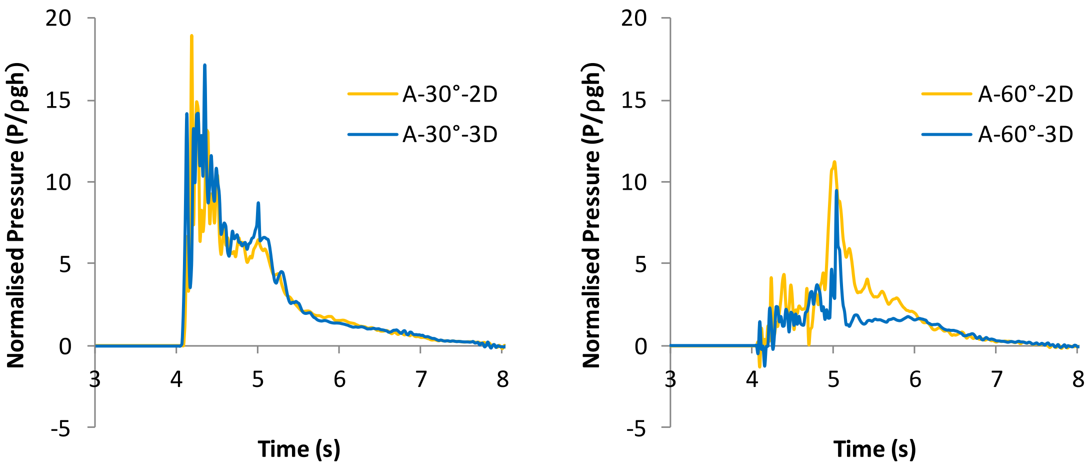

Figure 5.42 Total force on the surface of structures A. Each curve represents a different separation distance between structures A and B.

Figure 5.42 also indicates that narrower water tank caused higher total pressure because in the narrower channel the water has a greater velocity. For structure B, very similar pressures as structure A were measured especially for the 30° surface as shown in Figure 5.43. However, Figure 5.43 shows that the 60° surface of structure B exhibit low pressure compared with the same surface of structure A in Figure 5.42. This is probably due to the proximity of the wall.

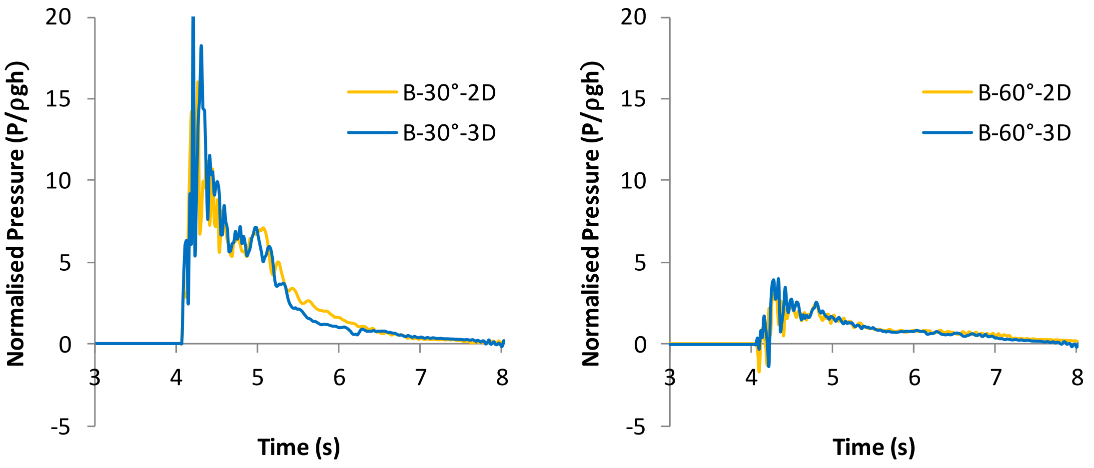

Figure 5.43 Total force on the surface of structures B. Each curve represents a different separation distance between structures A and B

The influence of the increment of gap d_{AB} can be seen in Figure 5.44, where the 30° surface of structure C with $d_{AB} = 3D$ experienced total pressure more than double, compared with the case with $d_{AB} = 2D$. Interestingly, significant differences occur when the 30° surface of structure C compared with its 60° surface regarding total pressure exerted on its surfaces. Since the 30° surface of structure C experiences significant pressure, the comparison can then be made for the case of structure C with and without flow focusing effects (without structure A and B). The results can be seen in Figure 5.45, where structure C with $d_{AB} = 2D$ experiences lower pressures than structure C alone. On the other hand, structure C with $d_{AB} = 3D$ undergoes higher pressure than the structure C alone. This results indicate that a certain gap size (d_{AB}) is required to make the flow focusing effects occured.

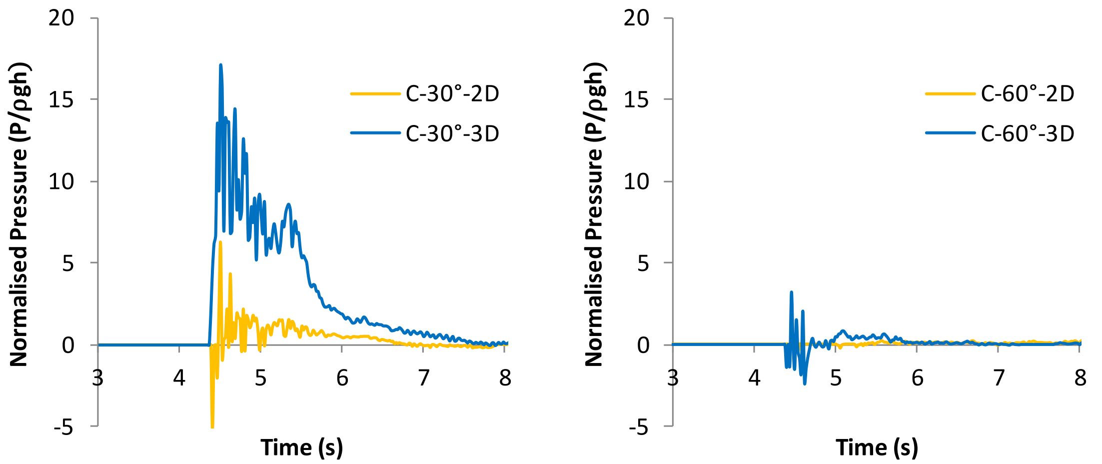

Figure 5.44 Total force on the surface of structures C. Each curve represents a different separation distance between structures A and B

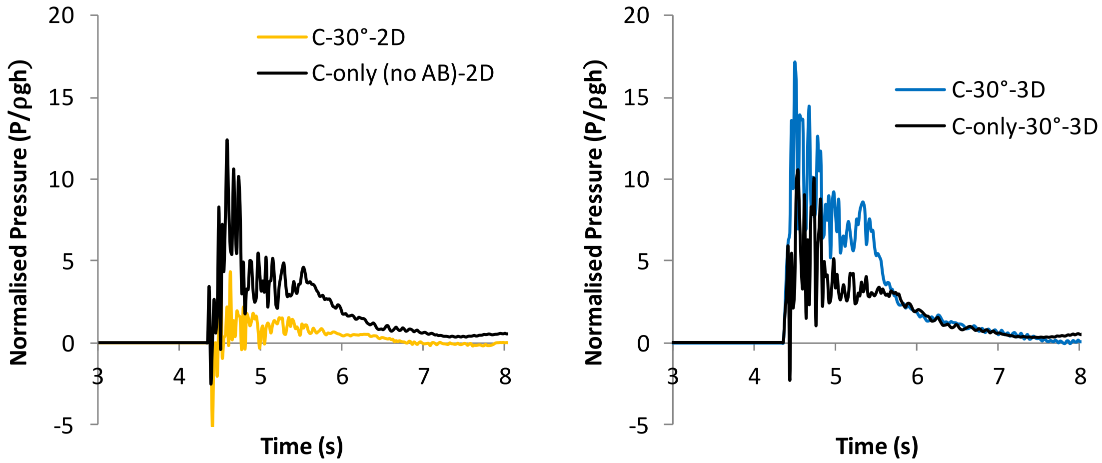

Figure 5.45 Total force on the 30° surface of structures C (with AB and without AB)

5.6 Concluding Remarks

The hydrodynamic modelling using SPH-based software DualSPHysics has been used to investigate the simulation of tsunami-induced waves/bore impacting structures including a vertical wall, idealised cube structures, a half-submerged cylindrical structure and multiple structures. By using SPH the simulations of wave-structure interaction can be performed and the resulting wave impact characteristics such as pressure, wave velocity and water surface elevation can be assessed in great detail. The results show that changing the orientation of the structure to the oncoming tsunami bore can reduce the pressure and force. This knowledge can then be used to inform the simulation and use of shielding for multiple structures. The output from the SPH simulations in this chapter will be used as an input for the finite element modelling to obtain the structural response of the structure.

Chapter 6

Structural Response Modelling using ABAQUS

6.1 Introduction

This chapter presents the finite element model for the general behaviour of a timber structure under tsunami load impact and finishes with recommendations for improving resilience of coastal structures due to tsunamis. Two models of timber structures are described. The first model (Model 1) is a timber structure that represents a vertical wall, typical of the low-rise residential houses damaged by tsunamis (Como and Mahmoud, 2013). This timber wall is based on experimental work by Linton *et al*. (2013). The second model (Model 2) is an idealised rectangular building that is representative of the type of timber houses situated in tsunami prone areas. Both Model 1 and Model 2 were analysed using ABAQUS version 6.10. The modelling process and results for Model 1 and Model 2 are described in the following sections.

6.2 Timber wall model (Model 1)

The prototype timber wall from experiments by Linton *et al*. (2013) was used as the model because of the following characteristics:

1. The wall structure was made of timber since this was the material used in the most vulnerable and frequent of the residential structures identified from tsunami events. The timber wall was designed following an international standard (International Code Council, 2009).

2. The timber wall in the experiment was built at full scale avoiding simplification related to scaling issues.

3. The wall was instrumented with three pressure transducers installed at different heights and two linear variable differential transducers (LVDTs) located at the middle top and middle bottom of the wall to measure the deflections of the wall at critical locations.

4. Testing was conducted in a large flume with a dry reef in front of the wall. The dry condition of the reef simulates a real onshore condition occurring in past tsunami events.

These characteristics ensure that data obtained from the experiment will provide a suitable level of detail to allow adequate comparison with numerical modelling results.

6.2.1 Model set up and properties

The timber wall structure (Model 1) has dimensions of 3.58 m long and 2.44 m high. The structure consists of vertically arranged members known as studs in addition to horizontal double end studs and is covered with plywood on the front side (see Figure 6.1). The vertical stud dimension is 38 x 140 mm which is spaced at 420 mm centres. The horizontal stud has the same size as a vertical stud. Double studs were used at the top and side end of the structure. The structural plywood thickness is 13 mm and screw fixed to the studs. The timber was classified as Douglas Fir kiln-dried No.2 in accordance with the International Residential Code (International Code Council, 2009). The material properties for the studs include Young's modulus of elasticity, E_{stud} = $7.0\mathrm{x}10^9$ N/m^2, Poisson's ratio = 0.22, and density = 530 kg/m^3. The material properties for the plywood are as follows: properties: Young's modulus of elasticity, E_{plywood} = $7.7\mathrm{x}10^9$ N/m^2, Poisson's ratio = 0.22 and density = 750 kg/m^3.

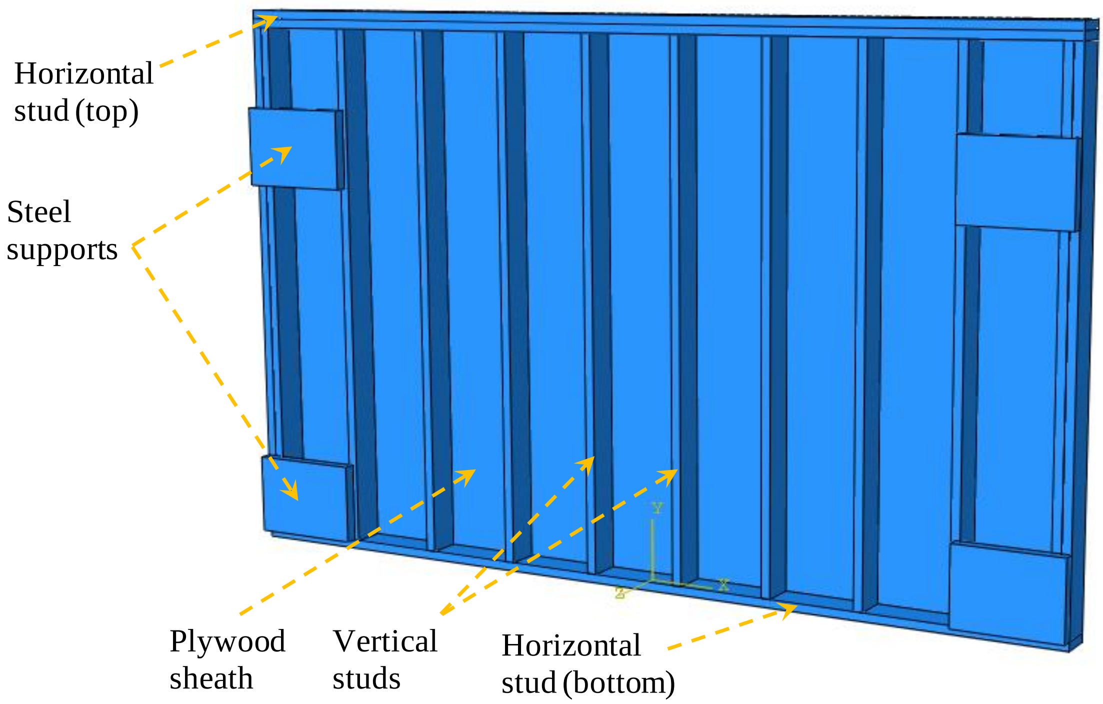

Figure 6.1 The arrangement of Model 1 (from the back “landward” side).

The support of the timber structure was formed via a fixed support represented by a total of four steel plates at both sides of the timber structure (see Figure 6.1). These plates were fully fixed to the flume side wall and were also utilised as the location of the load cells. The timber wall was free along the bottom plate, i.e. the wall is effectively spanning horizontally between the side walls of the flume, which is an uncommon scenario in standard building construction. This was intended to control the mode of failure which was bending failure of the bottom part of the wall. In the finite element (FE) model, the bottom part of timber wall also modelled unsupported.

6.2.2 Applied load and finite element analysis

In the experiment conducted by Linton *et al*. (2013), the timber structure is loaded by the impact of tsunami-like bore following the breaking of a solitary wave propagating along the water tank. In the FE model, the wave load is applied spatially and temporally using the data collected from the pressure probes in the SPH model. The pressures from the 2-D SPH model were applied for the 3-D timber wall by assuming Model 1 as a non-discrete structure; therefore the load was applied uniformly along the width of structure. The numerical pressure-time histories applied on the front surface of the timber structure are illustrated in Figure 6.2. The pressure-time histories shown by Figure 6.2 are the pressures acting on 24 different layers where each layer is associated with numerical pressure probes in the SPH model. The pressure-time history is denoted by L_p. Those pressure-time histories are divided into 4 figures for clarity. The same pressure scale used for Figure 6.2(a) and (b), also for Figure 6.2(c) and (d).

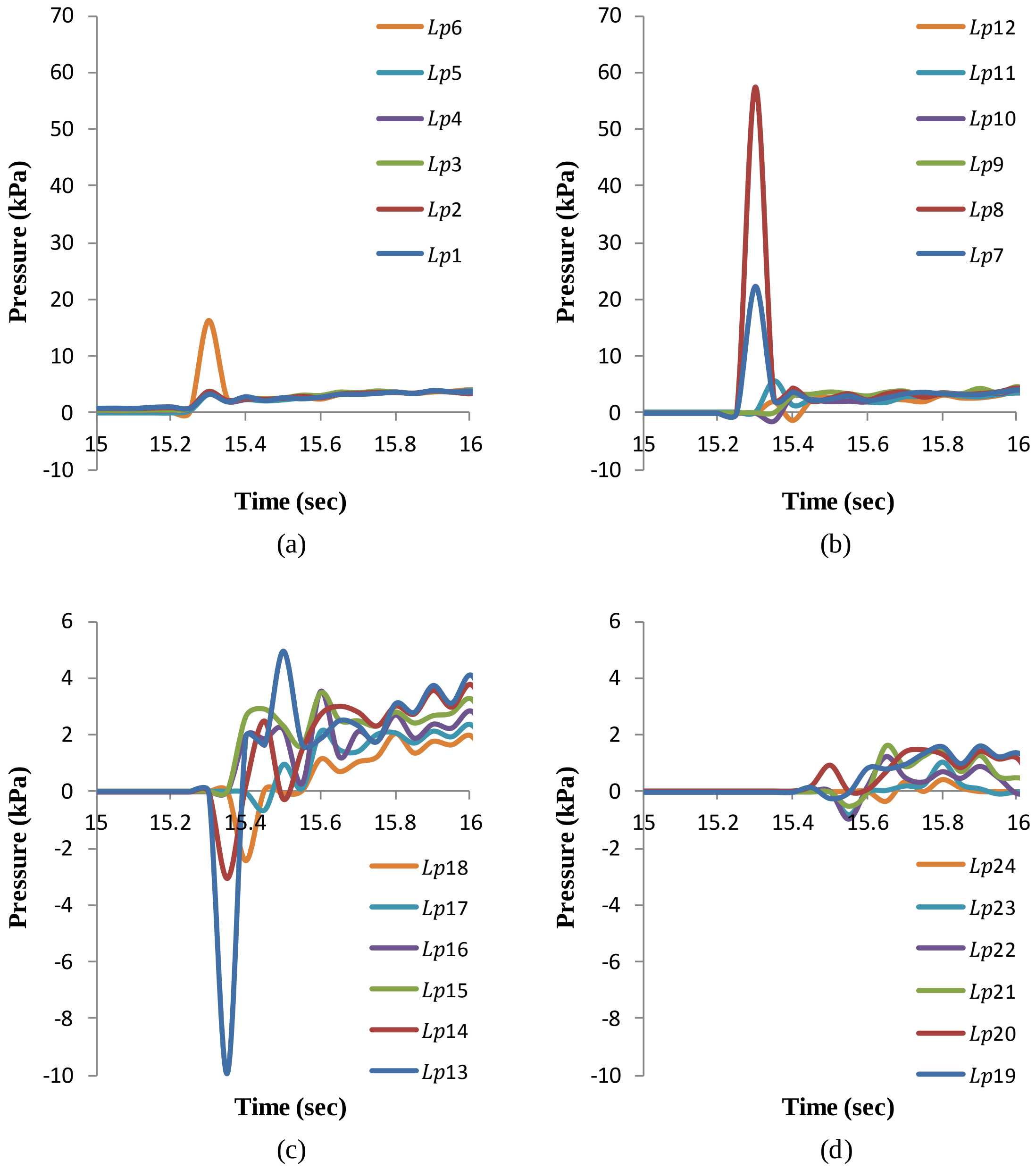

Figure 6.2 Load-time history for the timber wall FE model

The applied load is related with the mesh size of the FE model. The mesh was refined at the loaded area to have resolution similar in size to the SPH model particle size of 0.020 m, and gradually coarser towards the top of the wall. The reason for the spatial compatibility of the finite-element mesh and SPH particle size was purely to make it simpler to apply the SPH pressure outputs on the finite-element wall by maintaining the same degree of resolution in pressure variation. The mesh size of the timber wall can be seen in Figure 6.3, where small arrows represent the acting loads. The elements of model 1 in ABAQUS were created by using the eight-node linear brick elements, C3D8R. The analysis step with a time period of 20 s was in line with the duration of the SPH model output time, and time increments of 0.005 s. For the analysis, the ABAQUS dynamic-explicit procedure was used. The timber in the frame was defined as an anisotropic material. The damping ratio was less than 5% and without considering strain rate dependency.

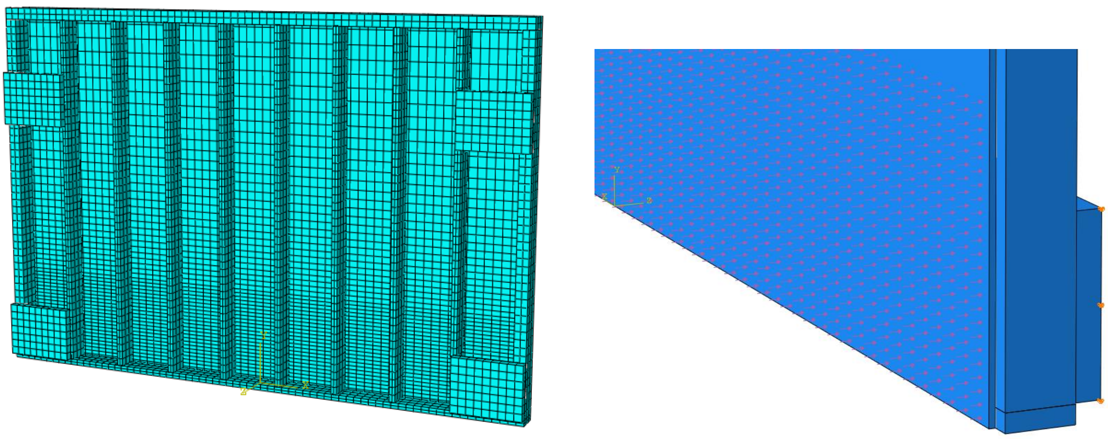

(a) the mesh of elements (b) acting pressure showing by arrows

Figure 6.3 Model 1: Mesh and loading

6.2.3 Modelling results

The behaviour of timber structures observed under transient tsunami-like wave impact was analysed in terms of deflection and stress distributions. The deflection contours for the wall and the comparison of numerical and experimental deflections are depicted in Figure 6.4.

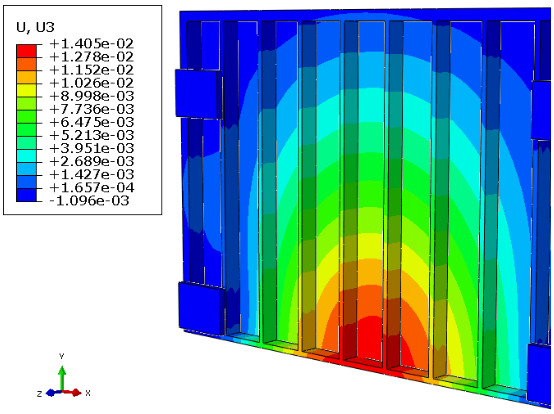

(a) the deflection contours at peak force

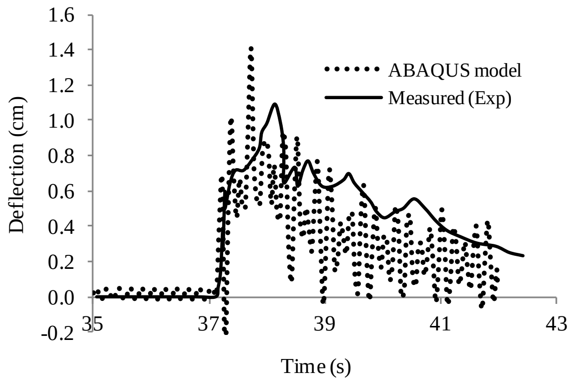

(b) the comparison of wall deflection at bottom of vertical centreline

Figure 6.4 Deflection of Model 2

The maximum deflection is located at the bottom-centre of the wall and gradually changes along the height of wall; it is generally consistent with the experimental data. In general the finite-element model prediction on maximum deflection is about 28.4% higher than experimental data. This can be accounted for by the fact that dissipation of wave force on impact is not modelled in the SPH simulation; that is, in the hydrodynamic simulation the structure is considered to be perfectly rigid. In parallel to this, it is likely that the finite-element model is sensitive to the level of damping inherent in the structure and further research of this parameter is needed.

Figure 6.5 shows the S11 stress contours at the point of peak wave force in the plywood surface, that is, the surface in contact with the wave. The S11 is the stress that is normal to the plane. Maximum tensile stresses occur near the bottom of the panel at the load cell positions. The magnitude of the peak stresses are such that the plywood is likely to be working near capacity. Figure 6.6 shows the surface stresses in the rear face of the wall at peak wave force. The highest tensile stresses occur in the middle of the lowest horizontal rib; the magnitudes indicate the timber is working close to capacity. In the physical model, tensile failure of the lowest rib occurred in the same location. Sources of variability in numerical and physical stress concentrations may occur from the natural variation in the timber itself, mesh sensitivity in the finite-element model and the 2-D simplification of the numerical wave front.

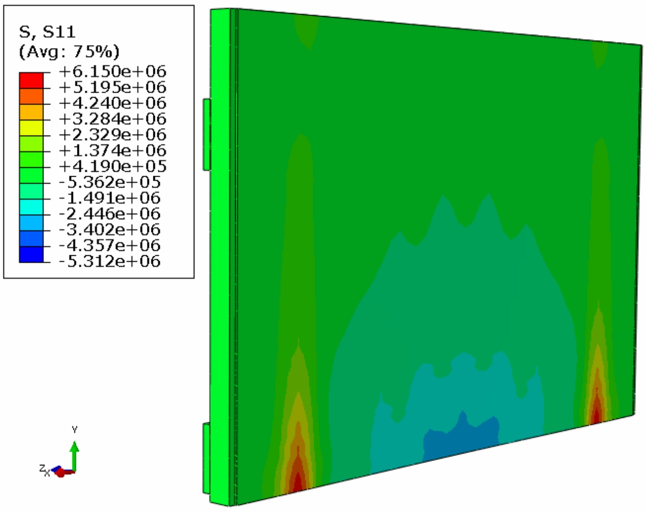

Figure 6.5 The S11 stress (N/m^2) distribution on the plywood surface of Model 1

(If the values for elements and nodes are within 75% of each other, they will be average and then displayed)

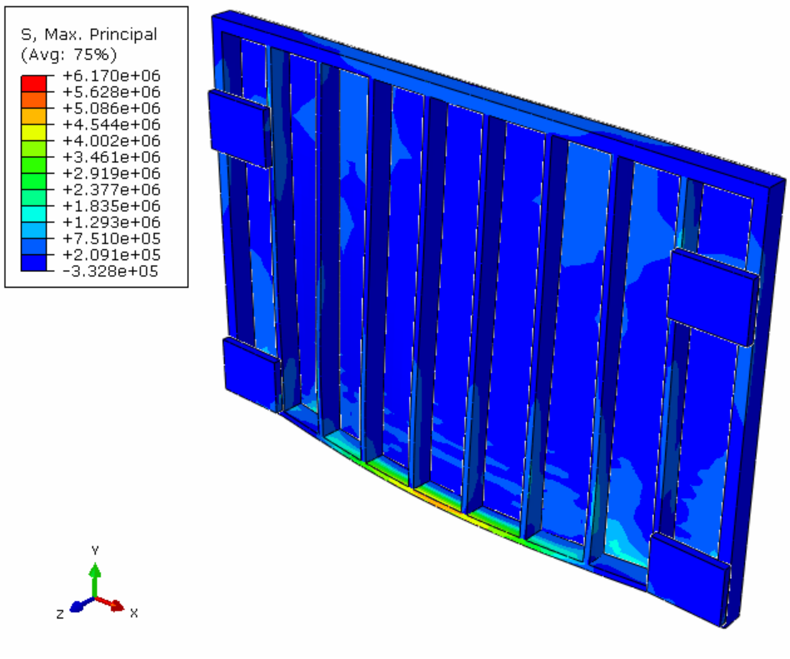

Figure 6.6 The maximum principal stress (N/m^2) at the studs of Model 1

6.3 Timber house model (Model 2)

The design of Model 2 is intended to study the response of a timber house at a real scale under tsunami-like bore loadings. Model 2 was a scale up version of an idealised coastal structure treated as a cube in the SPH model and was designed following a standard practice for one or two story dwelling house (International Code Council, 2009).

6.3.1 Model set up and properties

As a representation of a simple house, Model 2 includes vertical walls and a flat roof. The walls and roof are composed of sandwich timber panels which are an arrangement of sheath-stud-sheath. Figure 6.7 shows a definition sketch of the timber structure. The structure dimensions for Model 2 are 3m x 3m x 3m. The sheath is made of plywood with 13 mm thickness and has the following material properties: density = 750 kg/m^3, Young's modulus = $7.7x10^9$ N/m^2 and Poisson's ratio = 0.22. The studs are made of softwood timber (Douglas fir) with a cross sectional size of 38 mm wide x 140 mm deep and installed with spacing centres of 420 mm. The studs' material properties are as follows: density = 530 kg/m^3, Young's modulus = $7.0x10^9$ N/m^2 and Poisson's ratio = 0.22. The timber structure was designed to be simply supported at the base, that is no rotational fixity.

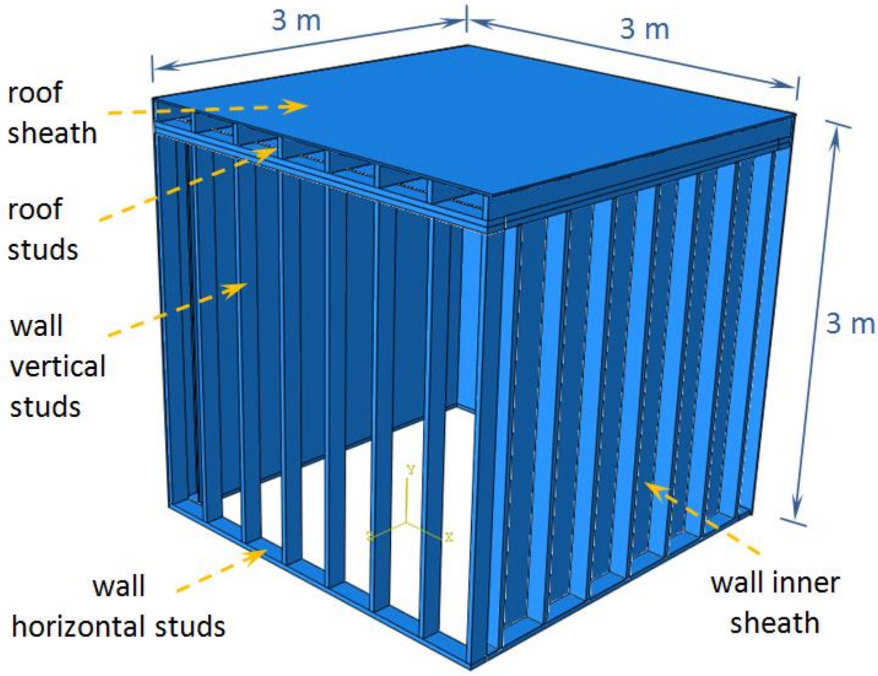

Figure 6.7 General arrangement of Model 2 (wall sheaths removed for clarity as shown).

6.3.2 Applied load and finite element analysis

The applied pressure-time histories on the FE model structures were obtained from the DualSPHysics output. The size of the structure in the FE model was scaled up by a factor of three from the structure in the DualSPHysics model. Thus, following dimensional analysis using Froude number scaling (McCormick, 2010), the magnitude of applied pressures on the surface of the FE models was also scaled up by three from the DualSPHysics output pressures. The pressure-time histories of applied loads can be seen in Figure 6.8 for both wave simulation cases with H/h_0 = 0.3 and 0.5. The output pressure from the wave simulation with H/h_0 = 0.1 was not included in the FE model analysis because the magnitude was relatively small. The FE structure responses were studied by applying two different pressure time histories (as shown in Figure 6.8) on the front surface of the structure.

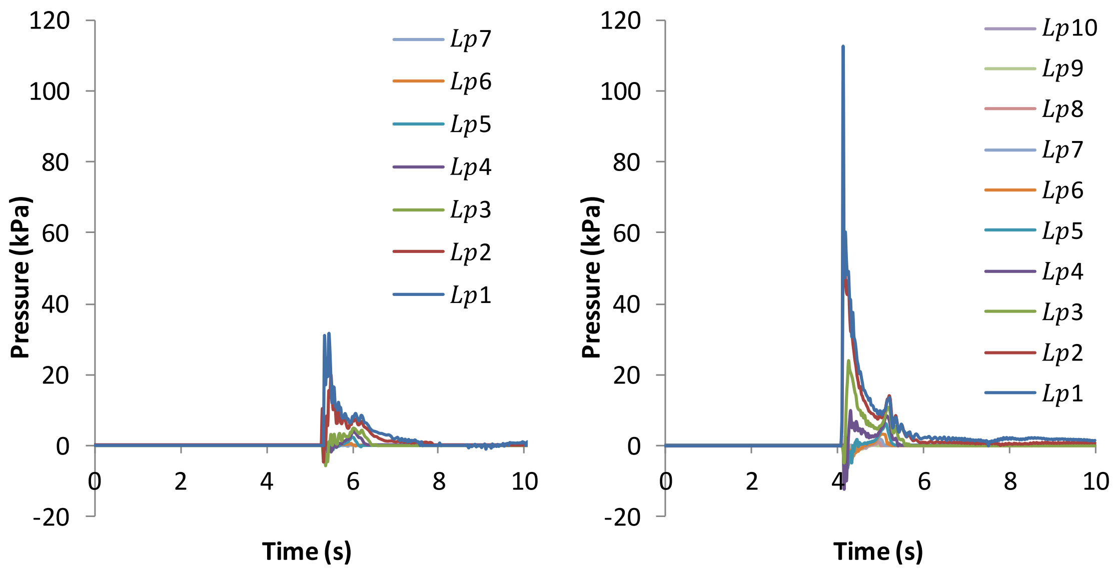

(a) $H/h_0 = 0.3$ (b) $H/h_0 = 0.5$

Figure 6.8 Applied pressure time histories for the finite element models.

The pressures applied on the vertical surface of the structures were divided into 10 layers. This number of layers was identical with the number of probes arranged vertically in the SPH model, denoted by *Lp* in Figure 6.8. The magnitude of pressure at each layer is the average pressure measured by pressure probes at the associated layer. The reason for applying average pressure history at each layer was based on time efficiency. Figure 6.8(a) shows the applied loads presented from Layer 1 to Layer 7 (*Lp*1 to *Lp*7). Loads at Layer 8 to Layer 10 (*Lp*8 to *Lp*10) are zero so they were not included in the graph. In Figure 6.8(b) all 10 layers were loaded. The loaded layers on the surface were related with the height of bore runup on the surface of the wall.

The negative pressure values in Figure 6.8 reflect the application of the equation of state in DualSPHysics and a rebound or suction effect. DualSPHysics version 3.0 is still a single phase model that cannot yet perform multi-phase behaviour including air and water at the same time. The next version of DualSPHysics (version 4.0) is being developed to be capable of performing such multi-phase modelling (Mokos *et al.*, 2015). Two peaks are shown in the pressure-time histories in Figure 6.8. The first peak occurred when the leading edge of the bore impacted the structure and the second peak occurred when splashing followed with the main flow. These two peak phenomena are typical for impact loads of this type and were also observed in the experiment by Fujima *et al*. (2009). Note in the case of the immediate impact on the structure, no additional force is applied e.g. drag force. The hydrodynamic 'drag' forces indeed occur in real tsunami events (Yeh *et al*., 2014) and affect the structure when surrounded by a 'steady' fluid flow with relatively constant velocity (FEMA, 2011). However in this simulation, the hydrodynamic drag was not so significant because of the application of a single stroke solitary wave where the most dominant effect was the highly transient impulsive pressure immediately following the impact of the leading edge of the arriving water mass.

6.3.3 Modelling results

The finite element analysis was performed using the ABAQUS Dynamic Explicit module with duration of simulation of 2.6 seconds and the time increment automatically determined by the program. The duration of simulation was enough to capture the important segment of pressure-time histories given in Figure 6.8 incorporating the peak impact and subsequent impact. All components of the structure were meshed with the finest mesh on the front surface. The size of the mesh for the front impacted surface was 0.05 m to correspond with the diameter of SPH fluid particles, a coarser mesh with twice the size of elements was used for the other sides of the structure. The response of the structures is shown in terms of the maximum principal stress that occurred on the members. On the front face of the structure, the main load carrying elements are the vertical and horizontal studs and these are shown in Figure 6.9 by omitting the outer plywood cover sheath. The results of the finite element modelling can be seen in Figure 6.9 which consists of four figures showing the response of the structure under different loading conditions. Figure 6.9(a) and Figure 6.9(b) shows the response of structures loaded by the SPH pressure time-history resulting from a normalised wave height H/h_0 = 0.3 and 0.5, respectively. Figure 6.9(c) and Figure 6.9(d) on the other hand show the response of the structure under a quasi-static pressure determined using the semi-empirical approach given by the following equation (CCH, 2000):

$$F_s = \frac{1}{2}\rho g h^2 b + 4\,\rho g h^2 b = 4.5\rho g h^2 b \qquad (6.1)$$

using the equivalent wave properties. The pressures related with Figure 6.9 and Figure 6.9(d) were calculated based on a bore height of 0.60 m and 0.96 m, respectively, where those bore heights were taken from the SPH model simulation and scaled-up by a factor of 3. The application of those bore heights in Equation (6.1) was intended to accomplish straightforward comparison of the structure's response based on numerical and semi-empirical approaches.

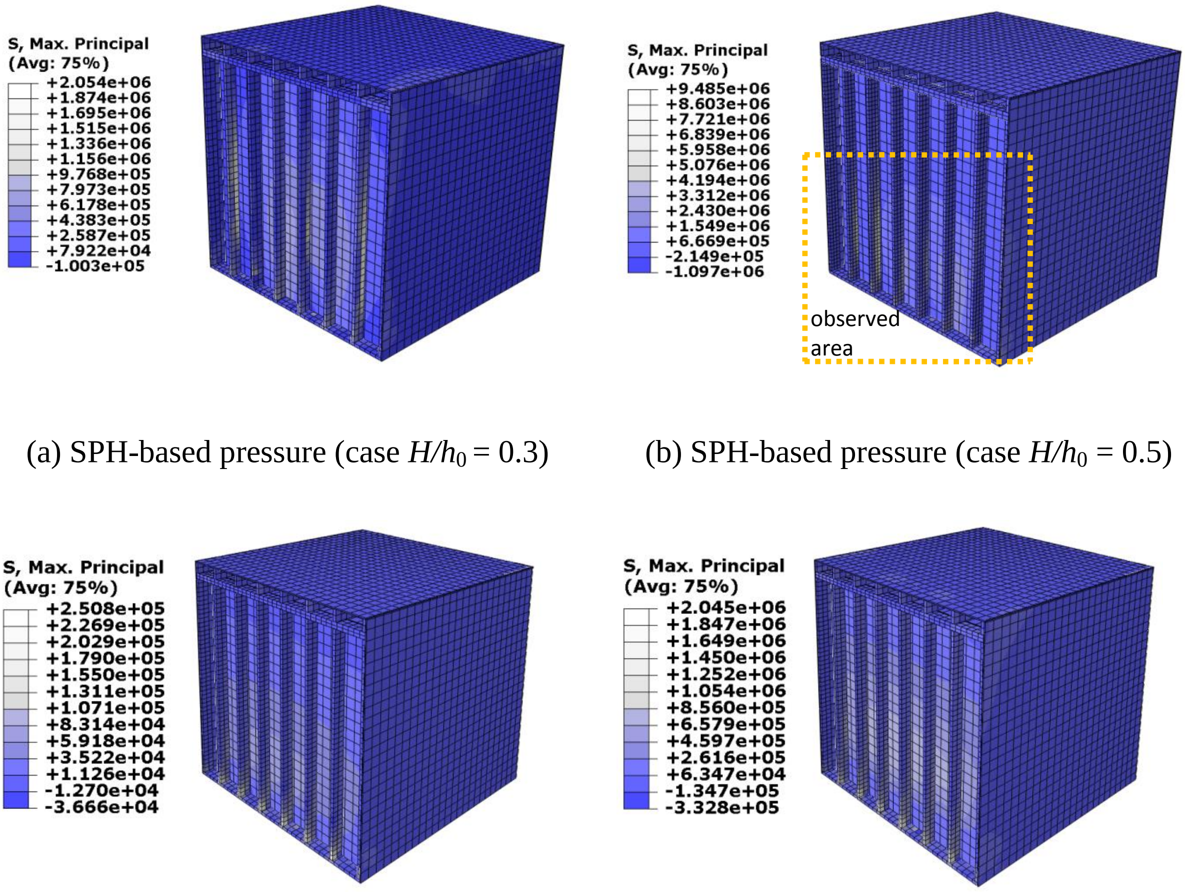

(a) SPH-based pressure (case $H/h_0 = 0.3$)

(b) SPH-based pressure (case $H/h_0 = 0.5$)

(c) Quasi static-based pressure (case $H/h_0 = 0.3$)

(d) Quasi static-based pressure (case $H/h_0 = 0.5$)

Figure 6.9 The dynamic response in ABAQUS due to SPH pressure-time history (a, b); the static response in ABAQUS due to quasi-static pressure from Equation (6.1); (all stresses shown in N/m^2).

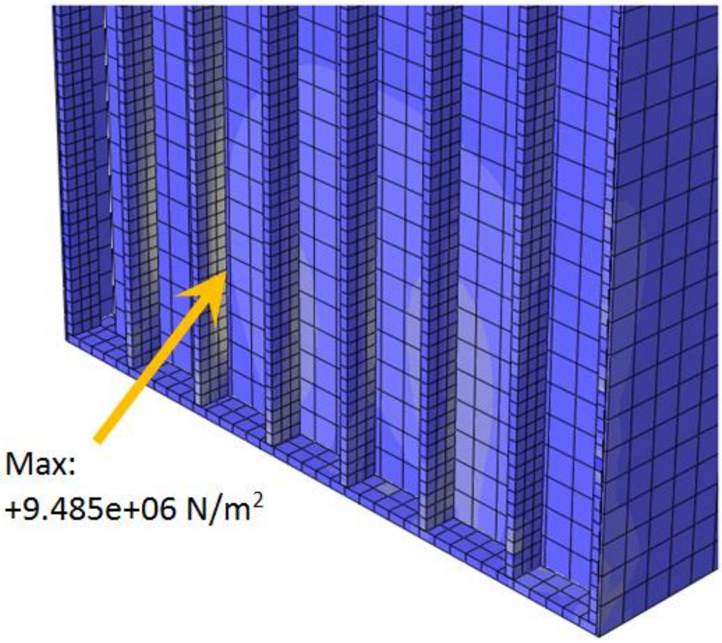

Figure 6.10 Close up view of area of maximum stress indicated in Figure 6.9(b).

From Figure 6.10, it can be clearly seen that the vertical timber studs are heavily loaded and depending on the timber grade strength, such magnitude of stress could result in rupture.

6.4 Concluding remarks

The finite element analyses using ABAQUS has been shown to be able to be coupled with the SPH method. The results from the DualSPHysics models were utilised in the finite element models as input loads to predict the response of the structure under transient bore impact loads. By using the same SPH pressure measuring probe spacing and FE mesh size, the SPH output pressure can be directly applied to the finite element model. This chapter has also shown that the behaviour of a vertical timber wall (Model 1) is in good agreement with the experimental results. Based on this, a further development for modelling a more complex structure of a complete timber building has been conducted. Using the timber building, the numerical pressure predictions were compared with pressure predictions from semi-empirical approaches used in design codes. The results shows that the resulting maximum stress on timber components due to the semi empirical design equation are almost one order of magnitude lower than same stress prediction given by method used in this thesis. The structure response results highlight the potential for non-conservatisms in the empirical approaches. The techniques outlined here can allow engineers to gain a better insight into tsunami wave-structure interaction and thus lead to resilience optimisation of structures vulnerable to these type of events.

Chapter 7

Storm Wave Impact Modelling using DualSPHysics

7.1 Introduction

So far, this thesis has concentrated on the application of the SPH and FE approach to modelling tsunami-like wave impacts on discrete structures. Although the effects of tsunami events can be catastrophic and far reaching, tsunamis remain statistically rare. For coastal structures, more frequent damage may be incurred by regular storm waves which are briefly considered here. This is particularly true of linear coastal defence structures and management of such occurrences often being the focus of the practice community. This chapter provides the results of the hydrodynamic modelling of storm waves using the DualSPHysics software as a means of demonstrating the applicability of the method to everyday coastal engineering problems. Methods for generating waves in the numerical simulation based on paddle motion are briefly described. The simulation of short waves impacting a 2-D recurve wall is presented and the results discussed.

7.2 Generating waves with numerical paddle motion

In recent research waves that are numerically simulated using DualSPHysics tend to be generated by the movement of the numerical paddle wavemaker. Two numerical paddle movements are utilized: (1) the rectangular sinusoidal paddle motion for generating short waves, (2) the paddle motion based on Goring's equation for simulating tsunami-like waves where the results are presented in Section 7.3.

The short wave in shallow water was used to simulate wind-driven waves that propagate towards onshore and repeatedly hit coastal structures. Galvin (1964) proposed a simple theory to generate a wave in shallow water where the water displaced by the wavemaker should be equal to the crest volume of the propagating wave form as illustrated in Figure 7.1. For example, consider a piston wavemaker with a stroke S which is constant over a depth h. The volume of water displaced over a whole stroke is Sh. The volume of water in a wave crest is $\int_0^{L/2}(H/2)\sin(kx)\,dx = H/k$. Equating the two volumes;

$$Sh = \frac{H}{k} = \frac{H}{2}\left(\frac{L}{2}\right)\frac{2}{\pi} \tag{7.1}$$

In which the $2/\pi$ factor represents the ratio of the shaded area of the enclosing rectangle. This equation can also be expressed as:

$$\left(\frac{H}{S}\right)_{\text{piston}} = kh \tag{7.2}$$

where H/S is the height-to-stroke ratio and k is the wave number $(2\pi/L)$. The wavemaker theory for different types of paddle motion (e.g. flap-type) can be found in Dean and Dalrymple (1991). The application of this theory in DualSPHysics was conducted by entering the properties of design waves (frequency and amplitude) in the XML input file of the DualSPHysics CaseWavemaker.

In Chapter 3 and Chapter 5, the solitary waves were designed based on Goring's equations. The displacement-time history for a desired solitary wave height is determined following Goring's equation and the displacement-time history is introduced to the DualSPHysics CaseWavemaker.

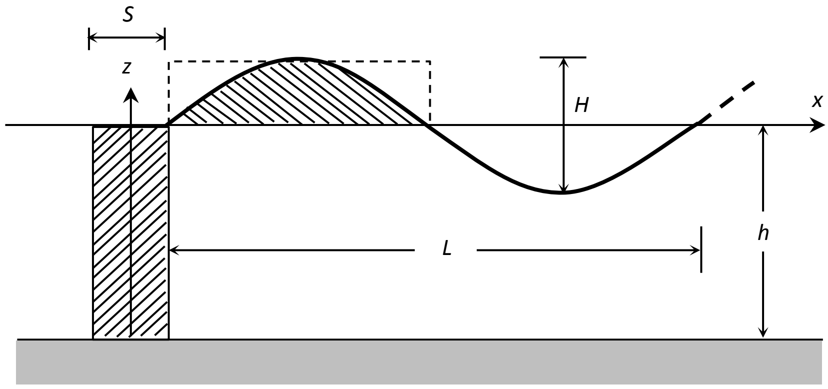

Figure 7.1 Simplified shallow water piston-type wavemaker theory

7.3 Short waves impacting a coastal recurve wall in 2-D

Coastal defences are built to protect coastal onshore structures from violent wave impacts. One of the examples of coastal defence structures is a recurve wall which has an S-shape geometry (Figure 7.2) that is designed to reduce the incoming wave energy by deflecting the wave and at the same time reduce overtopping. This kind of sea wall can be found in some of the UK coastal areas such as Anchorsholme near Blackpool. The nature and form of a sea wall is very important especially in popular tourist areas; not only for protecting the people but also the expensive investment in public infrastructures. The existing concrete recurve wall at Anchorsholme was built around the 1930s and was recently found to have sustained damage to the recurve element during a major storm. Based on a field investigation, the upper seaward-bull-nose part of the wave recurves had sheared over a significant length due to impulsive wave impacts (Cunningham, 2014). A study was conducted to find the breaking wave pressures whose magnitude exceeded the resistance of the concrete structures.

Figure 7.2 An example of a recurve wall coastal defence (Moore-Concrete, 2015)

Various existing numerical approaches have been shown to be capable of modelling wave pressures on seawalls, with different degrees of accuracy, detail and applicability. One such method which has been shown to be effective and computationally efficient for modelling impulsive waves on linear structures is the Shallow Water and Boussinesq (SWAB) model (McCabe, 2011). Such models are not applicable to modelling impulsive wave pressure situations. McCabe (2011) used the SWAB approach to model pulsating wave impacts and overtopping for the Anchorsholme seawall. In recent research the modelling of violent regular waves was performed in 2-D using SPH models with a fixed boundary in the form of a water tank that includes a wavemaker, fluid particles, and recurve wall with onshore promenade. A 2-D model is assumed to be sufficient for capturing the behaviour of wave impact on a typical non-discrete long structure such as a coastal defence because it has a uniformly longitudinal cross section. The details of the Anchorsholme 1930's recurve wall cross section can be seen in Figure 7.3, where the toe of the structure is at the bottom-left and is connected with a sloping apron which is followed by four terraces. The upper-most terrace is connected by a mild sloping berm to the S-shape recurve wall. The promenade length is about 13.7 m which is 0.51 m lower than the top surface. The water level is about 4.5 m and inundates the terraces part downward.

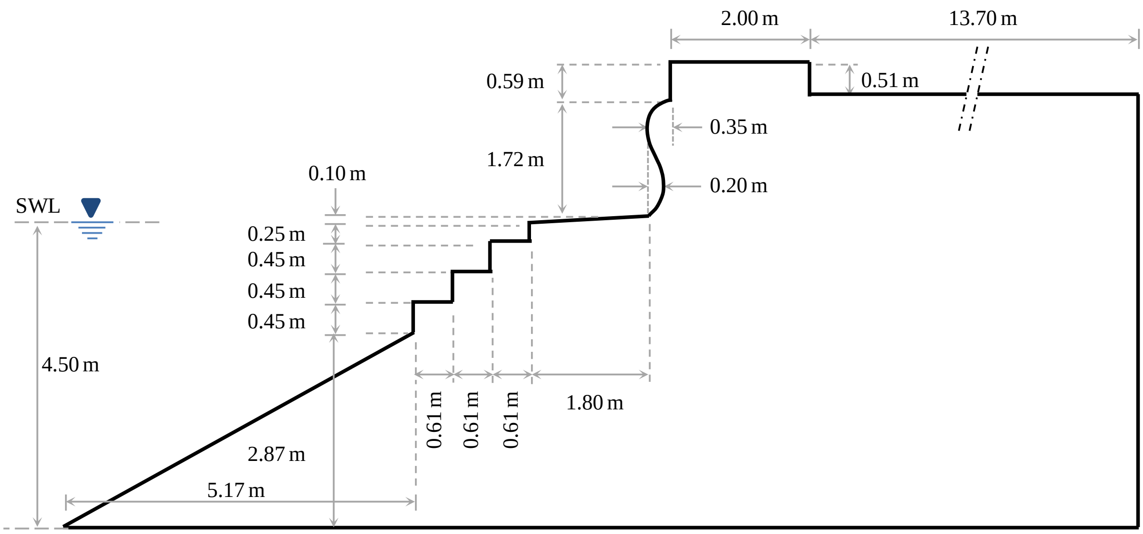

Figure 7.3 The 1930s recurve wall structure's cross section at Anchorsholme

Figure 7.4 shows the numerical SPH model where the recurve wall structure is located within the boundary. A 1:6.6 slope is added to connect the structure to the offshore sea bed. The distance between the paddle and structure is shown to be 50 m, however this value is varied as explained later. For this initial study, the storm waves were modelled as simple uniform wave trains with constant significant wave height and peak period based on the available data from the nearby wave bouy at Cleveleys, Lancashire. A more detailed time-series approach to the wave modelling is discussed later in this chapter. The paddle motions were designed to generate regular waves with 7 sec and 10 sec periods while the wave height was kept constant 4.5 m. The resolution/particle size used in the model was 0.025m. For the domain shown in Figure 7.4, the total number of particles was 502,083, of which 98 percent were water particles. The dashed line at the promenade illustrates a variation that was made to study the wave overtopping behaviour as can be seen in Figure 7.5.

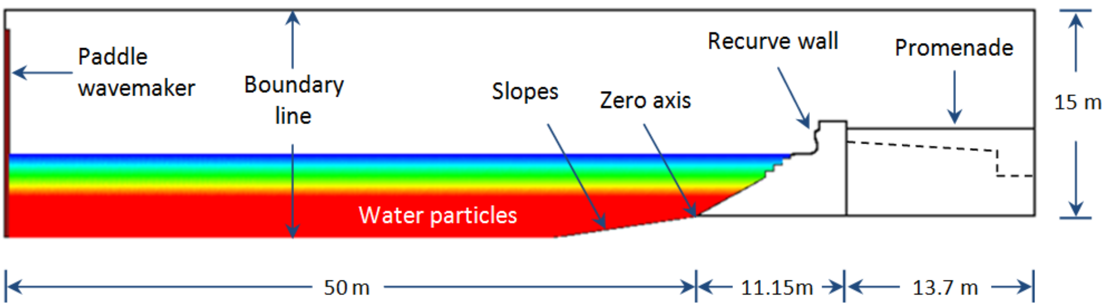

Figure 7.4 The boundary of 2-D numerical SPH model

The absence of a promenade as shown in Figure 7.5(a) strongly influences the behaviour of wave impact in front of the recurve wall where the returned water after hitting the vertical boundary wall collided with the succeeding waves, so that the wave impact pressures were also being disturbed.

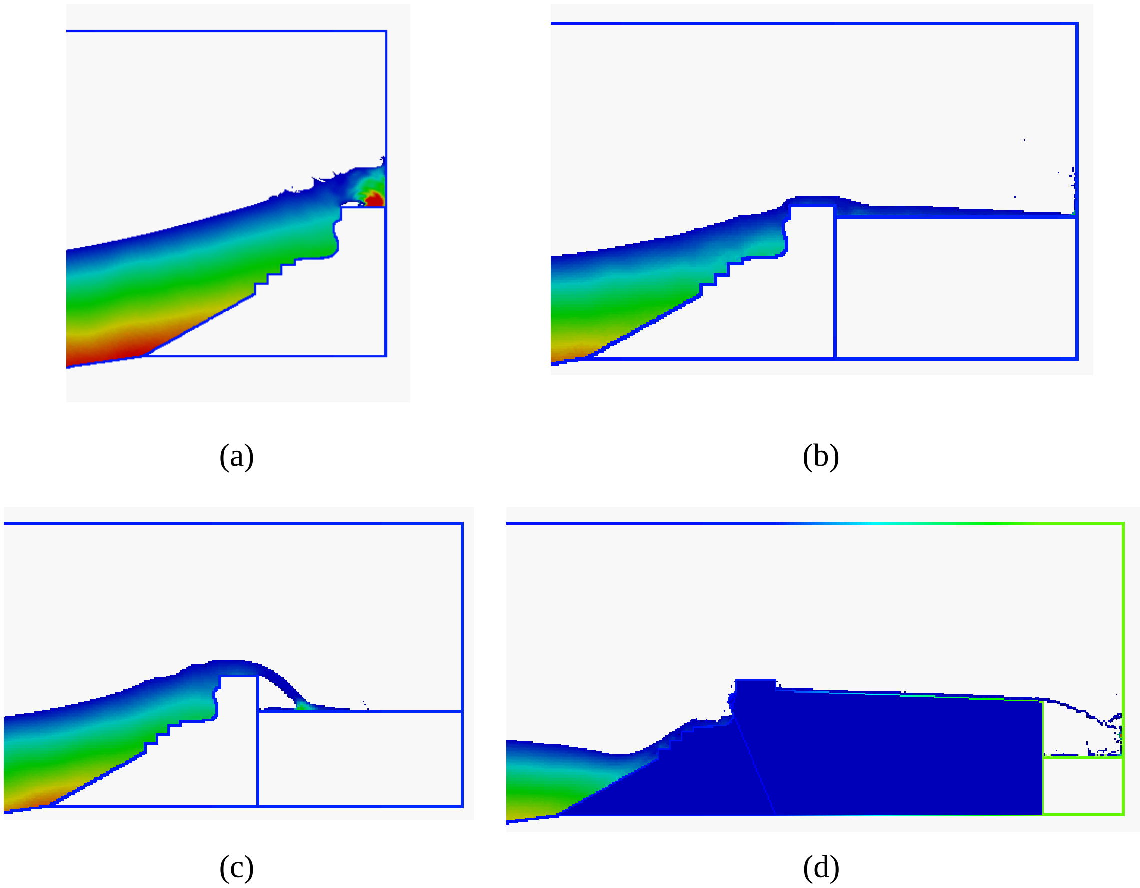

Figure 7.5 Different promenade shapes and sizes

An attempt to mitigate this effect was made by adding a space behind the recurve wall as shown by Figure 7.5(b), (c) and (d). Figure 7.5(b) represents a promenade with distance 13.7 m behind the recurve wall where this measurement was taken from field observation. The wave impact behaviour seemed more realistic by allowing some part of the water to overtop the recurve wall but this promenade was quickly drowned after the second wave impacts due to its shallow depth. The following attempts were made by increasing the depth of the promenade and the design of inclined promenade with gutter as can be seen in Figure 7.5(c) and (d), respectively, to prevent the overtopped water returning offshore. Although those designs seemed unrealistic in terms of seaward returning water, they gave an indication of the amount of overtopping water in this scenario. For the rest of the simulations, the promenade model in Figure 7.5(b) is used since it is the actual model based on field evaluation.

A preliminary SPH numerical simulation was conducted by modelling a water tank with a paddle distance to the toe of structure of 45 m. The total simulation physical time was 30 sec allowing 3 complete wave periods to be generated. The analysis results shown in Figure 7.6 revealed that the maximum wave impact pressures on the wall vary with time along the height of the recurve wall. With the displayed pressure-time history at different levels as measured by numerical probes, the impact events that may give the most significant effect to the recurve wall can be observed.

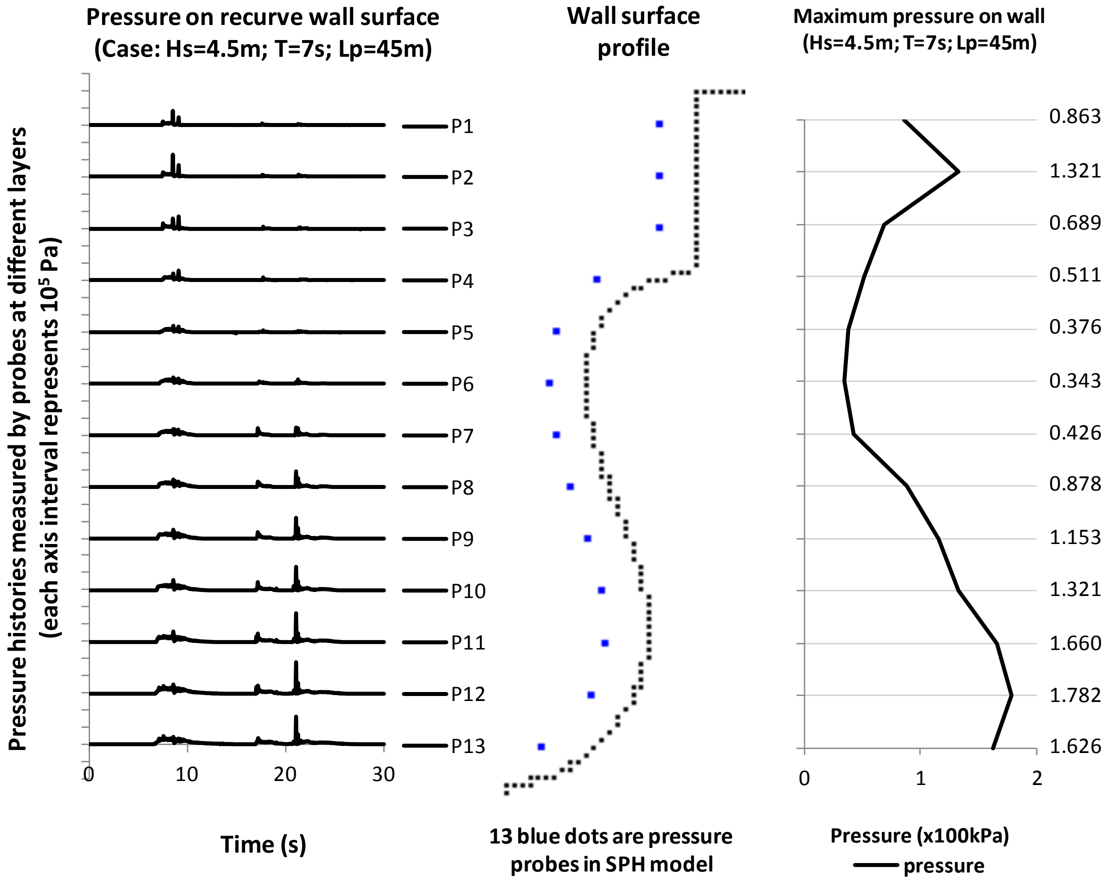

Figure 7.6 Pressure time history for models with *Lp* = 45 m

Based on previous studies including testing of concrete samples from the damaged wall (Cunningham, 2014), wave pressures greater than or equal to 200kN/m^2 acting vertically upwards on the underside of the out-stand (bullnose) of the recurve would be required to cause the type of shearing damage observed in the field. From this short simulation, it can be seen that those magnitude of impact pressures were not realised. The maximum pressure occurred at the bottom part of wall where it recurves and logically this shape will reduce the wave impact energy. The simulation of wave impact that gave the maximum pressure associated with Figure 7.6 is shown in Figure 7.7. Hence, a longer time simulation is needed to see the more comprehensive impact behaviour that may occur. Based on this preliminary simulation, the numerical models were re-produced with the same resolution but with further paddle distances and longer physical time simulations to enable the runs to generate at least to produce 10 wave impacts. A parametric study of paddle position was conducted to isolate the effects of any paddle reflections. By moving the paddle further from the shore, the length of the water tank was increased and as a consequence the numbers of particles were increased.

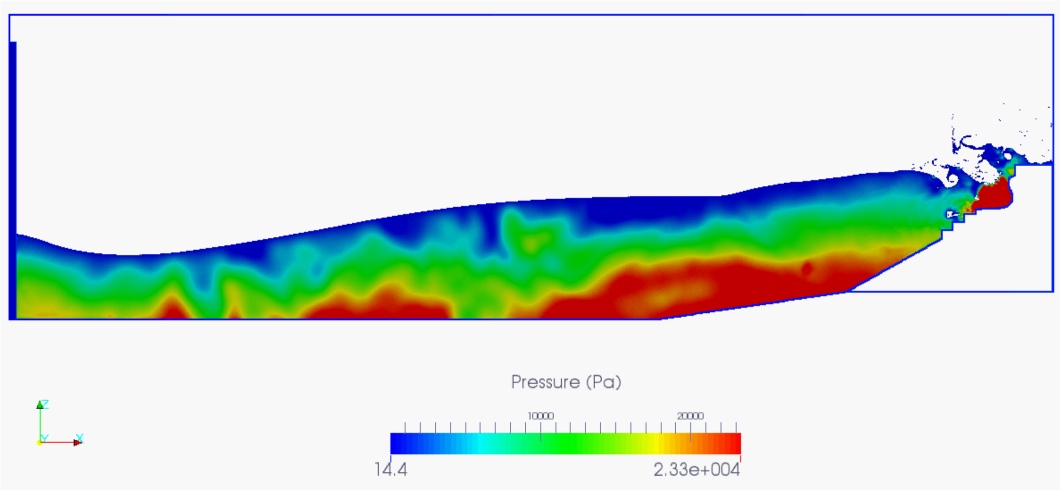

Figure 7.7 Simulation of maximum wave impact on recurve wall

Following the previous simulation, a different simulation was performed for the wave impact on the recurve wall and the pressure-time history using a domain of length 50 m. The maximum pressure distributions were depicted in Figure 7.8 through Figure 7.10. The snapshots of the simulations showing the details of maximum impact time and locations were arranged in Table 7.1 through Table 7.3. The resolutions of the following model are the same but with different duration ranges from 70 sec until 100 sec depending on the period of the design wave. The same procedure regarding the simulation results is performed. The pressure-time histories measured by different layers of probes were arranged horizontally at equal spacing and parallel with the vertical arrangement of probes P1-P13. The pressure at each layer is scaled with the same value for a more convenient observation. The maximum pressure values for each layer were also shown to give an overview where the maximum pressures are likely to occur. A notable pattern in the pressure-time histories that contribute for the maximum impacts are circled to make the observation easier.

Figure 7.8 shows the results of simulation for the case with wave period T = 7 sec and a distance between the paddle and the toe of structure L_p = 50 m. The pressure magnitude is scaled at 10^5 Pa each interval. It can be seen that the significant impact events occurred during the middle of simulation as circled by dashed lines. The maximum impacts took place at P7 and P8, at the mid height and underside of the recurve wall. More details on the time of impact, location and pressure distribution can be seen in Table 7.1.

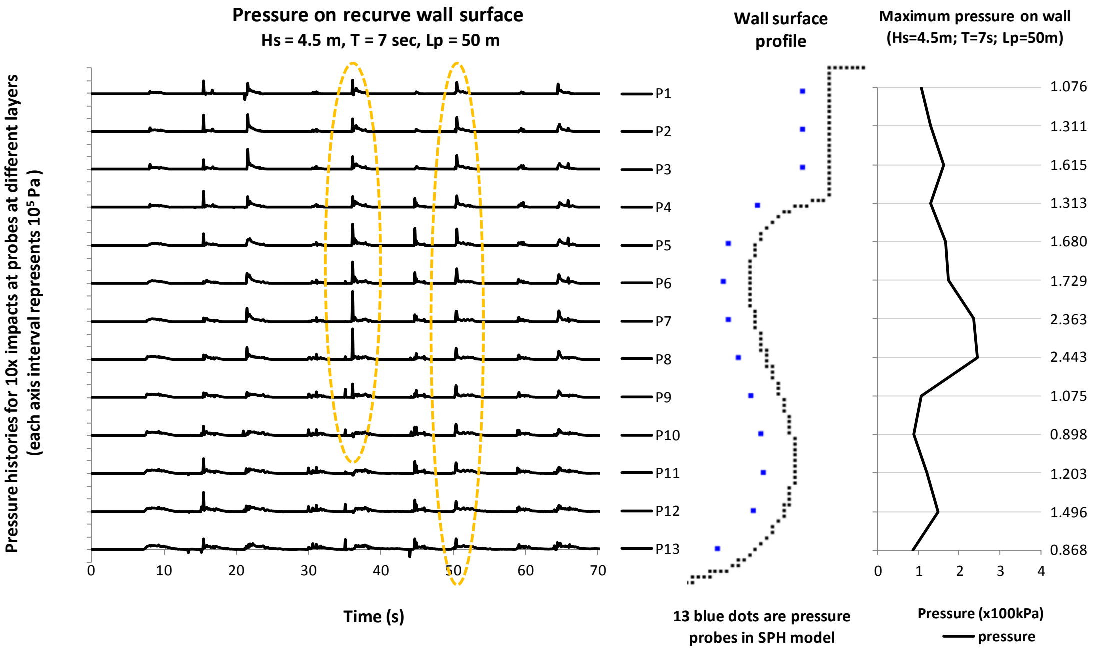

Figure 7.8 Pressure for the case with T = 7 s and L_p = 50 m.

A longer period of wave T = 10 sec but still with the same L_p = 50 m was performed and the pressure results shown in Figure 7.9. The change in this model resulted in different pressure-time histories where the maximum pressure occurred near the beginning and near the end of simulation time that runs for 80 sec. The maximum pressure in this case is higher than the one in Figure 7.8 and occurred at P11 in the bottom part of structure. However this maximum pressure occurs at the location that is not likely to have damaged the structure since in reality the structure was damaged at location between probes P4-P9. The snapshots of this numerical modelling can be viewed in Table 7.2.

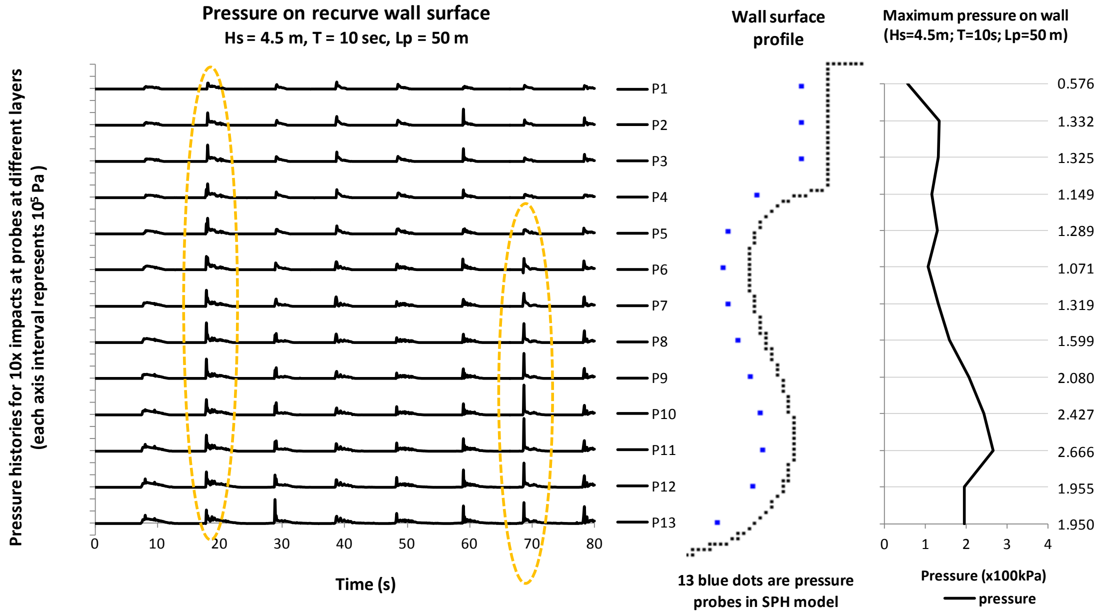

Figure 7.9 Pressure for the case with T = 10 s and L_p = 50 m.

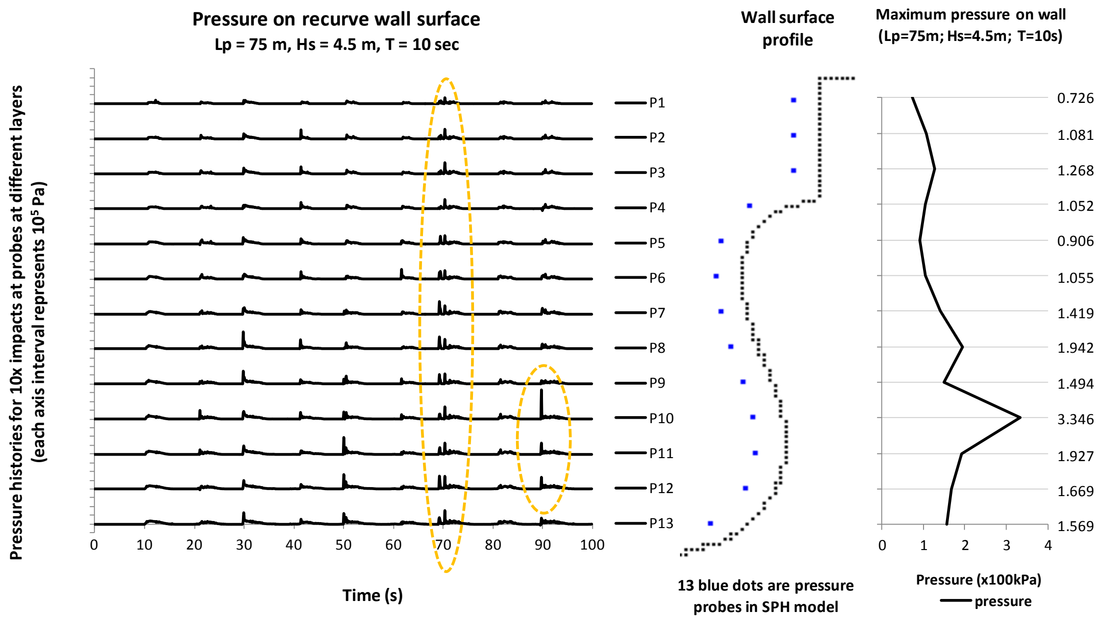

Figure 7.10 Pressure for the case with T = 10 s and L_p = 75 m.

The extension of paddle distance L_p = 75 m has performed to find out the changing behaviour of wave impact on the recurve wall. It was found that the maximum pressure occurs at the half end of the simulation and measured by probes P10. The maximum pressure profile was quite similar with the one in Figure 7.9. The longer paddle distance makes the wave impact on the first half of the simulation in-significant because the waves need a longer time to propagate before reaching the structure, such numerical wave decay can be a limitation of the SPH approach. Note that the pressure results are scaled at $4x10^6$ Pa each layer. More detail on the pressure regarding this simulation can be seen in Table 7.3.

Table 7.1 Model with wave period (T) = 7 sec, L_p = 50 m

#	Snapshots	Remarks
1	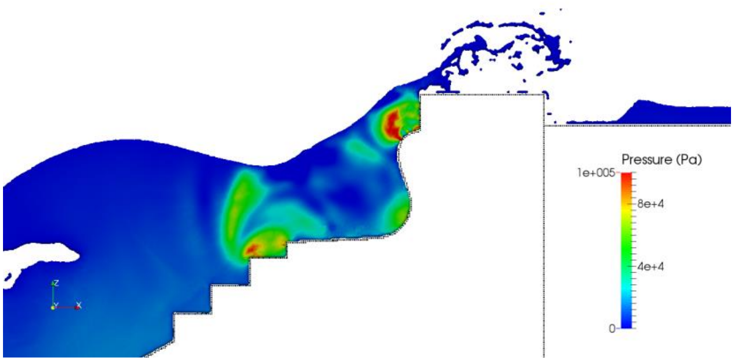	Time = 15.5 sec Timestep = 155 Maximum pressure at probes: P11 (120.29 kPa) and P12 (149.63 kPa)
2	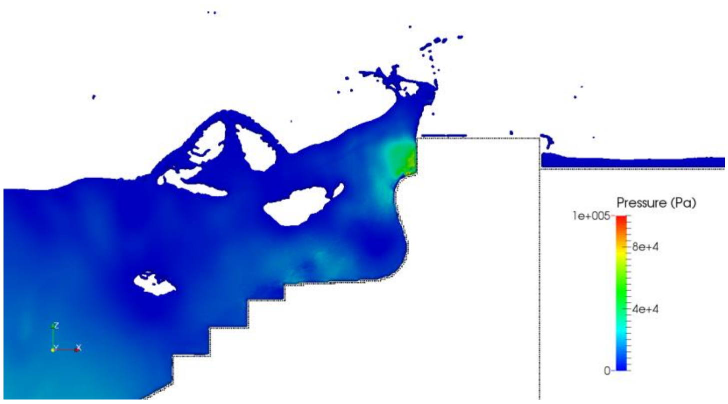	Time = 21.6 sec Timestep = 216 Maximum pressure at probes: P2 (131.13 kPa) and P3 (161.46 kPa)
3	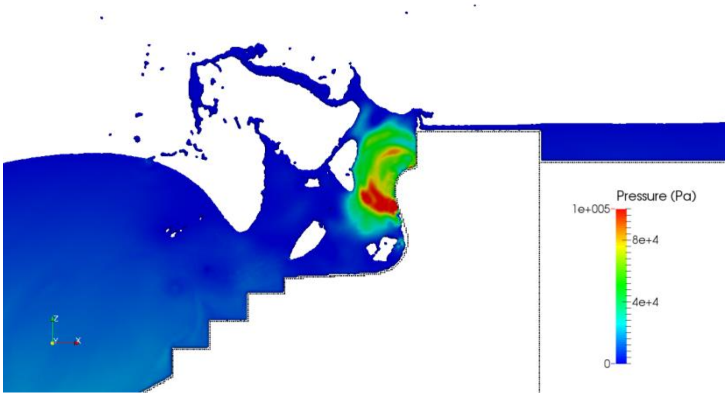	Time = 36.1 sec Timestep = 361 Maximum pressure at probes: P1 (107.58 kPa), P5 (168.05 kPa), P6 (172.89 kPa), P7 (236.28 kPa), P8 (244.31 kPa)/highest P9 (107.45 kPa)

4	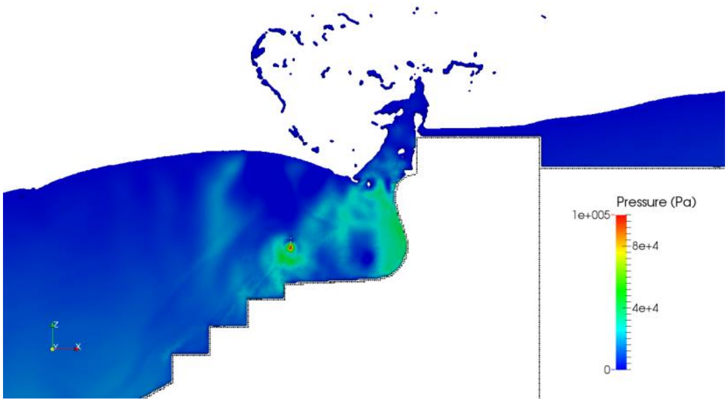	Time = 50.4 sec Timestep = 504 Maximum pressure at probes: P10 (89.82 kPa)
5	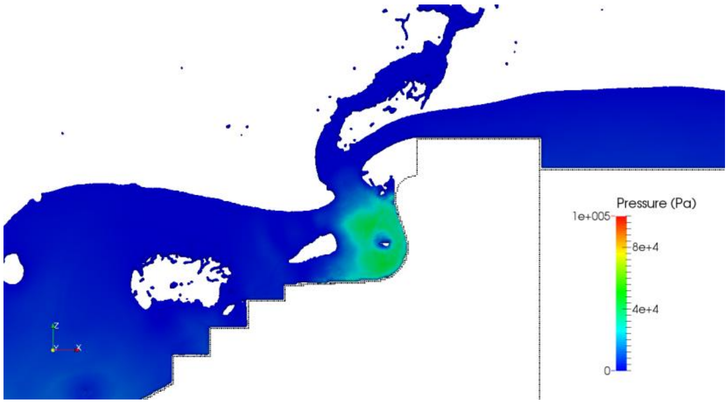	Time = 72.7 sec Timestep = 727 Maximum pressure at probes: P13 (86.76 kPa)

Table 7.2 Model with wave period (T) = 10 sec, L_p = 50 m

#	**Snapshots**	**Remarks**
1	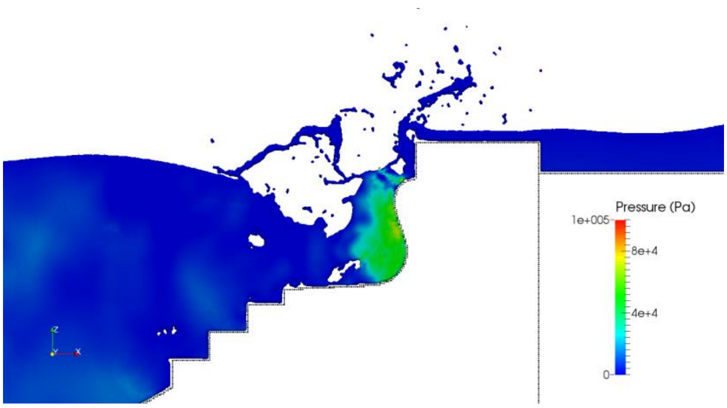	Time = 17.8 sec Timestep = 178 Maximum pressure at probes: P6 (107.06 kPa), P7 (131.88 kPa) and P8 (159.88 kPa)

2	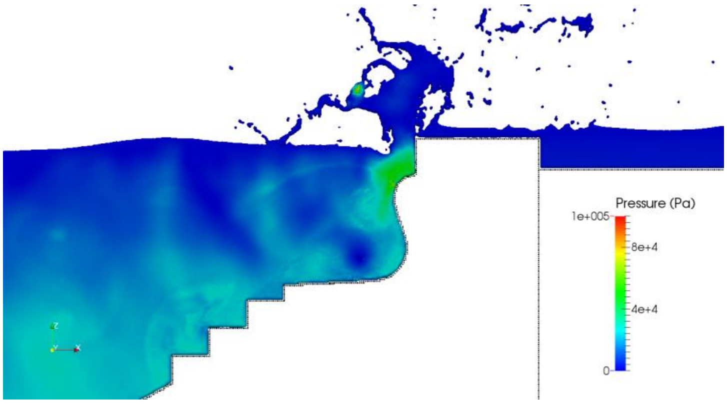	Time = 18.0 sec Timestep = 180 Maximum pressure at probes: P3 (132.45 kPa), P4 (114.92 kPa) and P5 (128.87 kPa)
3	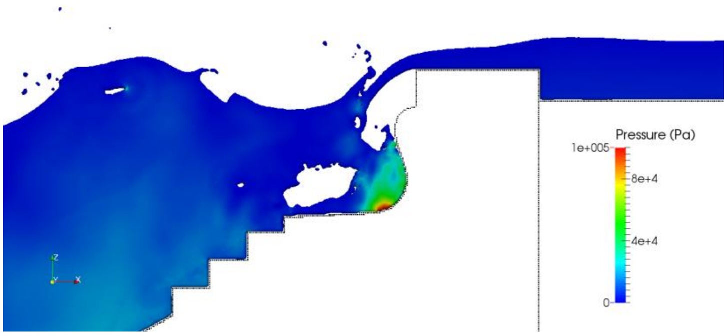	Time = 28.8 sec Timestep = 288 Maximum pressure at probes: P13 (195.57 kPa)
4	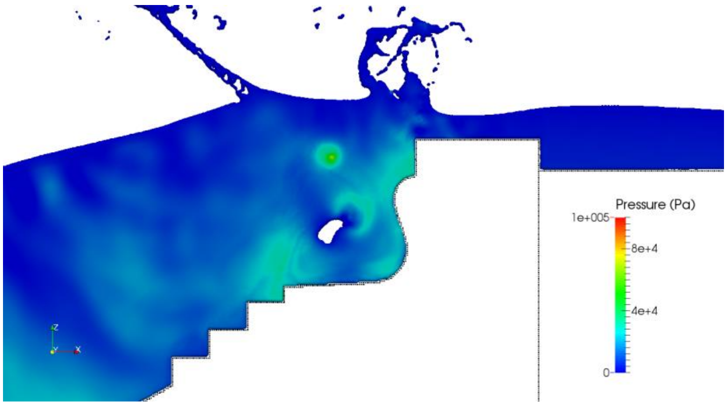	Time = 38.7 sec Timestep = 387 Maximum pressure at probes: P1 (57.57 kPa)
5	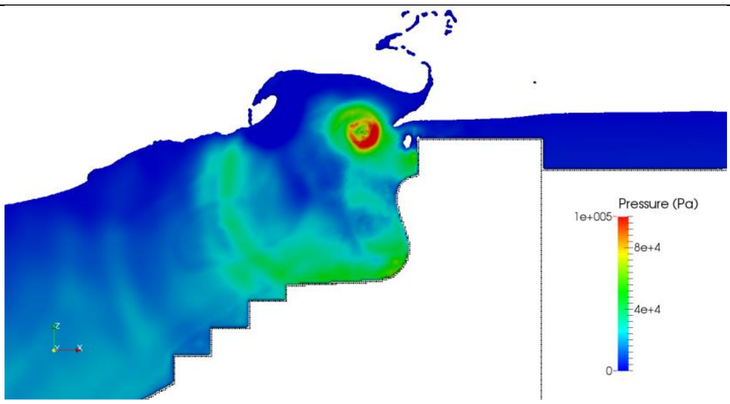	Time = 59.0 sec Timestep = 590 Maximum pressure at probes: P2 (133.17 kPa)

6	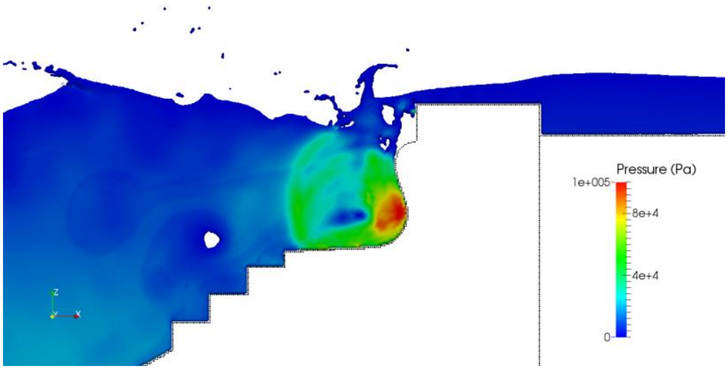	Time = 68.7 sec Timestep = 687 Maximum pressure at probes: P9 (208.00 kPa), P10 (242.65 kPa), P11 (266.58 kPa)/highest and P12 (195.49 kPa)

Table 7.3 Model with wave period (T) = 10 sec, L_p = 75 m.

#	Snapshots	Remarks
1	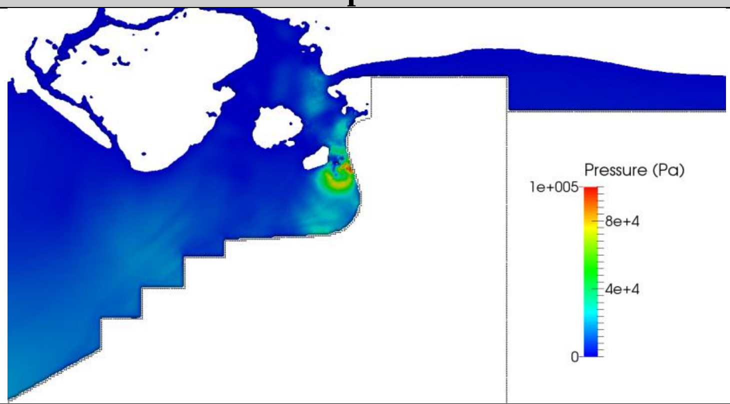	Time = 29.9 sec Timestep = 299 Maximum pressure at probes: P8 (194.21 kPa) and P9 (149.41 kPa)
2	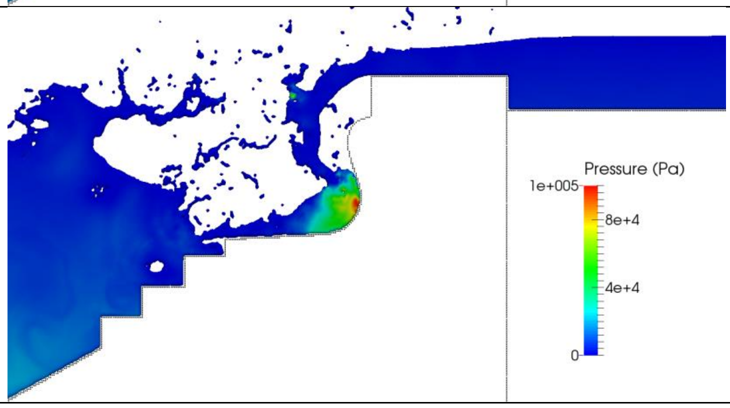	Time = 50.1 sec Timestep = 501 Maximum pressure at probes: P11 (192.67 kPa) and P12 (166.86 kPa)

3	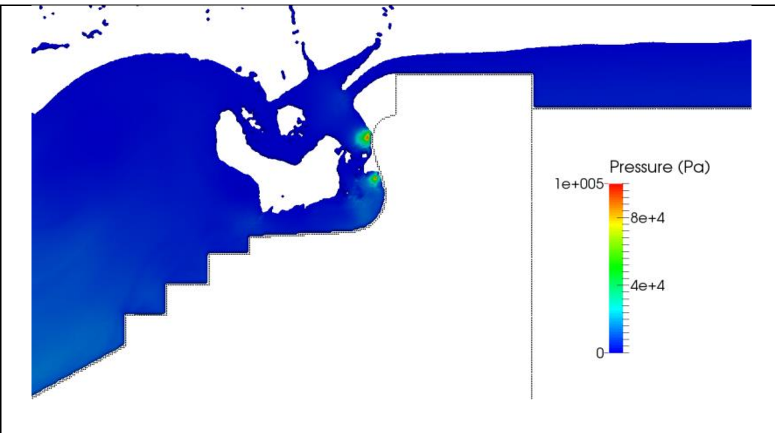	Time = 61.7 sec Timestep = 617 Maximum pressure at probes: P8 (194.20 kPa)
4	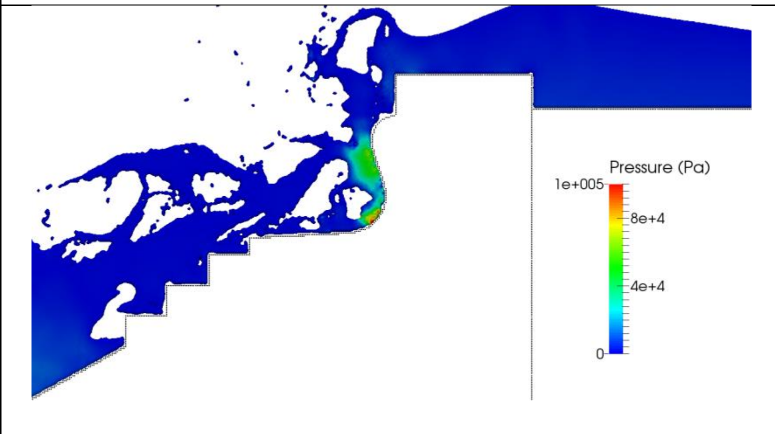	Time = 69.3 sec Timestep = 693 Maximum pressure at probes: P7 (141.89 kPa)
5	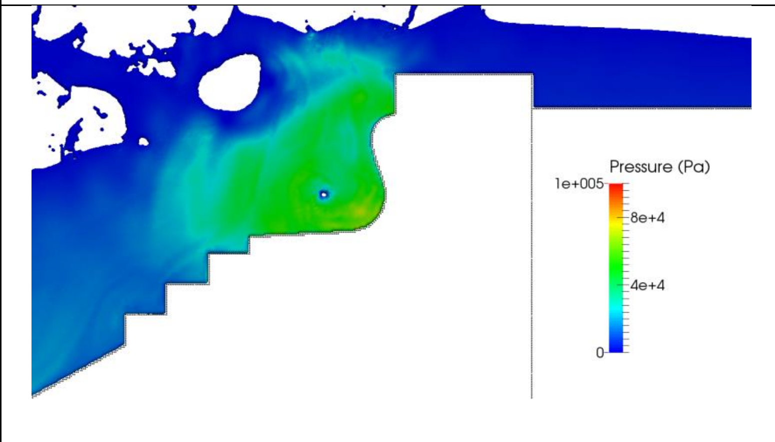	Time = 70.4 sec Timestep = 704 Maximum pressure at probes: P1 (72.58 kPa) P2 (108.12 kPa) P3 (126.85 kPa) P4 (105.23 kPa) P5 (90.59 kPa) and P13 (156.86 kPa)
6	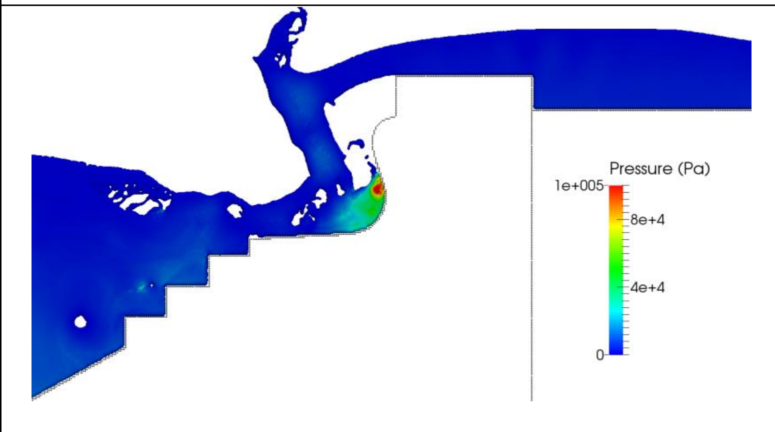	Time = 89.8 sec Timestep = 898 Maximum pressure at probes: P10 (334.58 kPa)/highest

So far, the storm wave has been approximated as a series of regular waves with constant period and wave height. In reality, the waves occurring during the storm are random, and are better represented as a time series. The results from a model for which the paddle motions were based on incident waves determined using a SWAN model analysis is shown in Figure 7.11. The incident wave was at Anchorsholme, about 50 m from the toe of the seawall. The SWAN model was run from the wave buoy to the shore with an output at a location about 1000 m from the shore (bed level = - 7.038 mOD). The spectrum that was used from 12:06pm (*Hm0* = 4.62m, T_p = 9.1s), with a water level based on the maximum at Liverpool (max level = 6.218m, estimated timing halfway between max. water levels at Heysham and Liverpool = 12:15pm). The paddle motion time series consisted of about 1000 sec of waves. The impact pressures on recurve wall obtained from incident waves determined using SWAN are smaller compared with the impact pressure shown in Figure 7.8 through Figure 7.10.

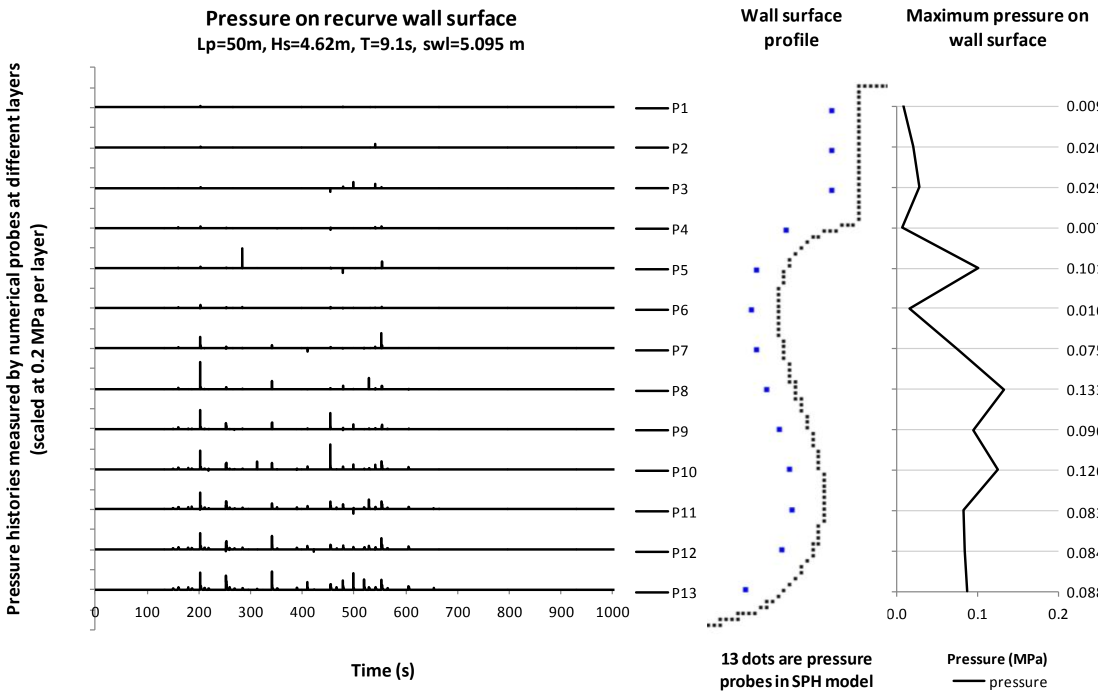

Figure 7.11 Pressure distribution from a simulation that the paddle motion is based on SWAN analysis.

7.4 Concluding Remarks

Numerical modelling using SPH has been undertaken to simulate storm waves generated via a paddle wavemaker. The intention for conducting the modelling in this chapter was to find out the maximum wave pressure that is likely to have occurred during a real life storm event that resulted in damage to a recurve wall. From the models investigated, maximum impact pressures around 200 kN/m^2 were observed, this magnitude being commensurate with the observed structural damage in-the-field. Such correlation underscores the capability of the method in modelling impulsive storm wave impacts. However, to achieve more accurate predictions, this method needs to be improved especially regarding the effect of reflective waves that join the oncoming waves and the associated complex interaction. The SPH model has also been used to generate a series of waves from the motion of the paddle based on SWAN analysis and this gave lower pressure predictions than the uniform wave paddle motion, this requires further investigation.

Chapter 8

Conclusion and Future Work

8.1 General Conclusions

A new method to simulate the interaction of tsunami-like bores and coastal structures is needed to improve present coastal engineering design practice with regard to tsunamis. Currently there is no method available that is capable of simulating in detail the complex wave structure interactions resulting from tsunami bore impacts. The sudden increase in transient tsunami bore pressure-time history affects the behaviour of coastal structures differently from current design practice that uses equations based on representing the impacting tsunami load as a quasi-static load.

The novelty in the research presented in this thesis is the use of a methodology that couples a full 3-D fluid simulation via SPH and a structural response model using the FE package ABAQUS. The phenomena associated with tsunami-like bores and coastal structure interaction including the transient bore impact, the random distribution of bore impact pressure, the location of maximum/peak impact pressure, the coastal structure behaviour in terms of deflection and stress distribution, are capable of being described in great detail using this methodology.

The thesis has shown that the resilience of coastal structures can be improved by simply changing the orientation of the structure relative to the direction of the incoming tsunami-like wave. The changing of the orientation of the structure reduced the force exerted on the structure's vertical surface significantly.

Furthermore, the SPH simulations showed that SPH can be used to investigate the shielding and focusing effects in tsunami events by involving a group of structures in different arrangements and orientations. The results show that the pressures exerted on structures have a strong dependence on their relative orientations and distance between adjacent structures where the fluid flowed. These findings are in good agreement with the performance of structures observed in the field.

The finite element modelling using ABAQUS shows the capability of the method to be exercised to obtain the response of timber structures under transient loading. ABAQUS can be used successfully as a coupled method for the SPH-based software DualSPHysics.

8.2 Detailed Conclusion

8.2.1 Improvement for current design practice

Current research examining the interaction of tsunami bores with land-based onshore coastal structures is limited to a relatively small number of experimental and numerical investigations. The research presented in this thesis used SPH to simulate solitary waves to represent tsunami-like waves that propagate from offshore along a water tank and then forming a bore at the shore line which impacts an onshore structure. The tsunami-like bore impact pressure-time histories show sudden pressure increase of short time duration. On the other hand, current design practices used quasi-static loads to represent tsunami-induced hydrodynamic loads acting on the structure. Comparison has been made for predicting the tsunami bore impact pressure based on current design equations and 2-D SPH simulations. The design codes that are used for comparison include the City and County of Honolulu code (CCH, 2000). Parameter values that are considered for the comparison include the velocity and height of incoming bore and also the velocity and height of reflective bore after impact. The comparison results show that the design codes predict either higher or lower values than the SPH prediction. The load characteristics indeed affect the overall performance of structures. Pressure predictions for an equivalent bore height based on a code (CCH, 2000) and the SPH model have been applied as an input load on a timber structure modelled by ABAQUS as shown in section 6.3.3. The results of structural analysis using ABAQUS shows that the timber house components received maximum stresses of almost one order of magnitude less when loaded by the quasi-static load compared with the SPH transient pressures. The potential for poor design using existing quasi-static approaches is therefore clear.

8.2.2 The coupled methods of DualSPHysics and ABAQUS

The methodology used in this research coupled DualSPHysics and ABAQUS to provide a comprehensive analysis from the generation of tsunami-like waves to the response of the structure impacted by the tsunami-induced bore. This one-way coupling method relates the output pressure gained from the DualSPHysics model to be used as an input pressure in the ABAQUS model. One of the key aspects in this method is the application of the same size for pressure probe spacing in the DualSPHysics model with the size of mesh in the ABAQUS model. Using the same particle and mesh size enables the pressure value from DualSPHysics to be applied directly to the ABAQUS model. The DualSPHysics model enables provision of detailed pressure prediction through 2-D and 3-D models. The 2-D model can be performed to simplify a non-discrete model of a coastal structure such as a linear coastal defence. The 3-D model can be utilised to model discrete structures such as a coastal timber house. The advantages of performing DualSPHysics modelling over standard design codes hence includes the capability to obtain bore pressure-time history at any desired location on the surface of structure. Moreover, the location of peak pressure also can be tracked and this information is important to predict the location of potential failure of a structure during the impact events. The detail of the pressures distribution and magnitude from DualSPHysics outputs are valuable for conducting finite element modelling using ABAQUS. The results of hydrodynamic modelling using DualSPHysics and the structural modelling using ABAQUS in

Chapter 3 and Chapter 5, respectively, showed the advantage of 3-D fluid modelling of violent free-surface flow and structural response.

8.2.3 Improving resilience of coastal structures

Improvement in the resilience of coastal structures is essential as parts of the new strategy to survive tsunami-induced loads and reduce fatalities. This thesis has shown that a simple way to reduce the total stress exerted on the surfaces of a structure is by changing the orientation of the structure. The total pressure exerted on the surfaces of a structure can be reduced significantly up to 50% by rotating the structure relative to the incoming wave direction. The bigger the angle of structure orientation, the higher the reduction of the total force acting on its vertical surface. These results were obtained from 3-D simulations of a water tank with a simple discrete structure treated as a cube with dimension of 1 m. The degree orientations for the structure were 0°, 30°, 45° and 60°. The bore was generated by the solitary wave with $H/h_0 = 0.1$, 0.3 and 0.5.

8.2.4 The shielding and focusing effect simulations

The field studies reviewed in Chapter 2 show clear evidence of the shielding and focusing effects playing an important role in influencing the damage of coastal structures in the tsunami events. In developed shore-based communities, the tsunami-induced bore flows among a group of structures and it is therefore of great interest to investigate shielding and focussing along with the associated pressure acting on the structures. In the present research using DualSPHysics, the shielding and focusing effects have been simulated involving multiple structures with a different arrangement. The thesis investigated two structures located at the front to provide shielding and at the same time the bore flows between the gaps of the front structures were shown to provide focusing effects for the rear structure. Simulations for different orientations of multiple structures demonstrated that the pressure exerted on the rear structure depends strongly on the size of the gaps of the front structures that caused the focusing effect. More research is clearly needed here to identify optimal arrangements.

8.3 Limitation of the research

The limitations of the research presented in this thesis are:

- An idealised coastal structure of a cube with dimension of 1 m x 1 m x 1 m is used in the 3-D parametric simulations in this thesis for the reason of simplicity and to non-dimensionalise the analysis output values. Variations of the shape and dimension of idealised coastal structures are needed to capture the complex fluid-structure interaction that depends strongly on the geometry of structures.
- The DualSPHysics software used for all SPH simulations in this thesis is still a single-phase model. Therefore, in the models the role of air in the tsunami-induced bores cannot be included. Future versions of the DualSPHysics software will incorporate multi-phase formulations so that the SPH particles can be modelled as water and air.
- The one-way coupling method applied in this research can only use the pressure-time history from the SPH model to be applied on the finite element models just once. The materials of the loaded structure are still in their elastic condition and therefore the structure deforms during the loading and can influence back the fluid particles that impact it. With one-way coupling method, this reciprocal interaction cannot be examined.

8.4 Recommendations for future research

It is recommended that further research be undertaken in the following areas:

- In the 3-D simulations in this thesis, the tsunami-induced bores developed at shorelines directly impacted onshore idealised coastal structures that were assumed as residential houses. However, in several coastal areas that were affected by tsunamis, coastal defences were in evidence, built in different forms including submerged breakwaters in offshore coastal areas and vertical sea walls located at onshore coastal areas. Further studies regarding the tsunami bores impact modelling with the presence of coastal defences seaward of the residential structures would be worthwhile.

- This thesis only examined very simple arrangements of multiple structures and shielding effects. There is considerable scope for more comprehensive investigations to suggest optimal arrangements of structures.
- Despite the advantages of the GPU acceleration of the simulations, it is possible that some simulations could benefit from finer resolution in the vicinity of the structure which could be achieved using variable resolution SPH (Vacondio *et al*., 2015) or a multi-GPU code (Domínguez *et al*., 2013).
- The role of air is complex in violent breaking wave impacts (Bredmose *et al*., 2009). A substantial volume of air may well be trapped between the water and structure against during the impact and this may cause high pressure in the impact zone leading to a localized damaged to the structure. The role of air in the simulation of tsunami-induced bores using SPH is an intriguing one which could be usefully explored in further research.
- In tsunami events some buildings collapsed because of scouring at the foundations. The scouring that removes the soils supporting the buildings could occur at the time when incoming bores inundate the onshore side and also when the water recedes back to the sea. At the same time when the building submerged during the inundation with entrapped air inside it, the buoyancy effect will be active and can cause the buildings being uplifted from the ground. Further research needs to examine the effects of scouring and buoyancy during the tsunami-bore inundation.
- The existence of openings or break-away walls on the surface of buildings can reduce the total force exerted on it as shown by Lukkunaprasit *et al*. (2009). Further study could assess the influence of openings on the surface of buildings as an alternative to improve the resilience of coastal structures.
- The residential buildings built in the tsunami prone coastal areas vary in shape, sizes and materials. It is suggested that the association of these variations is investigated in future studies.
- The impact of floating debris such as floating building remains, fishing boats and cars have caused fatal failures during tsunami events including column failures near the mid height of coastal buildings. The debris impact generated pressure can be higher than the tsunami wave pressure (Saatcioglu *et al*., 2005). Another

possible area of future research would be to investigate the effect of debris impact pressure on coastal buildings.

References

Abadie, S. M., Harris, J. C., Grilli, S. T., & Fabre, R. (2012). Numerical modeling of tsunami waves generated by the flank collapse of the Cumbre Vieja Volcano (La Palma, Canary Islands): tsunami source and near field effects. *J. Geophys. Res*, *117*, C05030.

Abadie, S. M., Morichon, D., Grilli, S. T., & Glockner, S. (2010). Numerical simulation of waves generated by landslides using a multiple-fluid Navier–Stokes model. *Coast. Eng*, *57*, 779–794.

ABAQUS. (2010). *ABAQUS analysis user's manual.* Providence, Rhode Island, USA., SIMULIA, Dassault Systèmes.

Ali, R. M. M., & Louca, L. A. (2008). Performance-based design of blast resistant offshore topsides, Part II: Modelling and design. *Journal of Constructional Steel Research*, *64*, 1046–1058.

Al-Thairy, H. A. B. (2012). *Behaviour and design of steel columns subjected to vehicle impact*. PhD Thesis, University of Manchester.

Altomare, C., Crespo, A. J. C., Domínguez, J. M., Gómez-Gesteira, M., Suzuki, T., & Verwaest, T. (2015). Applicability of Smoothed Particle Hydrodynamics for estimation of sea wave impact on coastal structures. *Coastal Engineering*, *96*, 1–12.

Arnason, H. (2005). *Interactions between an Incident Bore and a Free-Standing Coastal Structure*. PhD thesis, Department of Civil and Environmental Engineering, University of Washington.

Arnason, H., Petroff, C., & Yeh, H. (2009). Tsunami Bore Impingement onto a Vertical Column. *Journal of Disaster Research*, *4*, 391–403.

Asakura, R., Iwase, K., Ikeya, T., Takao, M., Kaneto, K., Fujii, N., & Omori, M. (2000). An Experimental Study on Wave Force Acting on On-Shore Structures Due to Overflowing Tsunamis. *Proc. Coastal Eng*, *47*, 911–915 (in Japanese).

ASTM-D1761-06. (2008). *Annual book of ASTM standards–standard test methods for mechanical fasteners in wood*. ASTM International.

Bader, M., Böck, C., Schwaiger, J., & Vigh, C. A. (2010). Dynamically adaptive simulations withminimal memory requirement-solving the shallow water equations using Sierpinski curves. *SIAM J. Sci. Comput*, *32*, 212–228.

Bambach, M. R. (2008). Behaviour and design of aluminium hollow sections subjected to transverse blast loads. *Thin-Walled Structures*, *46*, 1370–1381.

Bambach, M. R., Jama, H., Zhao, X. L., & Grzebieta, R. H. (2008). Hollow and concrete filled steel hollow sections under transverse impact loads. *Engineering Structures*, *30*, 2859–2870.

Barreiro, A., Crespo, A. J. C., Domínguez, J. M., & Gómez-Gesteira, M. (2013). Smoothed Particle Hydrodynamics for coastal engineering problems. *Computers & Structures*, *120*, 96–106.

Becker, A. B., Johnstone, W. M., & Lence, B. J. (2011). Wood frame building response to rapid-onset flooding. *Natural Hazards Review*, *12*(2), 85–95.

Behrens, J., & Dias, F. (2015). New computational methods in tsunami science. *Philosophical Transactions of the Royal Society A: Mathematical, Physical and Engineering Sciences*, *373*.

Boh, J. W., Louca, L. A., & Choo, Y. S. (2004). Numerical assessment of explosion resistant profiled barriers. *Marine Structures*, *17*, 139–160.

Bonorchis, D., & Nurick, G. N. (2009). The influence of boundary conditions on the loading of rectangular plates subjected to localised blast loading - Importance in numerical simulations. *International Journal of Impact Engineering*, *36*, 40–52.

Børvik, T., Hanssen, A. G., Langseth, M., & Olovsson, L. (2009). Response of structures to planar blast loads – A finite element engineering approach. *Computers & Structures*, *87*, 507–520.

Bredmose, H., Peregrine, D. H., & Bullock, G. N. (2009). Violent breaking wave impacts. Part 2: modelling the effect of air. *Journal of Fluid Mechanics*, *641*, 389.

Canelas, R., Ferreira, R. M. L., Crespo, A. J. C., & Domínguez, J. M. (2013). A generalized SPH-DEM discretization for the modelling of complex multiphasic free surface flows. In *Proceedings of the 8th International SPHERIC Workshop* (p. 6). Trondheim, Norway.

Castro, C. E., Behrens, J., & Pelties, C. (2013). CUDA-C implementation of the ADER-DG method for linear hyperbolic PDEs. *Geosci. Model Dev. Discuss*, *6*, 3743–3786.

CCBFC. (1995). *National Building Code of Canada 1995*. Canadian Commission on Building and Fire Codes, National Research Council Canada, Ottawa, Canada.

CCH. (2000). *City and County of Honolulu Building Code (CCH)*. Chapter 16, Article 11. Department of Planning and Permitting of Honolulu Hawaii, Honolulu, HI.

Chock, G., Robertson, I., Carden, L., & Yu, G. (2012). Tohoku Tsunami-Induced Building Damage Analysis Including the Contribution of Earthquake Resistant design to Tsunami Resilience of Multi-Story Buildings. *Proceedings of the International Symposium on Engineering Lessons Learned from the 2011 Great East Japan Earthquake*, 492–503.

Chock, G. Y. K., Robertson, I., & Riggs, H. R. (2011). Tsunami structural design rovisions for a new update of building codes and performance-based engineering. *Solution to Coastal Disasters*, 423–435.

Clubley, S. K. (2014). Non-linear long duration blast loading of cylindrical shell structures. *Engineering Structures*, *59*, 113–126. Retrieved from http://linkinghub.elsevier.com/retrieve/pii/S0141029613004999\nhttp://www.sciencedirect.com/science/article/pii/S0141029613004999

Como, A., & Mahmoud, H. (2013). Numerical evaluation of tsunami debris impact loading on wooden structural walls. *Engineering Structures*, *56*, 1249–1261. Retrieved from http://dx.doi.org/10.1016/j.engstruct.2013.06.023.

Crespo, A. J. C., Dominguez, J. M., Barreiro, A., Gómez-Gesteira, M., & Rogers, B. D. (2011). GPUs, a new tool of acceleration in CFD: Efficiency and reliability on smoothed particle hydrodynamics methods. *PLoS ONE*, *6*(6).

Crespo, A. J. C., Dominguez, J. M., Gesteira, M. G., Barreiro, A., Rogers, B. D., Longshaw, S., … Vacondio, R. (2013). *User Guide for DualSPHysics code v3.0*.

Crespo, A. J. C., Domínguez, J. M., Rogers, B. D., Gómez-Gesteira, M., Longshaw, S., Canelas, R., … García-Feal, O. (2015). DualSPHysics: Open-source parallel CFD solver based on Smoothed Particle Hydrodynamics (SPH). *Computer Physics Communications*, *187*, 204–216.

Crespo, A. J. C., Gomez-Gesteira, M., & Dalrymple, R. A. (2007). Boundary conditions generated by dynamic particles in SPH methods. *Cmc-Computers Materials & Continua*, *5*, 173–184.

Cross, R. H. (1967). Tsunami surge forces. *Journal of Waterways and Harbor Division, ASCE, 93*(4), 201–231.

Cumberbatch, E. (1960). The Impact of A Water Wedge on A Wall. *Journal of Fluid Mechanics*, *7*, 353–374.

Cunningham, L. S. (2014). Communication with Blackpool Council regarding storm damage in Anchorsholme. University of Manchester, School of Mechanical, Aerospace and Civil Engineering.

Cunningham, L. S., Rogers, B. D., & Pringgana, G. (2014). Tsunami wave and structure interaction: an investigation with smoothed-particle hydrodynamics. *ICE Journal of Engineering and Computational Mechanics*, *167*(EM3), 126–138.

Dalrymple, R. A., Gómez-Gesteira, M., Rogers, B. D., Panizzo, A., Zou, S., Crespo, A. J. C., … Narayanaswamy, M. (2009). *Smoothed particle hydrodynamics for water waves*. in Advances in numerical simulation of nonlinear water waves, ed. Ma, Q., Singapore: World Scientific Publishing.

Dalrymple, R. A., & Rogers, B. D. (2006). Numerical modeling of water waves with the SPH method. *Coastal Engineering*, *53*, 141–147.

Dean, R. G., & Dalrymple, R. A. (1991). *Water wave mechanics for engineers and scientist*. Singapore: World Scientific.

Domínguez, J. M., Crespo, A. J. C., Barreiro, A., Gómez-Gesteira, M., & Mayrhofer, A. (2011). Development of a new pre-processing tool for SPH models with complex geometries. In: Schriftenreihe Schiffbau 6th SPHERIC, Edited by Hamburg

University of Technology, 117–124.

Domínguez, J. M., Crespo, A. J. C., Valdez-Balderas, D., Rogers, B. D., & Gómez-Gesteira, M. (2013). New multi-GPU implementation for Smoothed Particle Hydrodynamics on heterogeneous clusters. *Computer Physics Communications*, *184*, 1848–1860.

Dorogoy, A., & Rittel, D. (2008). Transverse impact of free-free square aluminum beams: An experimental-numerical investigation. *International Journal of Impact Engineering*, *35*, 569–577.

Drazin, P. G., & Johnson, R. S. (1989). Solitons: An Introduction.

Dutykh, D., Poncet, R., & Dias, F. (2011). The VOLNA code for the numerical modeling of tsunami waves: generation, propagation and inundation. *Eur. J. Mech. B/Fluids*, *30*, 598–615.

EERI. (2010). Samoa Earthquake and Tsunami of September 29, 2009. *Earthquake Engineering Research Institute (EERI) Special Earthquake Report*, 1–8.

EERI. (2011). The Tohoku, Japan, Tsunami of March 11, 2011: Effects on Structures. *Earthquake Engineering Research Institute (EERI) Special Earthquake Report*, 1–14.

El-Solh, S. (2012). *SPH Modeling of Solitary Waves and Resulting Hydrodynamic Forces on Vertical and Sloping Walls*. *Department of Civil Engineering*. University of Ottawa, Ottawa.

Esteban, M., Thao, N. D., Takagi, H., & Shibayama, T. (2009). Pressure exerted by a solitary wave on the rubble mound foundation of an armoured caisson breakwater. In *Proceedings of the 19th International Offshore and Polar Engineering Conference*. Osaka.

FEMA. (2008). *Design of Structures for Vertical Evacuation from Tsunamis*. Federal Emergency Management Agency (FEMA), P-646.

FEMA (Federal Emergency Management Agency). (2011). *Coastal Construction Manual*. *FEMA P-55* (Vol. II). Washington, DC, USA.

Fraser, S., Raby, A., Pomonis, A., Goda, K., Chian, S. C., Macabuag, J., … Sammonds,

P. (2013). Tsunami Damage to Coastal Defences and Buildings in The March 11th 2011 Mw9.0 Great East Japan Earthquake and Tsunami. *Bull. Earthquake Eng.*, *11*, 205–239.

Fujima, K., Achmad, F., Shigihara, Y., & Mizutani, N. (2009). A Study on Estimation of Tsunami Force Acting on Structures. *Journal of Disaster Research*, *4*(6), 404–409.

Gailler, A., Hébert, H., Loevenbruck, A., & Hernandez, B. (2013). Simulation systems for tsunami wave propagation forecasting within the French tsunami warning system. *Nat. Hazards Earth Syst. Sci.*, *13*, 2465–2482.

Galvin, C. J. J. (1964). *Wave-height prediction for wave generators in shallow water*. Tech Memo 4, U. S. Army, Coastal Engineering Research Centre, March.

George, D. L., & LeVeque, R. L. (2006). Finite volume methods and adaptive refinement for global tsunami propagation and local inundation. *Sci. Tsunami Hazards*, *24*, 319–328.

Ghobarah, A., Saatcioglu, M., & Nistor, I. (2006). The Impact of the 26 December 2004 Earthquake and Tsunami on Structures and Infrastructure. *Engineering Structures*, *28*, 312–326.

Gisler, G. R., Weaver, R., & Gittings, M. L. (2006). SAGE calculations of the tsunami threat from La Palma. *Sci. Tsunami Hazards*, *24*, 288–301.

Gisler, G. R., Weaver, R., Mader, C. L., & Gittings, M. L. (2004). Two- and three-dimensional asteroid impact simulations. *Comput. Sci. Eng*, *6*, 46–55.

Gomez-Gesteira, M., Crespo, A. J. C., Rogers, B. D., Dalrymple, R. A., Dominguez, J. M., & Barreiro, A. (2012). SPHysics - development of a free-surface fluid solver - Part 2: Efficiency and test cases. *Computers and Geosciences*, *48*(2), 300–307.

Gomez-Gesteira, M., Rogers, B. D., Crespo, A. J. C., Dalrymple, R. A., Narayanaswamy, M., & Dominguez, J. M. (2012). SPHysics – development of a free-surface fluid solver – Part 1: Theory and formulations. *Computers & Geosciences*, *48*(1), 289–299.

Gómez-Gesteira, M., Rogers, B. D., Dalrymple, R. A., Crespo, A. J. C., &

Narayanaswamy, M. (2010). *User guide for the SPHysics code v2.0.* (http://www.sphysics.org).

Goring, D. G. (1978). Tsunamis - The Propagation of Long Wave onto A Shelf. Report Kh-R-38,.

Harada, T., Koshizuka, S., & Kawaguchi, Y. (2007). Smotthed Particle Hydrodynamics on GPUs. *Proc of Comp Graph Inter*, 63–70.

Harig, S., Chaeroni, X., Pranowo, W. S., & Behrens, J. (2008). Tsunami simulations on several scales: comparison of approaches with unstructured meshes and nested grids. *Ocean Dyn*, *58*, 429–440.

Hébert, H., Burg, P. E., Binet, R., Lavigne, F., Allgeyer, S., & Schindelé, F. (2012). The 2006 July 17 Java (Indonesia) tsunami from satellite imagery and numerical modelling: a single or complex source? *Geophys. J. Int*, *191*, 1255–1271.

Hiroi, I. (1919). A Formula for evaluating breaking wave pressure intensity in the case of breaking waves. *Journal of the College of Engineering, Tokyo Imperial University, Tokyo, Japan*, 11–21.

Hsiao, S.-C., & Lin, T.-C. (2010). Tsunami-like Solitary Waves Impinging and Overtopping An Impermeable Seawall: Experiment and RANS Modelling. *Coastal Engineering*, *57*, 1–18.

Iemura, H., Pradono, M. H., & Takahashi, Y. (2005). Report on the Tsunami Damage of Bridges in Banda Aceh and Some Possible Countermeasures. *Proc. 28th JSCE Earthquake Engineering Symposium*, 1–10.

Imamura, F., Yalciner, A. C., & Ozyurt, G. (2006). Tsunami modelling manual.

International Code Council. (2009). *2009 International residential code for one- and two-family dwellings*. Country Club Hills, IL.

Jacinto, A. C., Ambrosini, R. D., & Danesi, R. F. (2002). Dynamic response of plates subjected to blast loading. *Proceedings of the ICE - Structures and Buildings*, *152*(3), 269–276.

Jacob, N., Nurick, G. N., & Langdon, G. S. (2007). The effect of stand-off distance on the failure of fully clamped circular mild steel plates subjected to blast loads.

Engineering Structures, *29*, 2723–2736.

Johnson, G. R., Stryk, R. A., & Beissel, S. R. (1996). SPH for high velocity impact computations. *Computer Methods in Applied Mechanics and Engineering*, *139*(1-4), 347–373.

Johnson, K. L. (1985). Contact Mechanics. Cambridge.

Johnson, W. (1972). *Impact Strength of Material*.

Kawashima, K., Kosa, K., Takahashi, Y., Akiyama, M., Nishioka, T., Watanabe, G., … Matsuzaki, H. (2011). Damage of Bridges during 2011 Great East Japan Earthquake. *Proceedings of 43rd Joint Meeting, US-Japan Panel on Wind and Seismic Effects*.

Kennedy, A. B., Chen, Q., Kirby, J. T., & Dalrymple, R. A. (2000). Boussinesq modeling of wave transformation, breaking, and runup, part I: 1D. *J. Waterw. Port Coast. Ocean Eng*, *126*, 39–47.

Kleefsman, K. M. T., Fekken, G., Veldman, A. E. P., Iwanowski, B., & Buchner, B. (2005). A Volume-of-Fluid based simulation method for wave impact problems. *Journal of Computational Physics*, *206*, 363–393.

Kumar, N., Dayal, V., & Sarkar, P. P. (2012). Failure of wood-framed low-rise buildings under tornado wind loads. *Engineering Structures*, *39*, 79–88. http://doi.org/10.1016/j.engstruct.2012.02.011

Leal, J. G. A. B., Ferreira, R. M. L., & Cardoso, A. H. (2006). Dam-break wave-front celerity. *Journal of Hydraulic Engineering*, *132*(1), 69–76.

Lee, E. S., Violeau, D., & Issa, R. (2010). Application of Weakly Compressible and Truly Incompressible SPH to 3-D Water Collapse in Waterworks. *Journal of Hydraulic Research*, *48*, 50–60.

Leimkuhler, B. J., Reich, S., & Skeel, R. D. (1996). Integration Methods for Molecular dynamic IMA Volume in Mathematics and its application. *Springer*.

Li, Y., & Raichlen, F. (2001). Solitary Wave Runup on Plane Slopes. *Journal of Waterway, Port, Coastal, and Ocean Engineering*, *127*, 33–44.

Lind, S. J., Stansby, P. K., Rogers, B. D., & Lloyd, P. M. (2015). Numerical predictions of water–air wave slam using incompressible–compressible smoothed particle hydrodynamics. *Applied Ocean Research*, *49*, 57–71.

Lind, S. J., Xu, R., Stansby, P. K., & Rogers, B. D. (2012). Incompressible smoothed particle hydrodynamics for free-surface flows: A generalised diffusion-based algorithm for stability and validations for impulsive flows and propagating waves. *Journal of Computational Physics*, *231*(4), 1499–1523.

Linton, D., Gupta, R., Cox, D., van de Lindt, J., Oshnack, M. E., & Clauson, M. (2013). Evaluation of Tsunami Loads on Wood Frame Walls at Full Scale. *Journal of Structural Engineering*, *139*(8), 1318–1325.

Louca, L. A., Boh, J. W., & Choo, Y. S. (2004). Design and analysis of stainless steel profiled blast barriers. *Journal of Constructional Steel Research*, *60*(12), 1699–1723.

Lukkunaprasit, P., Ruangrassamee, A., & Thanasisathit, N. (2009). Tsunami Loading on Buildings with Openings. *Journal of Tsunami Society International*, *28*(5), 303–310.

Madsen, P. A. (2010). On the Evolution and Run-up of Tsunamis. *Journal of Hydrodynamics*, *22*, 1–6.

Madsen, P. A., & Fuhrman, D. R. (2007). Analytical and Numerical Models for Tsunami Run-up. In A. Kundu (Ed.), *Tsunami and Non-Linear Waves* (pp. pp. 209–236). Berlin: Springer.

Madsen, P. A., Fuhrman, D. R., & Schaffer, H. A. (2008). On the Solitary Wave Paradigm for Tsunamis. *Journal of Geophysical Research*, *113*, 1–22.

Madsen, P. A., & Schaffer, H. A. (2010). Analytical Solutions for Tsunami Runup on A Plane Beach: Single Waves, N-Waves and Transient Waves. *Journal of Fluid Mechanics*, *645*, 27–57.

McCormick, M. E. (2010). *Ocean engineering mechanics with applications*. Cambridge University Press.

McGranahan, G., Balk, D., & Anderson, B. (2007). The rising tide: assessing the risk of climate change and human settlement in low elevation coastal zones. *Environment and Urbanization*, *19*, 17–37.

Mikami, T., Shibayama, T., & Esteban, M. (2012). Field Survey of the 2011 Tohoku Earthquake and Tsunami in Miyagi and Fukushima Prefectures. *Coastal Engineering Journal*, *54*, 1–26.

Mishnaevsky, L. J., & Schmauder, S. (2001). Continuum mesomechanical finite element modeling in materials development: a state-of-the-art review. *Applied Mechanics Reviews*, *54*(1), 49–69.

Mokos, A., Rogers, B. D., Stansby, P. K., & Domínguez, J. M. (2015). Multi-phase SPH modelling of violent hydrodynamics on GPUs. *Computer Physics Communications*, *196*, 304–316.

Monaghan, J. J. (1989). On the problem of penetration in particle methods. *Journal of Computational Physics*, *82*(1), 1–15.

Monaghan, J. J. (1992). Smoothed particle hydrodynamics. *Ann. Rev. Astron. Astrophys.*, *30*, 543–574.

Monaghan, J. J. (2005). Smoothed particle hydrodynamics. *Reports on Progress in Physics*, *68*, 1703–1759.

Monaghan, J. J., & Kos, A. (1999). Solitary waves on a Cretan beach. *Journal of Waterways, Port and Coastal Engineering*, *125*(3), 145–154.

Moore-Concrete. (2015). Wave Walls. Retrieved from www.moore-concrete.com/wave-walls-shetland/

Nistor, I., Palermo, D., Cornett, A., & Al-Faesly, T. (2010). Experimental and Numerical Modeling of Tsunami Loading on Structures. In *The 32nd International Conference on Coastal Engineering, ASCE* (pp. 1–14). Shanghai, China.

Nistor, I., Palermo, Y. N., Murty, T., & Saatcioglu, M. (2000). Coastal Structures: Tsunami-Induced Forces on Structures. In Y. C. Kim (Ed.), *Handbook of Coastal and Ocean Engineering* (1st Editio, pp. pp. 261–286). Singapore: World Scientific.

Nistor, I., Saatcioglu, M., & Ghobarah, A. (2005). The 26 December 2004 Earthquake and Tsunami - Hydrodynamics Forces on Physical Infrastructure in Thailand and

Indonesia. *Proc. 2005 Canadian Coastal Engineering Conference*, 15.

Nouri, Y., Nistor, I., Palermo, D., & Cornett, A. (2010). Experimental Investigation of Tsunami Impact on Free Standing Structures. *Coastal Engineering Journal*, *52*, 43–70.

OCADI. (2009). *Technical Standards and Commentaries for Port and Harbour Facilities in Japan*. The Overseas Coastal Area Development Institute of Japan, Ports and Harbours Bureau, Tokyo, Japan.

Okada, T., Sugano, T., Ishikawa, T., Ohgi, T., Takai, S., & Hamabe, C. (2005). *Structural design methods of buildings for tsunami resistance (SMBTR)*. The Building Center of Japan, Japan.

Papadopoulos, G. A., & Fokaefs, A. (2005). Strong Tsunamis in the Mediterranean Sea: A Re-Evaluation. *ISET Journal of Earthquake Technology*, *42*, 159–170.

Parshikov, A. N. (1999). Application of a solution of the Riemann problem to the SPH method. *Computational Mathematics and Mathematical Physics, 39*.

Pedersen, G., & Løvholt, F. (2008). *Documentation of a global Boussinesq solver*. *Preprint series in Applied Mathematics 1*. Department of Mathematics, University of Oslo, Norway. Retrieved from http://urn.nb.no/URN:NBN:no-27775

Pranowo, W. S., Behrens, J., Schlicht, J., & Ziemer, C. (2008). Adaptive mesh refinement applied to tsunami modeling: TsunaFLASH. In Adrianto (Ed.), *In Proc. Int. Conf. on Tsunami Warning*. Jakarta, Indonesia: State Ministry of Research and Technology, Republic of Indonesia (RISTEK).

Rakowsky, N., Androsov, A., Fuchs, A., Harig, S., Immerz, A., Danilov, S., … Schröter, J. (2013). Operational tsunami modelling with TsunAWI - recent developments and applications. *Nat. Hazards Earth Syst. Sci*, *13*, 1629–1642.

Ramsden, J. (1993). *Tsunamis: Forces on A Vertical Wall Caused by Long Waves, Bores and Surges on A Dry Bed*. PhD thesis, California Institute of Technology, Pasadena.

Ramsden, J. D. (1996). Forces on A Vertical Wall due to Long Waves, Bores, and Dry-Bed Surges. *Journal of Waterway, Port, Coastal, and Ocean Engineering*, *122*, 134–141.

Ramsden, J. D., & Raichlen, F. (1990). Forces on Vertical Wall Caused by Incident Bores. *Journal of Waterway, Port, Coastal, and Ocean Engineering, 116*, 592–613.

Reymond, D., Okal, E. A., Hébert, H., & Bourdet, M. (2012). Rapid forecast of tsunami wave heights from a database of pre-computed simulations, and application during the 2011 Tohoku tsunami in French Polynesia. *Geophysical Research Letters*, *39*, L11603.

Robertson, I. N., Paczkowski, K., Riggs, H. R., & Mohamed, A. (2013). Experimental investigation of tsunami bore forces on vertical walls. *Journal of Offshore Mechanics and Arctic Engineering*, *135*, 21601.

Robertson, I. N., Riggs, H. R., Paczkowski, K., & Mohamed, A. (2011). Tsunami bore forces on walls. In *Proceedings of the ASME 2011, 30th International Conference on Ocean, Offshore and Arctic Engineering* (pp. 1–9). Rotterdam, The Netherlands.

Robertson, I. N., Riggs, H. R., Yim, S. C. S., & Young, Y. L. (2007). Lessons from Hurricane Katrina Storm Surge on Bridges and Buildings. *Journal of Waterway, Port, Coastal, and Ocean Engineering*, *133*, 463–483.

Rogers, B. D., & Dalrymple, R. (2008). SPH modeling of tsunami waves. In P. Liu (Ed.), *Advanced Numerical Models for Tsunami Waves and Runup* (pp. 75–100). Singapore: World Scientific.

Saatcioglu, M. (2009). Performance of Structures During the 2004 Indian Ocean Tsunami and Tsunami Induced Forces for Structural Design. In A. T. Tankut (Ed.), *Earthquakes and Tsunamis: Geotechnical, Geological, and Earthquake Engineering* (1st Editio, Vol. 11, pp. pp. 153–178). Springer Science+Business Media B.V.

Saatcioglu, M., Ghobarah, A., & Nistor, I. (2005). Effects of the December 26, 2004 Sumatra Earthquake and Tsunami on Physical Infrastructure. *ISET Journal of Earthquake Technology*, *42*, 79–94.

Segur, H. (2007). Waves in Shallow Water, with Empasis on the Tsunami of 2004. In A. Kundu (Ed.), *Tsunami and Non-Linear Waves* (pp. pp. 3–29). Berlin: Springer.

Sengupta, A., Haan, F. L., Sarkar, P. P., & Balaramudu, V. (2008). Transient loads on buildings in microburst and tornado winds. *Journal Of Wind Engineering And Industrial Aerodynamics*, *96*(10-11), 2173–2187.

Shi, F., Kirby, J., Harris, J., Geiman, J., & Grilli, S. T. (2012). A high-order adaptive time-stepping TVD solver for Boussinesq modeling of breaking waves and coastal inundation. *Ocean Model*, *43*, 36–51.

Sitanggang, K. I., & Lynett, P. (2005). Parallel computation of a highly nonlinear Boussinesq equation model through domain decomposition. *Int. J. Numer. Meth. Fluids*, *49*, 57–74.

Stansby, P. K., Chegini, A., & Barnes, T. C. D. (1998). The initial stages of dam-break flow. *Journal of Fluid Mechanics*, *374*, 407–424.

St-Germain, P., Nistor, I., Townsend, R., & Shibayama, T. (2014). Smoothed-Particle Hydrodynamics Numerical Modeling of Structures Impacted by Tsunami Bores. *Journal of Waterway, Port, Coastal, and Ocean Engineering*, *140*(1), 66–81.

Stoker, J. J. (1957). *Water Waves: The Mathematical Theory with Applications*. New York: Wiley-Interscience.

Suppasri, A., Shuto, N., Imamura, F., Koshimura, S., Mas, E., & Yalciner, A. C. (2013). Lessons Learned from the 2011 Great East Japan Tsunami: Performance of Tsunami Countermeasures, Coastal Buildings, and Tsunami Evacuation in Japan. *Pure and Applied Geophysics*, *170*(6), 993–1018.

Suppasri, A., Shuto, N., Imamura, F., Shunichi, K., Mas, E., & Yalciner, A. C. (2012). Lessons Learned from the 2011 Great East Japan Tsunami: Performance of Tsunami Countermeasures, Coastal Buildings, and Tsunami Evacuation in Japan. *Pure and Applied Geophysics*, 1–26.

Talaslidis, D. G., Manolis, G. D., Paraskevopoulos, E., Panagiotopoulos, C., Pelekasis, N., & Tsamopoulos, J. A. (2004). Risk analysis of industrial structures under extreme transient loads. *Soil Dynamics and Earthquake Engineering*, *24*(6), 435–

448.

Thampi, H., Dayal, V., & Sarkar, P. P. (2011). Finite element analysis of interaction of tornados with a low-rise timber building. *Journal of Wind Engineering and Industrial Aerodynamics*, *99*(4), 369–377.

Thilakarathna, H. M. I., Thambiratnam, D. P., Dhanasekar, M., Hanasekar, M., & Perera, N. (2010). Numerical simulation of axially loaded concrete columns under transverse impact and vulnerability assessment. *International Journal of Impact Engineering*, *37*, 1100–1112.

Thusyanthan, N. I., & Madabhushi, S. P. G. (2008). Tsunami wave loading on coastal houses: a model approach. *Proceedings of the ICE - Civil Engineering*, *161*(2), 77–86.

Titov, V. V., & Gonzalez, F. I. (1997). *Implementation and testing of the Method Of Splitting Tsunami (MOST) model*. NOAA Technical Memorandum ERL PMEL-112 1927. NOAA, Seattle, WA, USA.

USACE. (1990). *Wave forces on a wall shoreward of the still water level*. US Army Corps of Engineers. Coastal Engineering Research Centre, Vicksburg, MS, USA, Technical Note III-29.

Vacondio, R., Rogers, B. D., Stansby, P. K., & Mignosa, P. (2015). Variable resolution for SPH in three dimensions: Towards optimal splitting and coalescing for dynamic adaptivity. *Computer Methods in Applied Mechanics and Engineering*. http://doi.org/DOI: 10.1016/j.cma.2015.11.021.

Verlet, L. (1967). Computer experiments on classical fluids. I. Thermodynamical properties of Lennard-Jones molecules. *Physical Review*, *159*, 98–103.

Wang, X. (2009). *User manual for COMCOT version 1.7*. Ithaca, NY: Cornell University.

Wei, Z., Dalrymple, R. A., Hérault, A., Bilotta, G., Rustico, E., & Yeh, H. (2015). SPH modeling of dynamic impact of tsunami bore on bridge piers. *Coastal Engineering*, *104*, 26–42.

Yeh, H., Barbosa, A. R., Ko, H., & Cawley, J. (2014). Tsunami Loadings on Structures.

Coastal Engineering, 1–13.

Yeh, H., Liu, P. L.-F., Briggs, M., & Synolakis, C. E. (1994). Propagation and Amplification of Tsunamis at Coastal Boundaries. *Nature*, *372*, 353–355.

Yeh, H., Robertson, I., & Preuss, J. (2005). Development of Design Guidelines for Structures that Serve as Tsunami Vertical Evacuation Sites, 42.

Yim, S. C. (2005). Modeling and Simulation of Tsunami and Storm Surge Hydrodynamic Loads on Coastal Bridge Structures. *Proceeding of the 21st US-Japan Bridge Engineering Workshop*. Tsukuba-Japan.

Yu, J.-L., & Jones, N. (1997). Numerical simulation of impact loaded steel beams and the failure criteria. *International Journal of Solids and Structures*, *34*, 3977–4004.

Zabusky, N. J., & Kruskal, M. D. (1965). Interactions of Solitons in A Collisionless Plasma and The Recurrence of Initial States. *Physics Review Letter*, *15*, 240–243.

Zeinoddini, M., Parke, G. A. R., & Harding, J. E. (2008). Interface Forces in Laterally Impacted Steel Tubes. Experimental Mechanics. *Experimental Mechanics*, *48*, 265–280.